Stockholm
University

New solid-state NMR methods for exciting and separating anisotropic interactions of spin I=1 nuclei

Rihards Aleksis

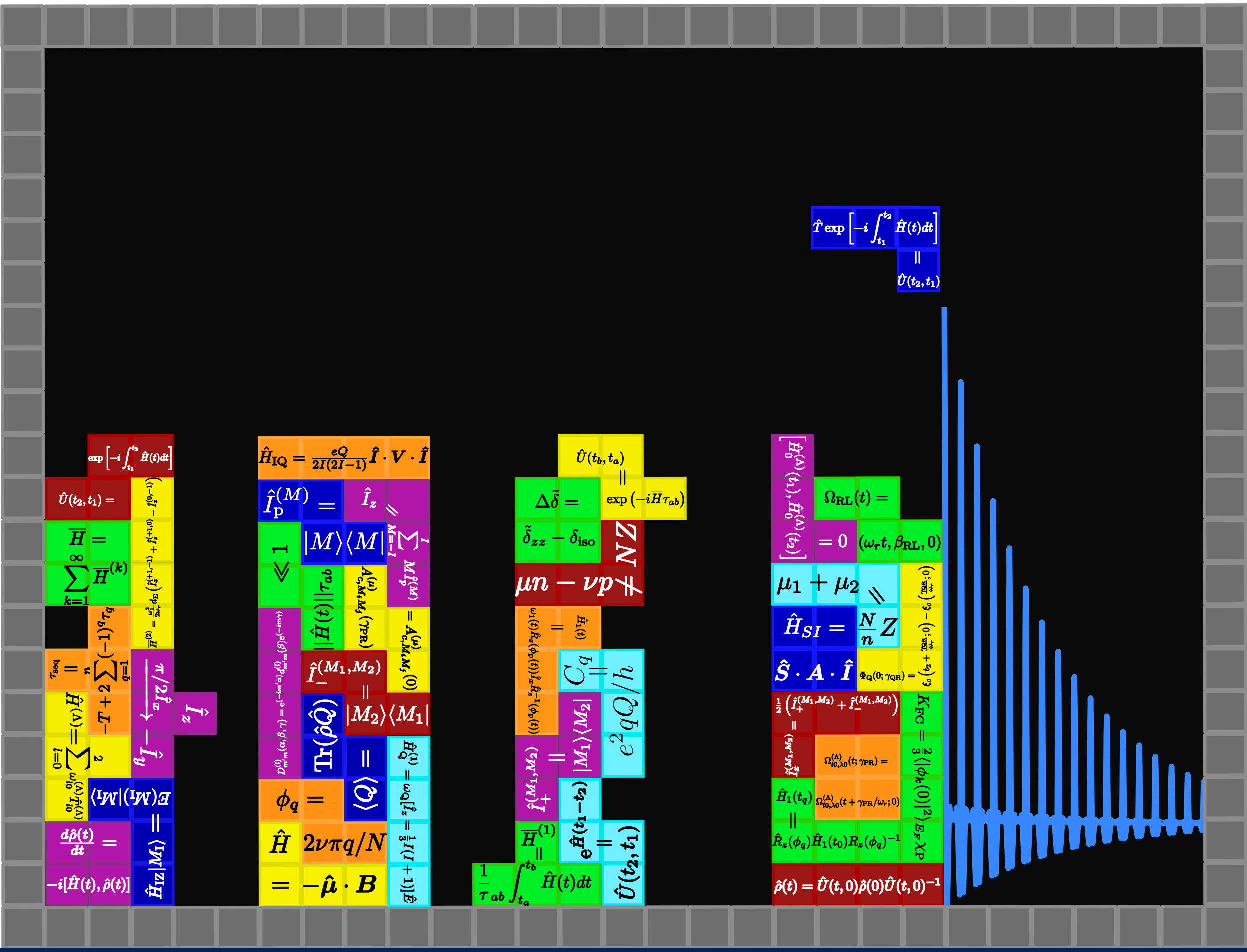
$\hat{T}\exp\left[-i\int_{t_1}^{t_2}\hat{H}(t)dt\right] = \hat{U}(t_2,t_1)$
$\hat{H}_{IQ} = \frac{eQ}{2I(2I-1)}\hat{I}\cdot V\cdot\hat{I}$
$\hat{U}(t_b,t_a) = \exp(-i\bar{H}\tau_{ab})$
$\Delta\tilde{\delta} = \tilde{\delta}_{zz} - \delta_{iso}$
$\mu n - \nu p \neq NZ$
$\Omega_{RL}(t) =$
$\mu_1 + \mu_2$
$\hat{H}_{SI} = \hat{S}\cdot A\cdot\hat{I}$
$\frac{N}{n}Z$
$\bar{H} = \sum_{k=1}^{\infty}\bar{H}^{(k)}$
$|M\rangle\langle M|$
$\mathrm{Tr}(\hat{\rho}\hat{Q}) = \langle Q\rangle$
$\phi_q =$
$\hat{H} = -\hat{\mu}\cdot B$
$2\nu\pi q/N$
$C_q = e^2qQ/h$
$\frac{d\hat{\rho}(t)}{dt} = -i[\hat{H}(t),\hat{\rho}(t)]$
$\frac{1}{\tau_{ab}}\int_{t_a}^{t_b}\hat{H}(t)dt$
$\hat{U}(t_2,t_1)$
$\hat{\rho}(t) = \hat{U}(t,0)\hat{\rho}(0)\hat{U}(t,0)^{-1}$
$\hat{R}_z(\phi_q)\hat{H}_1(t_0)\hat{R}_z(\phi_q)^{-1}$

Doctoral Thesis in Physical Chemistry at Stockholm University, Sweden 2022

New solid-state NMR methods for exciting and separating anisotropic interactions of spin I=1 nuclei

Rihards Aleksis

Academic dissertation for the Degree of Doctor of Philosophy in Physical Chemistry at Stockholm University to be publicly defended on Tuesday 19 April 2022 at 15.00 online via Zoom, public link is available at the department website.

Abstract

Solid-state NMR has become an essential tool for structural characterisation of materials, in particular systems with poor crystallinity and structural disorder. In recent years, a surge of interest has been observed for the study of paramagnetic systems, in which the interaction between nuclei and unpaired electrons allows to probe the electronic structure and properties of materials more directly. However, simultaneously this interaction leads to very broad resonances, which are difficult to acquire and interpret. While significant advancements in both NMR instrumentation and methodology have paved the way for the study of spin I=1/2 nuclei in these systems, still many issues remain to be resolved for routine investigation of quadrupolar nuclei I>1/2. In this Thesis we focus on improving both the excitation of the broad resonances and the resolution in the spectra of spin I=1 nuclei. The latter problem is addressed by developing methods for separation of the shift and the quadrupolar interactions. We introduce two new methods under static conditions, which have the advantage over previous experiments of both suppressing spectral artefacts and exhibiting a broader excitation bandwidth. Furthermore, we demonstrate for the first time an approach for separation of the anisotropic parts of the shift and quadrupolar interaction under magic-angle spinning. Secondly, to achieve broadband excitation we develop a new theoretical formalism for phase-modulated pulse sequences in rotating solids, which are applicable to nuclear spins with anisotropic interactions substantially larger than the spinning frequency, under conditions where the radio-frequency amplitude is smaller than or comparable to the spinning frequency. We apply the framework to the excitation of double-quantum spectra of ^{14}N and design new pulse schemes with γ-encoded properties. Finally, we employ some of the new sequences together with density functional theory calculations to resolve the electronic structure of barium titanium oxhydride.

Keywords: *solid-state NMR, quadrupolar, paramagnetic shifts, spinning solids, materials.*

Stockholm 2022
http://urn.kb.se/resolve?urn=urn:nbn:se:su:diva-202816

ISBN 978-91-7911-816-7
ISBN 978-91-7911-817-4

Department of Materials and Environmental Chemistry (MMK)

Stockholm University, 106 91 Stockholm

Stockholm University

NEW SOLID-STATE NMR METHODS FOR EXCITING AND SEPARATING ANISOTROPIC INTERACTIONS OF SPIN I=1 NUCLEI

Rihards Aleksis

Stockholm
University

New solid-state NMR methods for exciting and separating anisotropic interactions of spin I=1 nuclei

Rihards Aleksis

©Rihards Aleksis, Stockholm University 2022

ISBN print 978-91-7911-816-7
ISBN PDF 978-91-7911-817-4

Printed in Sweden by Universitetsservice US-AB, Stockholm 2022

Doctoral Thesis 2022

Department of Materials and Environmental Chemistry
Stockholm University
SE-106 91 Stockholm, Sweden

Faculty opponent

Prof. Robert Schurko

Department of Chemistry and Biochemistry
Florida State University, Tallahassee, USA

Evaluation committee

Prof. Marina Carravetta
School of Chemistry
University of Southampton, Southampton, UK

Prof. Elizaveta Suturina
Department of Chemistry
University of Bath, Bath, UK

Prof. Michael Odelius
Department of Physics
Stockholm University, Stockholm, Sweden

Substitute

Prof. Lena Mäler
Department of Biochemistry and Biophysics
Stockholm University, Stockholm, Sweden

List of Publications

This dissertation is based on the following papers, referred to in the text by their Roman numerals.

I **Artefact-free broadband 2D NMR for separation of quadrupolar and paramagnetic shift interactions**
Rihards Aleksis, José P. Carvalho, Aleksander Jaworski and Andrew J. Pell. *Solid State Nucl. Magn. Reson.*, **101**, 51-62 (2019).

Scientific contributions: Experimental static and MAS NMR data acquisition and analysis; performing spin dynamic simulations; leading role in writing the manuscript.

II **Separation of quadrupolar and paramagnetic shift interactions in high-resolution nuclear magnetic resonance of spinning solids**
Rihards Aleksis and Andrew J. Pell. *J. Chem. Phys.*, **155**, 094202 (2021).

Scientific contributions: Experimental static and MAS NMR data acquisition and analysis; performing spin dynamic simulations; leading role in writing the manuscript.

III **Low-power synchronous helical pulse sequences for large anisotropic interactions in MAS NMR: Double-quantum excitation of ^{14}N**
Rihards Aleksis and Andrew J. Pell. *J. Chem. Phys.*, **153**, 244202 (2020).

Scientific contributions: Experimental MAS NMR data acquisition and analysis; performing spin dynamic simulations; leading role in writing the manuscript.

IV **Probing the electronic structure and hydride occupancy in barium titanium oxyhydride through DFT-assisted solid-state NMR**
Rihards Aleksis, Reji Nedumkandathil, Wassilios Papawassiliou, Aleksander Jaworski, Ulrich Häussermann and Andrew J. Pell. *Manuscript.*

Scientific contributions: Experimental static and MAS NMR data acquisition and analysis; perfoming DFT calculations; leading role in writing the manuscript.

Publications not included in the Thesis.

A **Electrochemical denitrification and oxidative dehydrogenation of ethylbenzene over N-doped mesoporous carbon: Atomic level understanding of catalytic activity ^{15}N NMR spectroscopy**
Ireneusz Szewczyk, Anna Rokicińska, Marek Michalik, Jiahong Chen, Aleksander Jaworski, Rihards Aleksis, Andrew J. Pell, Niklas Hedin, Adam Slabon and Piotr Kuśtrowski.
Chem. Mater., **17**, 7263-7273 (2020).

Scientific contributions: Acquisition and analysis of ^{1}H and ^{15}N MAS spectra as well as the ^{1}H-^{13}C correlation spectrum.

Reprints were made with permission from the publishers.

Contents

Abbreviations **xiii**

List of Figures **xv**

List of Tables **xix**

1 Introduction **1**

2 Introduction to nuclear magnetic resonance **3**
- 2.1 Origin of nuclear magnetism . . . 3
- 2.2 Basic theory of nuclear magnetic resonance . . . 4
  - 2.2.1 The density operator . . . 4
  - 2.2.2 Basis operators . . . 5
  - 2.2.3 The spin Hamiltonian . . . 6
  - 2.2.4 Reference frame transformations . . . 8
  - 2.2.5 Propagators . . . 10
  - 2.2.6 Average Hamiltonian theory . . . 12
  - 2.2.7 Interaction-frame Hamiltonian . . . 13
- 2.3 Interactions in solid-state NMR . . . 14
  - 2.3.1 Interaction with Radio-frequency pulses . . . 14
  - 2.3.2 The chemical shielding interaction . . . 15
  - 2.3.3 The quadrupolar interaction . . . 17
  - 2.3.4 The hyperfine interaction . . . 19
- 2.4 Interpretation of NMR parameters . . . 21
  - 2.4.1 Basics of density functional theory . . . 22
  - 2.4.2 DFT in periodic solids . . . 24

3 Separation of the shift and quadrupolar interactions in static powders **27**
- 3.1 Shifting *p*- and *d*-echo sequences . . . 30
- 3.2 Adiabatic shifting *d*-echo sequences . . . 34

4 Separation of the shift and quadrupolar interactions in spinning powders 37
4.1 Theoretical description of the PASS sequence 39
4.2 Experimental performance of the PASS sequence 41

5 Excitation of large anisotropic interactions by low-power irradiation 45
5.1 Theoretical description of low-power irradiation of spins subject to large anisotropic interactions 47
5.1.1 The jolting frame description 47
5.1.2 Selection rules 48
5.2 Application to DQ excitation in spin $I = 1$ nuclei 50
5.2.1 Theoretical description of double-quantum excitation in spin $I = 1$ nuclei 50
5.2.2 Experimental evaluation of the DQ excitation pulse sequences . . . 54

6 Determination of the electronic structure and hydride occupancy in barium titanium oxyhydride 59
6.1 Comparison of ^{1}H and ^{2}H solid-state NMR 61
6.2 Determination and analysis of the quadrupole and shift tensor parameters . 63
6.3 Temperature dependence of NMR parameters 66
6.4 Density functional theory calculations 67

7 Summary 69
7.1 Sammanfattning (Summary in Swedish) 71

Acknowledgements 73

References 75

Abbreviations

1D	One-dimension
2D	Two-dimension
AHT	Average Hamiltonian theory
BMS	Bulk magnetic susceptibility
BTOD	Deuterated barium titanium oxyhydride
BTOH	Barium titanium oxyhydride
BZ	Brillouin zone
D-DQ-HMQC	Dipolar double-quantum heteronuclear multiple-quantum correlation
DFT	Density functional theory
DQ	Double-quantum
EFG	Electric-field gradient
FC	Fermi contact
FID	Free induction decay
GGA	Generalized gradient approximation
GIPAW	Gauge invariant projector augmented wave
HMQC	Heteronuclear multiple-quantum correlation
ISTO	Irreducible spherical tensor operator
LDA	Local density approximation
MAS	Magic-angle spinning
NMR	Nuclear magnetic resonance
PAF	Principle axis frame
PASS	Phase-adjusted spinning sideband
PAW	Projector augmented wave

PBE	Perdew, Ernzerhof and Burke functional
RF	Radio-frequency
SD	Spin-dipolar
SHAP	Short high-power adiabatic pulse
SQ	Single-quantum
TRAPDOR	Transfer of populations in double resonance

List of Figures

2.1 Illustration of the spin energy levels and NMR spectrum of a two-spin system I-S, where a nuclear spin $I = 1/2$ is coupled to an electron spin $S = 1/2$. In (a) is shown the array of four energy levels 1-4, assuming that $|\omega_{0,S}| > |\omega_{0,I}| > J$, $\omega_{0,S} > 0$, $\omega_{0,I} < 0$, and $J > 0$. The two I-spin transitions are shown with a red and blue arrow, and are labelled with their frequencies $\Delta\omega_{1\to2}$ and $\Delta\omega_{3\to4}$. The nuclear spin I spectrum is shown in (b) and exhibits diferent intensities of the two components of the doublet because the larger energy separation between the pairs of I-spin energy levels in the two transitions leads, via the Boltzmann distribution, to different equilibrium spin state population differences. The rapid electronic relaxation of S "decouples" the I spin spectrum to give a singlet which is positioned at the centre of mass of the two doublet components. The singlet is thus offset from $-\omega_{0,I}$ by an offset frequency $-\omega_{0,I}\delta^{\mathrm{S}}_{\mathrm{iso}}$, where $\delta^{\mathrm{S}}_{\mathrm{iso}}$ is the "paramagnetic shift" due to the electron S. Reproduced from [18], with permission of Elsevier. 20

2.2 Directly excited ^{15}N MAS NMR spectra of the SK_N sample collected at 7 kHz MAS and 14.1 T, shown together with chemical shifts calculated for hypothetical structural motifs. Experimental chemical shifts are given in black, calculated ^{15}N shifts are in blue. All shifts are in ppm. Reproduced from Ref. [69] with permission from the Royal Society of Chemistry. 22

3.1 Simulated static NMR spectra of powders. (a) shows crystallites with different orientations with respect to the external magnetic field and the resulting spectra of four of these unique crystallite orientations. Superimposed is the overall powder pattern lineshape. The spin $I = 1$ nucleus is subject to only the shift interaction in this case. In (b) we have the spectrum of a spin $I = 1$ system subject to only the first-order quadrupolar interaction. Superimposed are the spectra of each of the two transitions shown in orange and blue. (c) shows the spectrum of a spin $I = 1$ nucleus subject to both the shift and first-order quadrupolar interactions. In the simulations shift tensor parameters are $\delta_{\mathrm{iso}} = 0$, $\Delta\delta = 500$ ppm and $\eta_{\mathrm{S}} = 0.7$ and the quadrupolar tensor parameters are $C_{\mathrm{Q}} = 100$ kHz and $\eta_{\mathrm{Q}} = 0.2$. Apdated from [88] with permission of Wiley. 28

3.2 Sequences for acquiring 1D NMR spectra. On the left pulse sequences along with symmetry pathways are shown for the single pulse with a dead time (a), spin-echo (b) and solid-echo (c) experiments. On the right side are shown the corresponding simulated spectra for a spin $I = 1$ nucleus subject to either the shift, first-order quadrupolar or both interactions. Here the filled rectangle and empty rectangle represent $\pi/2$ and π, respectively. For simulations shift tensor parameters are $\delta_{\text{iso}} = 0$, $\Delta\delta = 500$ ppm and $\eta_{\text{S}} = 0.7$ and the quadrupolar tensor parameters are $C_{\text{Q}} = 100$ kHz and $\eta_{\text{Q}} = 0.2$. 29

3.3 Schematic representation of the time domain shifting *p*- and *d*-echo experiments. (a) and (b) show the respective shifting *p*- and *d*-echo experiment time domain data before and after shearing. The green and orange arrows represent *d*- and *p*-echo ridges in the time domain. Reproduced from [97], with permission of Elsevier. 31

3.4 2D spectra and pulse sequences for separation and correlation of shift and first-order quadrupolar interactions. Shifting *p*- (a), shifting *d*- (b), double adiabatic shifting *d*- (c) and quadruple adiabatic shifting *d*- (d) echo sequences and the corresponding experimental and simulated 2D spectra of ^{2}H in $CuCl_2{\cdot}2D_2O$. Here the filled rectangle, empty rectangle and rectangle with a diagonal represent $\pi/2$, π and adiabatic pulses, respectively. Time periods t_1 and t_2 are the evolution periods in the indirect and direct dimension, respectively, and τ, τ_1, τ_2, $\Delta\tau = \tau_1 - \tau_2$ are free precession periods to facilitate correct echo formation. p_I and d_I are the symmetry pathways for the experiments. Reproduced from [97], with permission of Elsevier. 33

4.1 NMR spectra of a powder sample under MAS. (a) Schematic showing the MAS rotor oriented at the magic-angle with respect to the external magnetic field. Simulated powder spectra of a spin $I = 1$ system subject to the shift and first-order quadrupolar interaction under static conditions (b), 10 kHz MAS (c) and 100 kHz MAS (d). Reproduced from Ref. [102] with permission from the Royal Society of Chemistry. 38

4.2 PASS pulse sequence. On the left we have the PASS pulse sequence with the symmetry pathways. On the right simulated PASS spectra are shown for a spin $I = 1$ nucleus subject to either the first-order quadrupolar interaction or the shift anisotropy. Reproduced from [109], with permission of AIP Publishing. 40

4.3 Experimental and simulated ^{2}H PASS spectra of $CuCl_2 \cdot 2D_2O$. From left to right are given experimental, best fit, and best fit residual ^{2}H PASS spectra of $CuCl_2 \cdot 2D_2O$. Both experimental and simulated spectra have been sheared. The projection of the isotropic shift/quadrupole dimension shows the spinning-sideband manifold, while the projection of the shift anisotropy dimension shows the profile of the spinning sideband intensities. Spectra were acquired/simulated at 4 kHz MAS. Reproduced from [109], with permission of AIP Publishing. 42

5.1 γ-encoding properties of different XN_n^ν pulse sequences. (a) shows a schematic representation of the sideband pairs contributing to the second-order average Hamiltonian for $X2_2^1$, $X62_6^{31}$ and $X94_6^{47}$ sequence. The filled and empty squares represent non-zero and zero terms, respectively. The DQ excitation efficiency as a function of irradiation time and γ_{QR} is given in (b) for a single ^{14}N spin subject to only the first-order quadrupole interaction. Details of simulations can be found in Paper III. Reproduced from [137], with permission of AIP Publishing. 52

5.2 Dipolar double-quantum heteronuclear multiple-quantum correlation (D-DQ-HMQC) pulse sequences. D-DQ-HMQC with DQ excitation/reconversion blocks using a single pulse (a) and XN_n^ν scheme (b) are provided along with the ^{1}H and ^{14}N coherence pathways. The filled and empty rectangle represent $\pi/2$ and π pulses, respectively. RN_n^ν are the symmetry-based heteronuclear dipolar recoupling sequences. Reproduced from [137], with permission of AIP Publishing. 54

5.3 Experimental and simulated contour plots for generation of ^{14}N DQ coherence from microcrystalline powder of glycine. From left to right are shown simulated and experimental DQ coherence generation efficiency plots as a function of irradiation time and RF field amplitude using a single pulse (a), $X2_2^1$ (b) and $X62_6^{31}$ (c) for DQ excitation and reconversion. The simulated DQ generation efficiency was obtain from a DQ-filtered experiment by varying the irradiation time and RF field amplitude symmetrically of both the excitation and reconversion blocks. The simulations included the first- and second-order quadrupolar interactions. See Paper III more simulation and experimental details. Reproduced from [137], with permission of AIP Publishing. 55

5.4 Experimental and simulated second-order quadrupolar lineshape from microcrystalline powder of glycine. (a) shows the experimental projections of the indirect dimension of 2D-D-DQ-HMQC spectra using a single pulse, $X2_2^1$ or $X62_6^{31}$ for DQ generation. Full 2D D-DQ-HMQC spectra are available in Paper III. Simulated projections of the indirect dimension of 2D DQ-SQ spectra using single pulse, $X2_2^1$ or $X62_6^{31}$ for DQ generation are provided in (b) in black, while the ideal second-order quadrupole lineshapes are given in red. The simulated DQ-SQ experiments were performed with the same irradiation times and RF powers as the experimental 2D D-DQ-HMQC. The DQ excitation efficiency for each crystal orientation (α, β) is shown in (c) using a spherical coordinate system $(1.0, \alpha, \beta)$. The intensity for each crystallite was acquired from a DQ-filtered experiment, averaging over 48 γ angles was used. Reproduced from [137], with permission of AIP Publishing. 57

5.5 2D D-DQ-HMQC spectra with large spectral window in the indirect dimension of glycine obtained with $X2_2^1$ (a) and $X62_6^{31}$ (b). Reproduced from [137], with permission of AIP Publishing. 58

6.1 Possible electronic structures of barium titanium oxyhydride considered in this work. From left to right the DFT optimized $2 \times 2 \times 2$ supercells for a polaron (a), a bandstate (b) and a double occupied bandstate (c) scenarios are shown. Below the structures the corresponding DFT calculated electronic bandstructures are shown. The blue and red colours represent occupied and unoccupied levels, respectively. The unpaired spin density is given by the isosurface in yellow. 60
6.2 MAS NMR spectra of barium titanium oxyhydrides. (a) shows the ^{1}H spectrum at 60 kHz MAS of unlabeled barium titanium oxyhdyride. In (b) from top to bottom are given ^{2}H spectra at 30 kHz MAS of $BTOD_{NAB}$, $BTOD_{CA}$ and $BTOD_{EXCH}$, with their determined hydride contents y. 62
6.3 Experimental ^{2}H spectra of $BTOD_{CA}$ under static and MAS conditions. The static 1D and 4 kHz MAS spectra are shown in (a) and (b), respectively. The static 2D adiabatic shifting *d*-echo experiment and 2D PASS at 4kHz MAS are given in (c) and (d), respectively. 63
6.4 2D static shifting *d*-echo NMR spectra of different BTOD samples. From left to right are given experimental, best fit and best fit residual spectra of $BTOD_{NAB}$ (a) and $BTOD_{CA}$ (b) and $BTOD_{EXCH}$ (c). 65
6.5 Temperature dependence of NMR parameters. The plot displays the quantity T_1TK^2 of ^{2}H in $BTOD_{CA}$ as a function of temperature. 67
6.6 Deviation from linearity of the total electronic energy as a function of the charge of the system. The plots with suboptimal and optimal U values are given in red and green, respectively. The calculations were performed on a $2 \times 2 \times 2$ supercell with $BaTiO_{2.875}H_{0.125}$ composition in the polaronic state. 68

List of Tables

4.1 Best fit tensor parameters obtained from the 2D quadruple shifting *d*-echo (static) and PASS (MAS) spectra of $CuCl_2 \cdot D_2O$. 41

6.1 Isotropic shift of ^2H and ^2H concentration in $BaTiO_{3-x}D_y$ 61
6.2 Best fit shift and quadrupolar tensor parameters and errors for the 2D adiabatic shifting *d*-echo spectra of $BTOD_{NAB}$, $BTOD_{CA}$ and $BTOD_{EXCH}$. . . . 66
6.3 DFT computed and $BTOD_{CA}$ quadrupolar tensor parameters 68

1

Introduction

At the heart of modern science lies our ability to obtain atomic and molecular level insights on almost any system. Detailed information on such a small scale has allowed the improvement of functional materials, [1; 2] discovery of new phenomena in physics, [3; 4] furthered our understanding of living organisms [5; 6] and facilitated novel drug development [7–9]. Frequently, the knowledge of the structure at an atomic level proves to be the key ingredient for these advancements.

Diffraction methods, such as X-ray crystallography, remain the principal tools for structural characterization of crystalline materials. However, conventional diffraction techniques fail when materials lack long-range order. In contrast, solid-state nuclear magnetic resonance (NMR) is well equipped to study crystalline and noncrystalline materials (e.g., polymers, [10] protein fibrils, [11; 12] glasses [13; 14]), as well as surface structures, [15; 16] defects and local distortions [17] in solids. Due to the versatility of NMR and the wide range of interactions available it is unsurprising that NMR offers to examine materials even beyond the structure and local geometry. The foremost example would be the study of paramagnetic systems, which has seen considerable interest in recent years as a result of advancements in NMR methodology and quantum chemical calculations. [18]

The advantage (and disadvantage) of paramagnetic systems manifests from the hyperfine interaction between the nuclear spin and the unpaired electrons. The interaction can give crucial insights on the bonding geometry, delocalization/polarization of the spin density, ion dynamics and particle shape. [19–22] Therefore, solid-state NMR is becoming an attractive method to investigate exotic electronic states, such as, polarons and topological insulators. [23; 24] However, the observed resonances in paramagnetic systems are severely broadened due to the large paramagnetic shift anisotropies and bulk magnetic susceptibility (BMS) effects, which impede the acquisition and interpretation of the data. In addition, the excited coherence lifetimes are reduced by the paramagnetic relaxation enhancement, hence lowering the experimental sensitivity. For spin $I = 1/2$ nuclei most of these issues have been solved. For instance, fast magic-angle spinning (MAS) in combination with low recycle delays provides considerable improvement in both resolution and sensitivity. [25] Frequency stepping and the development of new broadband excitation schemes have allowed acquisition of the broad spectra. [26–28] However, for quadrupolar nuclei, i.e. nuclei with spin $I > 1/2$, the presence of the quadrupolar interaction provides an additional broadening of the resonance. The convolution of the two interactions make the analysis of both the hyperfine and the quadrupolar interaction extremely difficult. Furthermore, most of the broadband schemes applicable for spin $I = 1/2$ nuclei fail for quadrupolar nuclei under MAS due to the complicated time-dependency of the spin dynamics.

In the present work, we address some these issues for spin $I = 1$ nuclei. We begin by examining how the NMR spectra could be deconvolved by employing methods for separation of the shift and the quadrupolar interactions. First, we explore NMR methods that can achieve this result under static conditions and devise two new pulse sequences. Secondly, we investigate similar sequences under MAS and demonstrate the separation of the anisotropic parts of the two interactions in spinning solids. Afterwards, we focus on the excitation of very large anisotropic interactions under MAS and provide a new theoretical formalism for developing such pulse schemes. We apply the new theoretical approach to study the double-quantum excitation of spin $I = 1$ nuclei. Finally, we showcase the potential of a few of the sequences by resolving the electronic structure of an important mixed electron-ion conductor.

The Thesis is structured as follows: in Chapter 2 we overview the basic quantum mechanics concepts necessary to describe solid-state NMR experiments considered in this work. In addition, we revise the principles of density functional theory (DFT) calculations, which can aid in the interpretation of NMR data. In Chapter 3, which is based on Paper I, we discuss NMR methods for separation of the shift and quadrupolar interactions in static solids. In Chapter 4 we summarise the results of Paper II, in which an experiment for separation of the shift and quadrupolar interactions under MAS is proposed. In Chapter 5 we explore low-power excitation of large anisotropic interactions under MAS as presented in Paper III. Chapter 6 forms the basis of Paper IV, where we combine NMR and DFT to demonstrate how we can solve problems in materials science by employing the new solid-state NMR methods.

2

Introduction to nuclear magnetic resonance

2.1 Origin of nuclear magnetism

In classical electromagnetism the energy E arising from the interaction between a magnetic moment $\boldsymbol{\mu}$ and a magnetic field $\mathbf{B}$ is given by the scalar product:

$$E = -\boldsymbol{\mu} \cdot \mathbf{B}. \tag{2.1}$$

In quantum mechanics this energy is expressed by the eigenvalues of the corresponding Hamiltonian $\hat{H}$, which is shown below:

$$\hat{H} = -\hat{\boldsymbol{\mu}} \cdot \mathbf{B}, \tag{2.2}$$

where $\hat{\boldsymbol{\mu}}$ is the magnetic moment operator. Atomic nuclei possess an intrinsic property called spin, I. If the nuclear spin is non-zero $I \neq 0$, the nucleus exhibits a magnetic dipole moment. The operator that measures the nuclear magnetic moment is described by:

$$\hat{\boldsymbol{\mu}}_I = \gamma_I \hat{\mathbf{I}}, \tag{2.3}$$

where $\hat{\mathbf{I}}$ is the nuclear spin angular moment operator. γ_I is the gyromagnetic ratio of the specific nucleus. The gyromagnetic ratio can take both positive and negative values depending on the nuclear configuration of protons and neutrons. We note that the operator is defined in terms of "frequency" units. We will adopt this notation for Hamiltonians and propagators throughout the Thesis and Papers I-III to facilitate theoretical description of spin dynamics.

Typically in nuclear magnetic resonance (NMR) spectrometers a homogeneous magnetic field is applied along a single direction, which by convention is denoted as the z axis in the laboratory frame. The interaction of the nuclear magnetic moment with an external magnetic field B_0 gives the nuclear Zeeman interaction Hamiltonian $\hat{H}_{\mathrm{IZ}}$:

$$\hat{H}_{\mathrm{IZ}} = -\gamma_I B_0 \hat{I}_z = \omega_0 \hat{I}_z, \tag{2.4}$$

where $\hat{I}_a$ is the operator representing the component of the spin along axis a. $\omega_0 = -\gamma_I B_0$ is the Larmor frequency. Hence nuclei with positive gyromagnetic ratios, such as ^{1}H and ^{13}C give negative Larmor frequencies, whereas nuclei with negative gyromagnetic ratios (^{15}N) have a positive Larmor frequency. The nuclear spin angular momentum as any quantity in quantum mechanics, takes only discrete values. A nucleus of spin quantum number I has $2I+1$ states labelled as $|I, M_I\rangle$, where M_I is the magnetic quantum number taking values of $-I$ to $+I$ in integer steps. The definition of the states can be written more compactly as $|M_I\rangle$, which are eigenfunctions of $\hat{I}_z$ with eigenvalues M_I, and will be used throughout the Thesis as well as in Papers I-III. Thus, these states are also eigenstates of the Zeeman Hamiltonian with energy $E(M_I)$:

$$\hat{H}_{\mathrm{IZ}}|I, M_I\rangle = E(M_I)|I, M_I\rangle = M_I \omega_0 |I, M_I\rangle \tag{2.5}$$

However, in the absence of an magnetic field the states are $2I+1$-fold degenerate. In NMR we measure the frequency associated with nuclear spin transitions so in order to lift the degeneracy we apply an external magnetic field. From Eq.2.5 we see that the energy between two adjacent energy levels is related to the Larmor frequency ω_0.

2.2 Basic theory of nuclear magnetic resonance

2.2.1 The density operator

Conventional NMR experiments are performed on a large number of interacting spins. However, the description is simplified by approximating the system as a collection of N_{ens} independent, identical smaller spin systems called an ensemble. A state k of the ensemble can be expressed as a linear combination of eigenfunctions of the Zeeman Hamiltonian $|r\rangle$ as:

$$|\psi_k\rangle = \sum_{r=1}^{N} c_r^k |r\rangle, \tag{2.6}$$

where c_r^k are normalized coefficients ($\sum_r |c_r^k|^2 = 1$) giving the amplitude for a contribution from $|r\rangle$ to the spin system $|\psi_k\rangle$. In principle, to compute a macroscopic quantity, such as the nuclear magnetization, it is possible to evaluate the expectation value of each member of the ensemble and sum the results. However, this process proves to be tedious due to the large number of components of the ensemble. An alternative approach is to employ the density operator $\hat{\rho}$, which describes the quantum state of the entire ensemble and is given by:

$$\hat{\rho} = \overline{|\psi_k\rangle\langle\psi_k|}. \tag{2.7}$$

The overbar denotes an average over the entire ensemble. Using the density operator approach the macroscopic observable quantity ($\hat{Q}_{\text{macro}}$) of operator $\hat{Q}$ is expressed as:

$$Q_{\text{macro}} = N_{\text{ens}}\text{Tr}(\hat{\rho}\hat{Q}), \tag{2.8}$$

where $\text{Tr}(\hat{A})$ denotes the trace of an operator $\hat{A}$, i.e. the sum of the diagonal elements. So we can write the average contribution of each ensemble member to the macroscopic value as:

$$\langle Q \rangle = \text{Tr}(\hat{\rho}\hat{Q}). \tag{2.9}$$

In NMR the relevant macroscopic quantity is the magnetization, however it proves to be convenient to use the spin angular momentum as the microscopic quantity, which requires additional constants of proportionality in Eq.2.9.

The response of the spin system to any pulse sequence can be described using the density operator formalism. To follow the evolution of the spin system we need to know the starting condition of the system and a law predicting the evolution. Usually at the beginning of the sequence the density operator $\hat{\rho}_0$ is at thermal equilibrium. In the presence of a strong magnetic field in the high-temperature limit ($\frac{\hbar\gamma_I B_0}{k_B T} \ll 1$) the equilibrium density operator can be derived from the Boltzmann distribution [29]:

$$\hat{\rho}_0 = \frac{\hat{E} + \beta\hbar\gamma_I B_0 \hat{I}_z}{2I+1}, \tag{2.10}$$

where β is related to the Boltzmann constant k_B and temperature as $\beta = 1/k_B T$. $\hbar$ is the reduced Plancks constant. The first term $\hat{E}$ is the identity operator, which commutes with all other spin operators and does not produce any observable signal, hence is ignored. In the present discussion we are not interested in the absolute size of the signal, and so the prefactor $\frac{\beta\hbar\gamma_I B_0}{2I+1}$ of the second term is omitted to facilitate the analysis of the pulse sequences, hence the equilibrium density operator is $\hat{\rho}_0 = \hat{I}_z$.

2.2.2 Basis operators

As discussed earlier the nuclear spin wavefunction of a single spin I can be expressed as a linear combination of $2I+1$ basis functions. It is convenient to choose the basis functions as the eigenfunctions of the Zeeman Hamiltonian $|I, M_I\rangle$. Furthermore, we can facilitate the description of the spin dynamics by expressing the density operator as a superposition of $(2I+1)^2$ basis operators $\{\hat{B}_i\}$, which are chosen to be orthogonal:

$$(\hat{B}_i|\hat{B}_j) = \text{Tr}(\hat{B}_i^\dagger \hat{B}_j) = N\delta_{ij}, \tag{2.11}$$

where N is a normalization factor and δ_{ij} corresponds to the Kronecker delta.

Here we review the different operator bases, which we will find useful for expressing both the interaction Hamiltonians and the density operator throughout the Thesis and Papers I-III. The single-element operator basis comprises operators $|M_1\rangle\langle M_2|$. $|M_1\rangle$ are Zeeman eigenfunctions as discussed earlier. Each operator in the Zeeman function basis represents a single-element of the density matrix, thus have been named single-element operators. Each operator is associated with an order p, where $p = M_1 - M_2$. As a result the operators can be separated into three groups with $p = 0$, $p > 0$ and $p < 0$, as shown below:

$$\hat{I}_{\mathrm{p}}^{(M)} = |M\rangle\langle M|, \tag{2.12}$$

$$\hat{I}_{+}^{(M_1,M_2)} = |M_1\rangle\langle M_2|, \tag{2.13}$$

$$\hat{I}_{-}^{(M_1,M_2)} = |M_2\rangle\langle M_1|. \tag{2.14}$$

The operators $I_{\pm}^{(M_1,M_2)}$ indicate coherences between states $|M_1\rangle$ and $|M_2\rangle$ with $M_1 > M_2$, and $I_{\mathrm{p}}^{(M)}$ represents the population of the state M.

The single-element operators are associated with the frequently used Cartesian basis operators $(\hat{E}, \hat{I}_z, \hat{I}_x, \hat{I}_y)$ by the following equations:

$$\hat{E} = \sum_{M=-I}^{+I} \hat{I}_p^{(M)}, \tag{2.15}$$

$$\hat{I}_z = \sum_{M=-I}^{+I} M\hat{I}_p^{(M)}, \tag{2.16}$$

$$\hat{I}_x = \sum_{M=-I}^{+I} \frac{1}{2}\sqrt{I(I+1) - M(M+1)}\left(\hat{I}_{+}^{(M+1,M)} + \hat{I}_{-}^{(M+1,M)}\right), \tag{2.17}$$

$$\hat{I}_y = \sum_{M=-I}^{+I} \frac{1}{2i}\sqrt{I(I+1) - M(M+1)}\left(\hat{I}_{+}^{(M+1,M)} - \hat{I}_{-}^{(M+1,M)}\right). \tag{2.18}$$

Another convenient basis that will be used throughout this work is the set of fictitious spin-$1/2$ operators [30] given by:

$$\hat{I}_x^{(M_1,M_2)} = \frac{1}{2}\left(\hat{I}_{+}^{(M_1,M_2)} + \hat{I}_{-}^{(M_1,M_2)}\right), \tag{2.19}$$

$$\hat{I}_y^{(M_1,M_2)} = \frac{1}{2i}\left(\hat{I}_{+}^{(M_1,M_2)} - \hat{I}_{-}^{(M_1,M_2)}\right), \tag{2.20}$$

$$\hat{I}_z^{(M_1,M_2)} = \frac{1}{2}\left(\hat{I}_p^{(M_1)} - \hat{I}_p^{(M_2)}\right). \tag{2.21}$$

Each operator corresponds to the x-, y- and z-components of the spin within the respective operator subspace (M_1, M_2).

Finally, we define the basis of the irreducible spherical tensor operators (ISTO) $\hat{T}_{lm}$ of rank l and order m. The complete basis of a single spin I consist of operators with ranks $l = 0$ to $2I$, and orders $m = -l$ to l in integers steps. [31]

2.2.3 The spin Hamiltonian

The dynamics of any quantum system is governed by the Schrödinger equation and the appropriate Hamiltonian. Though there are various types of spin interactions, each of them can be described as a coupling between two vectors via a rank-2 Cartesian tensor, which holds all the information about the spatial properties of the interaction. Thus, for an arbitrary interaction Λ we can write the interaction Hamiltonian as follows:

$$\hat{H}^{(\Lambda)} = \hat{\mathbf{I}}_i \cdot \omega^{(\Lambda)} \cdot \hat{\mathbf{I}}_j, \tag{2.22}$$

where $\hat{\mathbf{I}}_i$ represents a spin vector or a vector field, $\hat{\mathbf{I}}_j$ is the same or different spin vector to $\hat{\mathbf{I}}_i$ and $\omega^{(\Lambda)}$ is a rank-2 Cartesian tensor in frequency units, which is given by a 3×3 matrix. This tensor represents both size and orientation dependence of the interaction. The spin interaction tensors are diagonal in a particular coordinate system, which is called the principal axis frame (PAF) and the corresponding eigenvalues are the principal values of the tensor.

Often it is more convenient to express the field, spin, and spatial parts of the interaction Hamiltonian in an irreducible spherical tensor representation. In this representation the spin Hamiltonian of an interaction Λ is expressed as a scalar product of two irreducible spherical tensors, corresponding to a spatial and a spin angular momentum part. The ISTO ($\hat{T}_{lm}$) describing the spin part have been introduced in the Section 2.2.2. We note that the Cartesian tensor $\omega^{(\Lambda)}$ contains nine real components and can be decomposed into three irreducible spherical tensors, a rank-0 tensor equal to $\frac{1}{3}\mathrm{Tr}(\omega^{(\Lambda)})$, an assymetric rank-1 tensor and a symmetric rank-2 tensor. Thus, the Hamiltonian of interaction Λ in the irreducible spherical tensor basis is given by:

$$\hat{H}^{(\Lambda)} = \sum_{l=0}^{2} \sum_{m=-l}^{+l} (-1)^m \omega_{lm}^{(\Lambda)} \hat{T}_{l-m}^{(\Lambda)}. \tag{2.23}$$

For many NMR interactions the asymmetric part of the tensor $\omega^{(\Lambda)}$ is either zero or it does not contribute to the signal in the high-field approximation. Therefore, usually only the rank-0 and the symmetric rank-2 part need to be considered.

In that case the tensor $\omega^{(\Lambda)}$ is diagonal in the PAF of the symmetric part of the tensor ($\omega^{(\Lambda)\mathrm{sym}}$). The tensor components can be ordered according to the Haeberlen convention $|\tilde{\omega}_{zz}^{(\Lambda)\mathrm{sym}}| \geq |\tilde{\omega}_{xx}^{(\Lambda)\mathrm{sym}}| \geq |\tilde{\omega}_{yy}^{(\Lambda)\mathrm{sym}}|$. [32] The rank-2 spherical tensor components are given by:

$$\tilde{\omega}_{20}^{(\Lambda)} = \sqrt{\frac{3}{2}} \Delta\omega^{(\Lambda)}, \tag{2.24}$$

$$\tilde{\omega}_{2\pm1}^{(\Lambda)} = 0, \tag{2.25}$$

$$\tilde{\omega}_{2\pm2}^{(\Lambda)} = -\frac{1}{2} \eta_\Lambda \Delta\omega^{(\Lambda)}. \tag{2.26}$$

Here tilde denotes that the tensor components are evaluated in the PAF of the symmetric part of $\omega^{(\Lambda)}$. Symmetric anisotropy and assymetry are given by:

$$\Delta\omega^{(\Lambda)} = \tilde{\omega}_{zz}^{(\Lambda)\mathrm{sym}}, \tag{2.27}$$

$$\eta_\Lambda = \frac{\tilde{\omega}_{yy}^{(\Lambda)\mathrm{sym}} - \tilde{\omega}_{xx}^{(\Lambda)\mathrm{sym}}}{\Delta\omega^{(\Lambda)}}. \tag{2.28}$$

In general, NMR experiments are carried out in the high-field limit, in which the magnitude of the Zeeman interaction is much greater than any of the other spin interactions. Therefore, the form of the Hamiltonian can be simplified by treating the spin interactions as a perturbation to the Zeeman Hamiltonian. The perturbation expansion is evaluated by transforming the interaction Hamiltonian into the rotating frame (the reference frame rotating at the transmitter frequency), followed by an average Hamiltonian expansion according to the Baker-Campbell-Haussdorff expansion. [33; 34] Typically it is sufficient to truncate the expansion to first-order, however, for the quadrupolar interaction the second-order term is often required to describe the spin dynamics correctly. As a result, in the high-field (or secular) approximation only spin operators $\hat{T}_{l0}$ with order $m = 0$ are retained and so the Hamiltonian of the interaction Λ is written as:

$$\hat{H}^{(\Lambda)} = \sum_{l=0}^{2} \omega_{l0}^{(\Lambda)} \hat{T}_{l0}^{(\Lambda)}. \tag{2.29}$$

In Section 2.3 we provide concrete interaction Hamiltonians of the relevant spin interactions.

2.2.4 Reference frame transformations

The irreducible spherical tensor can be expressed in different frames of reference. It proves to be convenient to express the spatial part in the principal axis frame (PAF) of the tensor. We note that for some NMR interactions different spatial tensors of the same rank may couple to spin tensors of different spin ranks. Thus, we define l as the space rank and λ as the spin rank. Furthermore, the order of the spatial part m and spin part μ take values of $m = -l$ to $+l$ and $\mu = -\lambda$ to $+\lambda$ in integer steps, respectively. In the high-field limit we can write the Hamiltonian of interaction Λ as:

$$\hat{H}^{(\Lambda)} = \sum_{l,\lambda} \omega_{l0,\lambda0}^{(\Lambda)} \hat{T}_{\lambda0}^{(\Lambda)}. \tag{2.30}$$

The coefficient $\omega_{l0,\lambda0}^{(\Lambda)}$ represents spatial part of the interaction Λ, which is related to the components in the PAF via a rotation between the PAF and laboratory frame:

$$\omega_{l0,\lambda0}^{(\Lambda)} = \sum_{m=-l}^{+l} \tilde{\omega}_{lm,\lambda0}^{(\Lambda)} D_{m0}^{(l)}(\alpha_{\mathrm{PL}}, \beta_{\mathrm{PL}}, \gamma_{\mathrm{PL}}), \tag{2.31}$$

where $D_{m'm}^{(l)}(\alpha, \beta, \gamma)$ are the Wigner rotation matrix elements of rank l, [35] and the Euler angles $(\alpha_{\mathrm{PL}}, \beta_{\mathrm{PL}}, \gamma_{\mathrm{PL}})$ specifying the orientation of PAF in the laboratory frame. The Wigner rotation matrix elements can be expressed in terms of the reduced matrix elements $d_{m'm}^{l}$ by dividing the contribution of each Euler angle into a separate factor:

$$D_{m'm}^{(l)}(\alpha, \beta, \gamma) = \exp(-im'\alpha) d_{m'm}^{(l)}(\beta) \exp(-im\gamma). \tag{2.32}$$

We can notice that as a consequence of the high-field approximation the interaction is independent of the Euler angle γ_{PL}.

In solid-state NMR four reference frames are commonly used the laboratory frame (L), the rotor frame (R), crystal frame (C) and the PAF (P). The relation between them can be expressed with Wigner rotation matrix elements in a similar manner as shown in Eq.2.31. In Paper I we define the interaction Hamiltonians using the PAF, crystal and laboratory frames, since under static conditions the rotor frame can be ignored.

In Paper II and III we employ magic-angle spinning (MAS) so the rotor frame becomes crucial for the description of the Hamiltonians. However, to facilitate the discussion we remove the rotation to the crystal frame, which effectively means that we combine the PAF with the crystal frame orientation. According to this notation we write the Hamiltonian for a sum of different interactions as:

$$\hat{H}_0(t) = \sum_{\Lambda} \hat{H}_0^{(\Lambda)}(t) = \sum_{\Lambda,l,\lambda} \Omega^{(\Lambda)}_{l0,\lambda0}(t;\gamma_{\mathrm{PR}})\hat{t}^{(\Lambda)}_{\lambda0}, \tag{2.33}$$

where $\hat{H}_0^{(\Lambda)}(t)$ is the individual interaction Hamiltonian. The $\hat{t}^{(\Lambda)}_{\lambda0}$ are reduced spin tensor operators [36] of rank λ related to ISTO as $\hat{t}^{(\Lambda)}_{00} = \hat{T}^{(\Lambda)}_{00}$, $\hat{t}^{(\Lambda)}_{10} = \hat{T}^{(\Lambda)}_{10}$, $\hat{t}^{(\Lambda)}_{20} = \sqrt{\frac{2}{3}}\hat{T}^{(\Lambda)}_{20}$ and $\hat{t}^{(\Lambda)}_{30} = \frac{\sqrt{10}}{3}\hat{T}^{(\Lambda)}_{30}$. We utilize the reduced spin tensor operators to avoid awkward numerical factors in further equations. $\Omega^{(\Lambda)}_{l0,\lambda0}(t;\gamma_{\mathrm{PR}})$ is the orientational- and time-dependent frequency shift of the interaction. The orientational dependence is described by a set of Euler angles $\Omega_{\mathrm{PR}} = (\alpha_{\mathrm{PR}}, \beta_{\mathrm{PR}}, \gamma_{\mathrm{PR}})$ relating the PAF to the rotor frame and a set of Euler angles $\Omega_{\mathrm{RL}}(t) = (\omega_r t, \beta_{\mathrm{RL}}, 0)$, which specify the orientation of the rotor frame with respect to the laboratory frame. Since we are interested in looking at the Hamiltonian under spinning conditions the Euler angle α_{RL} is time-dependent and proportional to the spinning frequency ω_r. The Euler angle β_{RL} is chosen so that the reduced Wigner element $d^{(2)}_{00}$ would be zero, hence any time-independent terms arising from rank-2 tensors would be removed. This "magic-angle" is given by $\arctan\left(\sqrt{2}\right)$. Thus, the spatial component is given by:

$$\Omega^{(\Lambda)}_{l0,\lambda0}(t;\gamma_{\mathrm{PR}}) = \sum_{m=-l}^{+l} \omega^{(\Lambda)}_{c,l0,\lambda0,m}(\gamma_{\mathrm{PR}})\exp(-im\omega_r t), \tag{2.34}$$

where $\omega^{(\Lambda)}_{c,l0,\lambda0,m}(\gamma_{\mathrm{PR}})$ are time-independent coefficients expressed as:

$$\omega^{(\Lambda)}_{c,l0,\lambda0,m}(\gamma_{\mathrm{PR}}) = \sum_{m'=-l}^{+l} \tilde{\omega}^{(\Lambda)}_{lm',\lambda0} D^{(l)}_{m'm}(\alpha_{\mathrm{PR}}, \beta_{\mathrm{PR}}, \gamma_{\mathrm{PR}}) d^{(l)}_{m0}(\beta_{\mathrm{RL}}). \tag{2.35}$$

Furthermore, the description of spin dynamics under MAS can be facilitated by defining a carousel denoted by c for the coefficient $\omega^{(\Lambda)}_{c,l0,\lambda0,m}(\gamma_{\mathrm{PR}})$ that comprises all crystallites, which occupy the same orientations during the sample rotation, but at different times. [37] In practice, the crystallites within a certain carousel are those with same α_{PR} and β_{PR}, but different γ_{PR}.

2.2.5 Propagators

We are now in a position to discuss the impact of a pulse sequence on a nuclear spin system, which is described by the time evolution of the density operator $\hat{\rho}(t)$. The coherent evolution of $\hat{\rho}(t)$ is dictated by the Liouville–von Neumann equation:

$$\frac{d\hat{\rho}(t)}{dt} = -i[\hat{H}(t), \hat{\rho}(t)]. \tag{2.36}$$

We note that any incoherent processes, such as relaxation are not considered. The general solution to the Liouville-von Neumann equation is produced by sandwiching the initial density operator between the forward and backward system propagator:

$$\hat{\rho}(t) = \hat{U}(t,0)\hat{\rho}(0)\hat{U}(t,0)^{-1}. \tag{2.37}$$

Here $\hat{U}(t,0)$ is the propagator, corresponding to the Hamiltonian $\hat{H}(t)$. Depending on the type of Hamiltonian $\hat{H}(t)$ the propagator can be separated into three groups. We begin with the simplest case, when the Hamiltonian $\hat{H}$ is time-independent. So the propagator $\hat{U}(t_1,t_2)$ between some arbitrary time points t_1 and t_2 is given by:

$$\hat{U}(t_2,t_1) = \exp\left[-i\hat{H}(t_2 - t_1)\right]. \tag{2.38}$$

We encounter this situation in solution and static solid-state NMR during periods of free precession. This can be extended to a pulse sequence with piecewise time-independence, hence the total propagator of the sequence would be given by the product of the individual propagators for each time-independent process. We find that the transformation of density operator $\hat{\rho}(t_1)$ to $\hat{\rho}(t_2)$ via propagator $\hat{U}(t_2,t_1)$ with a corresponding Hamiltonian $\hat{H}$ is more succinctly illustrated as follows:

$$\hat{\rho}(t_1) \xrightarrow{\hat{H}(t_2 - t_1)} \hat{\rho}(t_2) \tag{2.39}$$

We employ these strategies in Paper I to describe pulse sequences under static conditions.

Next we consider when the Hamiltonian self commutes at any arbitrary time, i.e. satisfies $\left[\hat{H}(t_1),\hat{H}(t_2)\right] = 0$ for all times t_1 and t_2. In the present case, the propagator is given by:

$$\hat{U}(t_2,t_1) = \exp\left[-i\int_{t_1}^{t_2} \hat{H}(t)dt\right]. \tag{2.40}$$

This represents the situation in solid-state MAS NMR of an isolated single spin. This form of the propagator is important in Papers II and III.

Finally, we discuss the most general case, in which the Hamiltonian is time-dependent and does not self commute for any arbitrary time, i.e. $\left[\hat{H}(t_1),\hat{H}(t_2)\right] = 0$ is not satisfied for all times t_1 and t_2. The propagator describing the evolution between t_1 and t_2 is expressed as:

$$\hat{U}(t_2,t_1) = \hat{T}\exp\left[-i\int_{t_1}^{t_2} \hat{H}(t)dt\right], \tag{2.41}$$

where $\hat{T}$ is the Dyson time-ordering operator, which arranges the sequence of propagators in correct order. Although this is the most general solution, it is not analytically useful and approximate solutions need to be considered. We review one such approach in detail in Section 2.2.6. These strategies are employed in Paper III to describe phase-modulated low-power sequences under MAS.

Here we continue by demonstrating the evolution of a single-spin under MAS subject to several interactions Λ. We consider an isolated single spin or single spin subject to dipolar interactions only under the weak coupling regime, hence the Hamiltonian in Eq.2.33 self commutes. According to the second case, the propagator describing the evolution between time points t_a and t_b is given by:

$$\begin{aligned}\hat{U}_0(t_b,t_a;\gamma_{\text{PR}}) &= \exp\left(-i\int_{t_a}^{t_b}\hat{H}_0(t)dt\right)\\ &= \prod_{\Lambda,l,\lambda}\exp\left(-i\Phi^{(\Lambda)}_{l0,\lambda 0}(t_b,t_a;\gamma_{\text{PR}})\hat{t}^{(\Lambda)}_{\lambda 0}\right),\end{aligned}\tag{2.42}$$

where $\Phi^{(\Lambda)}_{l0,\lambda 0}(t_b,t_a;\gamma_{\text{PR}})$ is the integrated phase, which is accrued during the evolution of the density operator between time points t_a and t_b and is expressed as:

$$\Phi^{(\Lambda)}_{l0,\lambda 0}(t_b,t_a;\gamma_{\text{PR}}) = \int_{t_a}^{t_b}\Omega^{(\Lambda)}_{l0,\lambda 0}(t;\gamma_{\text{PR}})dt.\tag{2.43}$$

Assuming our initial density operator consists of a single-element operator $|M_i\rangle\langle M_j|$ then the evolution is described by:

$$\begin{aligned}&\hat{U}_0(t_b,t_a;\gamma_{\text{PR}})|M_i\rangle\langle M_j|\hat{U}_0(t_b,t_a;\gamma_{\text{PR}})^{-1} =\\ &\exp\left(-i\sum_{\Lambda,l,\lambda}\Phi^{(\Lambda)}_{l0,\lambda 0}(t_b,t_a;\gamma_{\text{PR}})\Xi^{(\Lambda)}_{\lambda 0,M_i,M_j}\right)|M_i\rangle\langle M_j|.\end{aligned}\tag{2.44}$$

Here $\Xi^{(\Lambda)}_{\lambda 0,M_i,M_j}$ defines the symmetry order of rank λ of the spin transition from state $|M_j\rangle$ to $|M_i\rangle$, which is given by:

$$\Xi^{(\Lambda)}_{\lambda 0,M_i,M_j} = \langle M_i|\hat{t}^{(\Lambda)}_{\lambda 0}|M_i\rangle - \langle M_j|\hat{t}^{(\Lambda)}_{\lambda 0}|M_j\rangle.\tag{2.45}$$

We can notice that the acquired phase Eq.2.44 is a sum of the individual phases arising from each interaction Hamiltonian. If we would detect and Fourier transform the "signal" a spinning sideband manifold would emerge. We can show this explicitly by separating the phase factor in Eq.2.44 into a non-periodic part due to the evolution of the time-independent frequency components, and periodic part that we expand as a Fourier series:

$$\begin{aligned}\exp\left(-i\sum_{\Lambda,l,\lambda}\Phi^{(\Lambda)}_{l0,\lambda 0}(t,0;\gamma_{\text{PR}})\Xi^{(\Lambda)}_{\lambda 0,M_i,M_j}\right) &= \exp\left(-i\sum_{\Lambda(\text{ti}),l,\lambda}\omega^{(\Lambda)}_{c,l0,\lambda 0,0}\Xi^{(\Lambda)}_{\lambda 0,M_i,M_j}t\right)\\ &\times\sum_{\mu=-\infty}^{+\infty}A^{(\mu)}_{c,M_iM_j}(\gamma_{\text{PR}})\exp\left(-i\phi^{(\mu)}_{c,M_i,M_j}(\gamma_{\text{PR}})\right)\exp(-i\mu\omega_r t).\end{aligned}\tag{2.46}$$

Here $A^{(\mu)}_{c,M_iM_j}(\gamma_{\text{PR}})\exp\left(-i\phi^{(\mu)}_{c,M_iM_j}(\gamma_{\text{PR}})\right)$ are the complex Fourier coefficients expressed as:

$$\begin{aligned} &A^{(\mu)}_{c,M_iM_j}(\gamma_{\text{PR}})\exp\left(-i\phi^{(\mu)}_{c,M_iM_j}(\gamma_{\text{PR}})\right) = \\ &\qquad \frac{1}{\tau_r}\int_0^{\tau_r}\exp\left(-i\sum_{\Lambda(\text{td}),l,\lambda}\Phi^{(\Lambda)}_{l0,\lambda 0}(t,0;\gamma_{\text{PR}})\Xi^{(\Lambda)}_{\lambda 0,M_iM_j}\right)\exp(i\mu\omega_r t)dt. \end{aligned} \tag{2.47}$$

The labels $\Lambda(\text{ti})$ and $\Lambda(\text{td})$ represent the time-independent and -dependent interactions, respectively. The Fourier coefficients are composed of amplitudes and phases that are related to the symmetry order ($\Xi^{(\Lambda)}_{\lambda 0,M_i,M_j}$) and crystallite orientation. The Fourier series represents the spinning-sideband manifold of the anisotropic interactions. The formal description here, in principle, has shown the origin of the formation of sidebands in spinning solids. We note that the amplitude $A^{(\mu)}_{c,M_iM_j}(\gamma_{\text{PR}})$ is the intensity of the μth-order sideband and the phase $\phi^{(\mu)}_{c,M_iM_j}(\gamma_{\text{PR}})$ is the sideband phase.

We find it useful to employ symmetry properties first reported by Levitt [37], which show (see Paper III for more detail) that the sideband amplitude is independent of γ_{PR}, while the sideband phases have a well-defined γ_{PR} dependence:

$$A^{(\mu)}_{c,M_iM_j}(\gamma_{\text{PR}}) = A^{(\mu)}_{c,M_iM_j}(0) \equiv A^{(\mu)}_{c,M_iM_j}, \tag{2.48}$$

$$\phi^{(\mu)}_{c,M_iM_j}(\gamma_{\text{PR}}) = \phi^{(\mu)}_{c,M_iM_j}(0) - \Phi^{(\Lambda)}_{l0,\lambda 0}(\gamma_{\text{PR}}/\omega_r,0;0) + \mu\gamma_{\text{PR}}. \tag{2.49}$$

Therefore, the Fourier series coefficient amplitudes depend on α_{PR} and β_{PR}, but not on γ_{PR} and henceforth we define the μth order sideband amplitude as $A^{(\mu)}_{c,M_iM_j}$.

2.2.6 Average Hamiltonian theory

As discussed in Section 2.2.5 a general Hamiltonian does not self commute at different times, and so the propagator takes a form that is not practically applicable for analyzing spin dynamics. However, strategies that yield approximate solutions are available, such as, numerical simulations [38–40], Floquet theory [41–45] or average Hamiltonian theory (AHT) [33; 46; 47]. AHT and Floquet theory are most commonly employed to describe periodic Hamiltonians and cyclic propagators. However, here we only focus on AHT, in which the propagator is expressed as a function of a time-independent average Hamiltonian:

$$\hat{U}(t_b,t_a) = \exp\left(-i\overline{H}\tau_{ab}\right). \tag{2.50}$$

Here $\overline{H}$ is the average Hamiltonian and τ_{ab} is the time step $t_b - t_a$. The propagator describes the evolution over one complete period of the Hamiltonian, hence AHT is restricted to the observation of the density operator to time points that are integer multiples of the period. The average Hamiltonian ($\overline{H}$) can be expanded as a Magnus series [48]:

$$\overline{H} = \sum_{k=1}^{\infty}\overline{H}^{(k)}, \tag{2.51}$$

where $\overline{H}^{(k)}$ is the kth order average Hamiltonian. The first three terms have the following integral expressions:

$$\overline{H}^{(1)} = \frac{1}{\tau_{ab}} \int_{t_a}^{t_b} \hat{H}(t) dt, \tag{2.52}$$

$$\overline{H}^{(2)} = \frac{1}{2i\tau_{ab}} \int_{t_a}^{t_b} dt \int_{t_a}^{t} dt' \left[\hat{H}(t), \hat{H}(t')\right], \tag{2.53}$$

$$\begin{aligned}\overline{H}^{(3)} = \frac{-1}{6\tau_{ab}} \int_{t_a}^{t_b} dt \int_{t_a}^{t} dt' \int_{t_a}^{t'} dt'' \{ & \left[\hat{H}(t) \left[\hat{H}(t'), \hat{H}(t'')\right]\right] \\ + & \left[\hat{H}(t'') \left[\hat{H}(t'), \hat{H}(t)\right]\right] \}.\end{aligned} \tag{2.54}$$

The Hamiltonians do not describe the exact spin dynamics during the time period τ_{ab}, but allow the prediction of the average dynamics over this time interval. We can notice that the higher order average Hamiltonians become increasingly more complex, so the series is usually truncated with the first few orders. However, to still have an accurate description of the spin dynamics we need to ensure that the Magnus series converges rapidly for any time $t_a \leq t \leq t_b$. This condition is satisfied if the norm of the Hamiltonian $\left(||\hat{H}(t)||\right)$ is sufficiently small so that $||\hat{H}(t)||\tau_{ab} \ll 1$.

The convergence of the Magnus expansion can be improved by transforming the total Hamiltonian ($\hat{H}(t)$) into a suitable interaction frame. In Paper III the Hamiltonian is transformed into the interaction frame of the large anisotropic interaction(s) and AHT is applied to describe the spin dynamics.

2.2.7 Interaction-frame Hamiltonian

As discussed in Section 2.2.6 the form of the propagator is often rather complicated and so approximate solutions are found using AHT. However, in order to apply AHT successfully we need to transform into an interaction frame, in which the Magnus series would converge quickly. Consider a Hamiltonian of the system with a dominant contribution $\hat{H}_0(t)$ and a small contribution $\hat{H}_1(t)$:

$$\hat{H}(t) = \hat{H}_0(t) + \hat{H}_1(t). \tag{2.55}$$

If we choose $\hat{H}_0(t)$ so that the corresponding propagator $\hat{U}_0(t)$ has an exact solution, we can transform the small interaction into the frame of the dominant interaction as shown below:

$$\tilde{H}_1(t) = \hat{U}_0(t)^{-1} \hat{H}_1(t) \hat{U}_0(t) + i \left(\frac{d}{dt} \hat{U}_0(t)^{-1} \right) \hat{U}_0(t) \tag{2.56}$$

The Hamiltonian $\tilde{H}_1(t)$ represents the small interaction as viewed from the coordination frame of the dominant interaction. As a result the norm of the Hamiltonian $||\tilde{H}_1(t)||$ has been decreased and the convergence of the Magnus series would be improved.

The most common interaction frame in NMR is the rotating-frame (not to be confused with the rotor frame), in which the observer follows the rotation of the resonant part of the applied radio-frequency field.

2.3 Interactions in solid-state NMR

So far we have described the interactions in a very general form, so in this Section we review in more detail the most relevant interactions for present work. Usually NMR interactions are grouped as internal and external. External interactions are referred to as perturbations of the spin system arising from the instrument, whereas internal perturbations originate from the sample itself. The Zeeman interaction reviewed in Section 2.1 is an example of an external interaction, since it originates from the interaction of the nuclear magnetic moment with an external magnetic field. In this Section we will first review the nuclear spin interaction with radio-frequency (RF) fields, followed by an account of the most essential internal interactions to the present work.

2.3.1 Interaction with Radio-frequency pulses

RF pulse with constant amplitude and phase. The nuclear spin interacts with the magnetic field produced by a RF pulse as shown below:

$$\hat{H}_{\mathrm{RF}} = -\gamma_i \hat{\mathbf{I}}_i \cdot \mathbf{B}_{\mathrm{RF}}(t). \tag{2.57}$$

Typically RF pulses are applied in the transverse plane (the xy-plane) and so the time-dependent magnetic field of the pulse is given by:

$$\mathbf{B}_{\mathrm{RF}}(t) = 2B_1 \cos(\omega_{\mathrm{ref}} t + \phi_p) e_x, \tag{2.58}$$

where $2B_1$ and ϕ_p are the magnetic field amplitude and phase of the RF pulse, respectively. We note that the magnetic field produced by the RF pulse consists of two components a resonant and non-resonant. Transformation of the Hamiltonian into the interaction frame of the resonant component (and ignoring the non-resonant part) gives:

$$\hat{H}_{\mathrm{RF}} = \omega_{\mathrm{RF}} R_z(\phi_p) \hat{I}_x R_z(\phi_p)^{-1}, \tag{2.59}$$

where ω_{RF} is nutation frequency or more often we refer to it as the RF field amplitude. $R_a(\theta)$ is the rotation operator about a axis through angle θ.

Any nuclear spin components that are not parallel to the applied RF field will nutate about the RF field. Employing the density operator formalism we can illustrate an excitation pulse as follows:

$$\hat{I}_z \xrightarrow{\pi/2\hat{I}_x} -\hat{I}_y, \tag{2.60}$$

where the phase of the pulse is chosen to be 0, i.e. the magnetic field component of the RF pulse is along the x-axis by convention. While $\pi/2$ represents the flip angle $\beta_p = \omega_{\mathrm{RF}} \tau_p$, where τ_p is the pulse length.

The constant phase and amplitude pulses reviewed here are simple to implement experimentally and straightforward for analysing spin dynamics. However, in practice instrument limitations, such as RF inhomogeneity, give rise to a distribution of RF field amplitudes (and phases) across the sample, thus lead to a distribution of flips angles. [49] Furthermore, the excitation bandwidth (the span of frequencies that can be efficiently excited) of a pulse is inversely proportional to the pulse length, so longer pulses exhibit poorer excitation bandwidth. These effects can hinder the acquisition of intact NMR spectra, particularly when the nuclear spin systems we wish to study are subject to large anisotropic interactions.

RF pulse with time-dependent amplitude and phase. Improvement in the excitation bandwidth and response to RF inhomogeneity have been obtained by employing short high-power adiabatic pulses (SHAPs) . [50; 51] The basic principle behind adiabatic pulses is to lock the spin magnetization to an effective field (B_{eff}) and move the effective field so that population inversion or a specific change of coherences is achieved. The Hamiltonian of an adiabatic pulse is given by:

$$\hat{H}_1(t) = \omega_1(t)\hat{R}_z(\phi_\mathrm{p}(t))\hat{I}_x\hat{R}_z(\phi_\mathrm{p}(t))^{-1}, \tag{2.61}$$

where $\omega_1(t)$ is the time-dependent RF field amplitude and $\phi_\mathrm{p}(t)$ represents the time-dependent phase. To describe the effect of an adiabatic pulse on a spin system we would need to first transform the total Hamiltonian into the interaction representation of the RF phase, followed by a transformation into the first-adiabatic frame. [51] We have explained in detail this process in Paper I, here we only quote the resulting propagator:

$$\hat{U}_{\mathrm{SHAP}} = R_z(\phi_{\max})R_y(\pi)\exp(-i\xi_1 I_z)\exp\left(-i\xi_2\sqrt{\frac{2}{3}}\hat{T}_{20}\right)R_z^{-1}(\phi_{\max}). \tag{2.62}$$

In the derivation we have assumed that we have a single spin subject to the shift and first-order quadrupolar interactions. The phase $\phi_{\max} = \phi_\mathrm{p}(0) = \phi_\mathrm{p}(\tau_\mathrm{p})$ is the maximum phase value of the adiabatic pulse, τ_p is the pulse length, ξ_1 and ξ_2 are the phases acquired due to the shift or first-order quadrupolar interaction, respectively.

2.3.2 The chemical shielding interaction

The nuclear Zeeman Hamiltonian provides a correct description of the nuclear spin interaction with an external magnetic field of a bare nucleus. However, it is seldom that we study such systems, usually the nuclei are surrounded by electrons. In the presence of the magnetic field the electron motion induces a local magnetic field, which usually opposes the external magnetic field, thus shielding the nucleus. This is the so-called diamagnetic contribution of the shielding $\boldsymbol{\sigma}^{\mathrm{dia}}$. Moreover, the external magnetic field also distorts the electronic ground state by mixing in certain excited electronic states. The excited states provide a paramagnetic contribution to the shielding tensor $\boldsymbol{\sigma}^{\mathrm{para}}$. [52] Thus, the chemical shielding interaction is at the intersection between internal and external interactions. The general form of the chemical shielding Hamiltonian is given by:

$$\hat{H}_{\mathrm{IC}} = \gamma_I \mathbf{B}_0 \cdot \boldsymbol{\sigma} \cdot \hat{\mathbf{I}}, \tag{2.63}$$

where $\boldsymbol{\sigma} = \boldsymbol{\sigma}^{\mathrm{dia}} + \boldsymbol{\sigma}^{\mathrm{para}}$ is the chemical shielding tensor. In diamagnetic systems, i.e. systems without unpaired electrons, this chemical shielding tensor completely describes the shielding experienced by a nucleus and it has been denoted by Pennanen and Vaara as the orbital contribution $\boldsymbol{\sigma}^{\mathrm{orb}}$. [53] However, in paramagnetic systems we also need to take into account contributions due to the unpaired electrons ($\boldsymbol{\sigma}^{\mathrm{S}}$). Thus, the shielding for any system is described by the sum of the orbital term and the contribution arising from the unpaired electrons:

$$\boldsymbol{\sigma} = \boldsymbol{\sigma}^{\mathrm{orb}} + \boldsymbol{\sigma}^{\mathrm{S}}. \tag{2.64}$$

We describe the shielding interaction with unpaired electrons in more detail in Section 2.3.4.

We can transform the Hamiltonian in Eq.2.63 into the rotating frame and treat it as a perturbation to the Zeeman Hamiltonian, for which the first-order term is given by:

$$\hat{H}_{\mathrm{CS}}^{(1)} = -\omega_0 \left[-\sqrt{\frac{1}{3}}\sigma_{00} + \sqrt{\frac{2}{3}}\sigma_{20} \right] \hat{I}_z. \tag{2.65}$$

We notice that the chemical shielding tensor depends on the terms of spherical rank-0 and rank-2. The antisymmetric part of the tensor does not contribute to the observable signal, because the spin operators with rank-1 and order-0 are zero. The rank-0 term can be simplified and is referred to as the isotropic shielding $\sigma_{00} = -\sqrt{3}\sigma_{\mathrm{iso}}$. In experimental NMR we measure the chemical shift tensor $\boldsymbol{\delta}$ instead of the shielding. The shielding tensor and shift are related to each other via an isotropic shielding of a reference system as shown below:

$$\boldsymbol{\delta} = \sigma_{\mathrm{iso}}^{\mathrm{ref}} \mathbb{1} - \boldsymbol{\sigma}. \tag{2.66}$$

Since the two are related by a constant factor it is often that the definitions are used interchangeably. Throughout the Thesis and the Papers we will refer to it as the (chemical) shift interaction.

The shift Hamiltonian in the high-field approximation is given by:

$$\hat{H}_S = \Omega(\Omega_{\mathrm{SC}}, \Omega_{\mathrm{CL}}) \hat{I}_z. \tag{2.67}$$

Here $\Omega(\Omega_{\mathrm{SC}}, \Omega_{\mathrm{CL}})$ is the resonance frequency, which is expressed as:

$$\Omega(\Omega_{\mathrm{SC}}, \Omega_{\mathrm{CL}}) = \omega_0 \delta_{\mathrm{iso}} + \sqrt{\frac{2}{3}}\omega_0 \sum_{m'=-2}^{+2} \sum_{m=-2}^{+2} \tilde{\delta}_{2m'} D_{m'm}^{(2)}(\Omega_{\mathrm{SC}}) D_{m0}^{(2)}(\Omega_{\mathrm{CL}}), \tag{2.68}$$

where $\Omega_{\mathrm{SC}} = (\alpha_{\mathrm{SC}}, \beta_{\mathrm{SC}}, \gamma_{\mathrm{SC}})$ and $\Omega_{\mathrm{CL}} = (\alpha_{\mathrm{CL}}, \beta_{\mathrm{CL}}, \gamma_{\mathrm{CL}})$ are sets of Euler angles relating the principal axis frame (PAF) of the shift tensor to the crystal frame, and the crystal frame to the laboratory frame, respectively. $\tilde{\delta}_{2m'}$ are the rank-2 irreducible spherical tensor components of the shift tensor and are given by:

$$\tilde{\delta}_{20} = \sqrt{\frac{3}{2}}\Delta\delta, \tag{2.69}$$

$$\tilde{\delta}_{2\pm1} = 0, \tag{2.70}$$

$$\tilde{\delta}_{2\pm2} = -\frac{1}{2}\eta_{\mathrm{S}}\Delta\delta, \tag{2.71}$$

where $\Delta\delta$ and η_S are the shift anisotropy and the asymmetry parameter of the shift tensor, respectively. According to Haeberlen convention ($|\tilde{\delta}_{zz}-\delta_\mathrm{iso}| \geqslant |\tilde{\delta}_{xx}-\delta_\mathrm{iso}| \geqslant |\tilde{\delta}_{yy}-\delta_\mathrm{iso}|$) the shift parameters ($\delta_\mathrm{iso}$, $\Delta\delta$, η) are defined as follows [32]:

$$\delta_\mathrm{iso} = \frac{\tilde{\delta}_{xx}+\tilde{\delta}_{yy}+\tilde{\delta}_{zz}}{3}, \tag{2.72}$$

$$\Delta\delta = \tilde{\delta}_{zz}-\delta_\mathrm{iso}, \tag{2.73}$$

$$\eta_\mathrm{S} = \frac{\tilde{\delta}_{yy}-\tilde{\delta}_{xx}}{\Delta\delta}, \tag{2.74}$$

where $\tilde{\delta}_{zz}$, $\tilde{\delta}_{yy}$, $\tilde{\delta}_{xx}$ are the Cartesian tensor principal components of the shift tensor.

Finally, we discuss the symmetry order of the chemical shift interaction (or in general the shift interaction). As shown in Section 2.2.5 the evolution of an interaction depends on the symmetry order, which takes a specific value for each interaction and the nuclear spin transition. For the shift interaction the spin rank λ is 1, so according to Eq.2.45 for a transition from state $|M_j\rangle$ to state $|M_i\rangle$ symmetry order is given by:

$$p = M_i - M_j. \tag{2.75}$$

This is equivalent to the definition of the order p in Section 2.2.2. In Paper I and II we heavily use the symmetry order to facilitate the analysis of the refocussing properties of the pulse sequences.

2.3.3 The quadrupolar interaction

For nuclei with spin $I > 1/2$ the charge distribution of the nucleus is not spherical, meaning that the nucleus possesses a nuclear quadrupolar moment. The quadrupolar interaction arises due to the coupling between the nuclear quadrupole moment and the surrounding electric-field gradient (EFG). The symmetric and traceless EFG tensor is calculated as the second derivative of the electrostatic potential with respect to position. In the PAF, the EFG tensor $\mathbf{V}$ principal components are arranged according to the Haeberlen convention $|\tilde{V}_{zz}| \geqslant |\tilde{V}_{xx}| \geqslant |\tilde{V}_{yy}|$. [32] The EFG anisotropy and assymmetry are related to the Cartesian components as follows:

$$eq = \tilde{V}_{zz}, \tag{2.76}$$

$$\eta_Q = \frac{\tilde{V}_{yy}-\tilde{V}_{xx}}{\tilde{V}_{zz}}. \tag{2.77}$$

The general form of the Hamiltonian of the quadrupolar interaction is given by:

$$\hat{H}_\mathrm{IQ} = \frac{eQ}{2I(2I-1)h}\hat{\mathbf{I}}\cdot\mathbf{V}\cdot\hat{\mathbf{I}}. \tag{2.78}$$

Here, eQ is the nuclear quadrupolar moment. We define the quadrupole splitting frequency as:

$$\omega_Q^\mathrm{PAF} = \frac{3\pi C_Q}{2I(2I-1)}, \tag{2.79}$$

where C_Q is the quadrupolar coupling constant given by $C_Q = e^2qQ/h$.

As described earlier for the chemical shielding we treat the quadrupolar interaction as a perturbation to the Zeeman interaction. Thus, in the high-field approximation the first-order quadrupolar interaction Hamiltonian is expressed as [29; 46]:

$$\hat{H}_Q^{(1)} = \omega_Q(\Omega_{\mathrm{QC}},\Omega_{\mathrm{CL}})\left[\hat{I}_z^2 - \frac{1}{3}I(I+1)\hat{E}\right], \tag{2.80}$$

where $\omega_Q(\Omega_{\mathrm{QC}},\Omega_{\mathrm{CL}})$ is the quadrupolar splitting frequency for a nuclear spin, for which the PAF of the EFG tensor has an orientation in the crystal frame defined by the Euler angles $\Omega_{\mathrm{QC}} = (\alpha_{\mathrm{QC}},\beta_{\mathrm{QC}},\gamma_{\mathrm{QC}})$. Furthermore, the orientation of each crystallite is related to the laboratory frame by a set of Euler angles $\Omega_{\mathrm{CL}} = (\alpha_{\mathrm{CL}},\beta_{\mathrm{CL}},\gamma_{\mathrm{CL}})$. Thus, the quadrupolar splitting frequency is given by:

$$\omega_Q(\Omega_{\mathrm{SC}},\Omega_{\mathrm{CL}}) = \sqrt{\frac{2}{3}}\frac{\omega_Q^{\mathrm{PAF}}}{eq}\sum_{m'=-2}^{+2}\sum_{m=-2}^{+2}\tilde{V}_{2m'}D_{m'm}^{(2)}(\Omega_{\mathrm{QC}})D_{m0}^{(2)}(\Omega_{\mathrm{CL}}), \tag{2.81}$$

where $\tilde{V}_{2m'}$ are spherical tensor components of the EFG tensor and are given by:

$$\tilde{V}_{20} = \sqrt{\frac{3}{2}}eq, \tag{2.82}$$

$$\tilde{V}_{2\pm1} = 0, \tag{2.83}$$

$$\tilde{V}_{2\pm2} = \frac{1}{2}\eta_Q eq. \tag{2.84}$$

According to Eq.2.45 for a transition from state $|M_j\rangle$ to state $|M_i\rangle$ the symmetry order of the first-order quadrupolar interaction is given by:

$$d = M_i^2 - M_j^2. \tag{2.85}$$

The symmetry order d is often referred to as the satellite order. We see that for symmetric transitions, such as the central transition of half-integer quadrupolar nuclei and DQ transition for spin $I = 1$ are unaffected by the first-order quadrupolar interaction. Furthermore, the form of the coherence order and satellite order are different this will be exploited in Paper I and II to separate and correlate the two interactions.

In contrast to the shift interaction, truncation of the quadrupolar interaction Hamiltonian at the first-order does not provide a full description of the observed NMR spectra, thus higher-order terms are needed. The second-order average Hamiltonian is given by:

$$\begin{aligned}\hat{H}_Q^{(2)} = \frac{4(\omega_{\mathrm{Q}}^{\mathrm{PAF}})^2}{9\omega_0}\Bigg[&W_{00}\left(\frac{9}{5\sqrt{5}}\hat{t}_{30} + \frac{4I(I+1)}{5\sqrt{5}}\hat{t}_{10}\right)\\ &+W_{20}\left(-\frac{9}{5}\sqrt{\frac{2}{7}}\hat{t}_{30} + \frac{4I(I+1)-3}{10\sqrt{14}}\hat{t}_{10}\right)\\ &+W_{40}\left(-\frac{51}{4}\sqrt{\frac{1}{70}}\hat{t}_{30} - \frac{12I(I+1)-9}{10\sqrt{70}}\hat{t}_{10}\right)\Bigg],\end{aligned} \tag{2.86}$$

where the coefficient W_{L0} represents the coupled spatial tensor of two spherical tensor components as shown below:

$$W_{L0} = \sum_{m} \langle 22m-m|L0\rangle v_{2m} v_{2-m}. \tag{2.87}$$

Here $\langle 22m-m|L0\rangle$ are Clebsch-Gordan coefficients and v_{pk} are the spherical tensor components of the reduced EFG tensor $\mathbf{v} = \mathbf{V}/eq$. We can notice that the second-order quadrupolar interaction Hamiltonian depends on a rank-0, rank-2 and rank-4 tensor. The rank-0 term is spatially isotropic, but will lead to an additional contribution to the isotropic shift. The rank-2 and rank-4 are spatially anisotropic. The rank-4 interaction cannot be completely averaged by MAS and so the spinning sidebands exhibit a broadening due to this contribution.

2.3.4 The hyperfine interaction

In paramagnetic systems, i.e. systems with unpaired electrons, the nuclear magnetic moment can couple to the unpaired electron magnetic moment leading to the hyperfine interaction. The hyperfine coupling Hamiltonian is expressed as:

$$\hat{H}_{SI} = \hat{\mathbf{S}} \cdot \mathbf{A} \cdot \hat{\mathbf{I}}, \tag{2.88}$$

where $\hat{\mathbf{S}}$ represents the operator for electron spin and $\mathbf{A}$ is the hyperfine coupling tensor. In the non-relativistic approximation, the hyperfine coupling tensor can be separated into a rank-0 term and a rank-2 component as shown below:

$$\mathbf{A} = A^{\mathrm{FC}} \mathbb{1} + \mathbf{A}^{\mathrm{SD}}, \tag{2.89}$$

where A^{FC} is the Fermi contact (FC) term, which is purely isotropic (rank-0). $\mathbf{A}^{\mathrm{SD}}$ is the rank-2 spin-dipolar (SD) component. [54; 55]

The FC part of the hyperfine interaction is directly proportional to the unpaired electron density at the nuclear site. Physically this represents the delocalised unpaired electron density in the s-orbital centred at the nucleus. The spin density is transferred from the paramagnetic centre to the s-orbitals of the nucleus of interest via bonds, therefore allows to gain insights into the bonding network of the system. Whereas the SD component is a through space interaction between the nucleus and unpaired electron density. SD part leads to the so-called pseudo contact shift δ_{PC} and an additional anisotropic contribution to the chemical shift tensor.

In principle, the Hamiltonian in Eq.2.88 takes the form of a heteronuclear coupling and a splitting of the NMR resonances would be expected, however, experimentally we observe a contribution to the shift tensor instead. This can be explained by two properties of the electron spin. Firstly, the electron Zeeman interaction is much larger than the nuclear Zeeman interaction, which leads to an unequal population difference of the two nuclear transitions in the four level spin system (Fig.2.1(a)), thus different intensities of the two components of the doublet (Fig.2.1(b)). Secondly, electron relaxation times are significantly shorter than the nuclear relaxation times, which effectively “decouples” the NMR spectrum. [56] Therefore, the resulting singlet position is shifted due to the “paramagnetic shift” (Fig.2.1(b)).

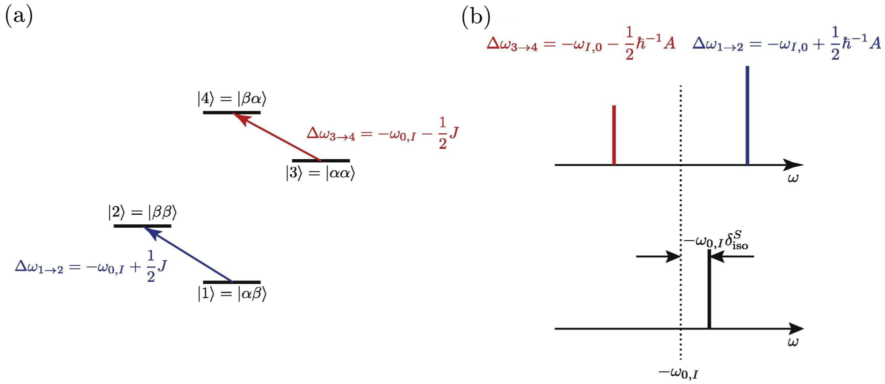
(a)
$|4\rangle = |\beta\alpha\rangle$
$\Delta\omega_{3\to4} = -\omega_{0,I} - \frac{1}{2}J$
$|3\rangle = |\alpha\alpha\rangle$
$|2\rangle = |\beta\beta\rangle$
$\Delta\omega_{1\to2} = -\omega_{0,I} + \frac{1}{2}J$
$|1\rangle = |\alpha\beta\rangle$
(b)
$\Delta\omega_{3\to4} = -\omega_{I,0} - \frac{1}{2}\hbar^{-1}A$
$\Delta\omega_{1\to2} = -\omega_{I,0} + \frac{1}{2}\hbar^{-1}A$
ω
$-\omega_{0,I}\delta^{S}_{\text{iso}}$
ω
$-\omega_{0,I}$

Figure 2.1: Illustration of the spin energy levels and NMR spectrum of a two-spin system I-S, where a nuclear spin $I = 1/2$ is coupled to an electron spin $S = 1/2$. In (a) is shown the array of four energy levels 1-4, assuming that $|\omega_{0,S}| > |\omega_{0,I}| > J$, $\omega_{0,S} > 0$, $\omega_{0,I} < 0$, and $J > 0$. The two I-spin transitions are shown with a red and blue arrow, and are labelled with their frequencies $\Delta\omega_{1\to2}$ and $\Delta\omega_{3\to4}$. The nuclear spin I spectrum is shown in (b) and exhibits diferent intensities of the two components of the doublet because the larger energy separation between the pairs of I-spin energy levels in the two transitions leads, via the Boltzmann distribution, to different equilibrium spin state population differences. The rapid electronic relaxation of S “decouples” the I spin spectrum to give a singlet which is positioned at the centre of mass of the two doublet components. The singlet is thus offset from $-\omega_{0,I}$ by an offset frequency $-\omega_{0,I}\delta^{\text{S}}_{\text{iso}}$, where $\delta^{\text{S}}_{\text{iso}}$ is the “paramagnetic shift” due to the electron S. Reproduced from [18], with permission of Elsevier.

For a paramagnetic insulator the FC part of the shift takes the form:

$$\delta_{\text{FC}} = \frac{2}{3}\rho^{\alpha-\beta}(0)\chi, \tag{2.90}$$

where $\rho^{\alpha-\beta}(0)$ is the unpaired electron density in the s-orbital and χ is the susceptibility per paramagnetic centre. However, a paramagnetic shift can also be observed in metals, which is referred to as the Knight shift K. [57; 58] In metallic systems the hyperfine interaction arises due to the nuclear spin interaction with the conduction electrons, i.e. electrons that are near the Fermi level. In conventional metals the FC part of the Knight shift [29; 59] is given by:

$$K_{\text{FC}} = \frac{2}{3}\langle|\phi_k(0)|^2\rangle_{E_F}\chi_{\text{P}}, \tag{2.91}$$

where $\langle|\phi_k(0)|^2\rangle_{E_F}$ is the average unpaired electron density of the s-band electrons near the Fermi level and χ_{P} is the Pauli susceptibility, which is directly proportional to the number of states at the Fermi level $N(E_F)$. For simple metals the Knight shift is temperature independent and the magnitude depends on the number of charge carriers at Fermi level.

For both paramagnetic insulators and metals the combination of large hyperfine couplings and stochastic fluctuations of the electronic magnetic moment lead to very fast longitudinal relaxation times (T_1) of the nuclear spin. Typically, this is the most significant contribution to the observed longitudinal relaxation in these systems. In simple metals, the FC term usually dominates the relaxation and it can be shown that the longitudinal relaxation T_1 is given by:

$$\frac{1}{T_1} = \frac{\pi}{9}\mu_0^2 \mu_B^2 \gamma_I^2 g_e^2 \hbar \langle |\phi_k(0)|^2 \rangle_{E_F} N(E_F) k_B T, \tag{2.92}$$

where μ_0 is the magnetic permeability in vacuum, μ_B is the Bohr magneton and g_e is the electron g-factor. From Eq.2.91 and 2.92 we can notice that for conventional metals the quantity $K_{FC}^2 T_1 T$ is constant. This is the so-called Korringa relation. [60] In Paper IV we use both the Korringa relation and differences in the form of the FC shift between paramagnetic insulators and metals to determine the electronic structure of barium titanium oxyhydride.

Finally, we note that bulk magnetic properties of the paramagnetic sample can also contribute to both the isotropic shift and the broadening of the resonances. [22; 61–64] In powders there exists a non-uniform distribution of crystal sizes, which can take any random orientation, since magnetic susceptibility is in general anisotropic each crystallite generates a unique magnetic field, which depends on the specific crystal structure, crystallite size and orientation. The produced inhomogeneous magnetic field in the sample leads to a distribution of isotropic shifts and shift anisotropies. Collectively, these effects are referred to as bulk magnetic susceptibility (BMS) effects.

2.4 Interpretation of NMR parameters

Thus far, we have focussed on the form of the interaction Hamiltonians and the evolution of the density operator. Here we continue by discussing the link between NMR parameters and properties of materials. Most commonly, the shift interaction is determined using NMR, which is related to the magnetic shielding of the nucleus. The shielding arises due to the induced electron orbital motion and the distortion of the electronic wavefunction by mixing with excited electronic states by the external magnetic field. Both effects are sensitive to the local electron distribution surrounding the nucleus and give rise to distinct isotropic shifts and shift anisotropies for different chemical substituents. For instance, in Paper A we measure the ^{15}N spectrum of nitrogen-doped graphene and identified pyridine and pyrolidine type nitrogen moieties (see Fig.2.2) based on the ^{15}N isotropic shift values. These local nitrogen environments were then linked to the catalytic activity in the material. In paramagnetic materials the hyperfine interaction between the nucleus and the unpaired electrons provides an additional contribution to the shift interaction, which can yield information about the nature of bonding, delocalisation of the unpaired electrons onto the atoms, ion dynamics and crystallite shape. [19–22] While the quadrupolar interaction is sensitive to the local geometry and the dynamics on the μs-ms timescale. [65–67] We note that the dipolar interaction between the nuclear spins gives information regarding the distance between two nuclei, which has proven to be remarkably valuable in determining the three-dimensional structures of biomacromolecules. [68] However, for the present discussion information extracted from the shift and quadrupolar interactions is the most relevant.

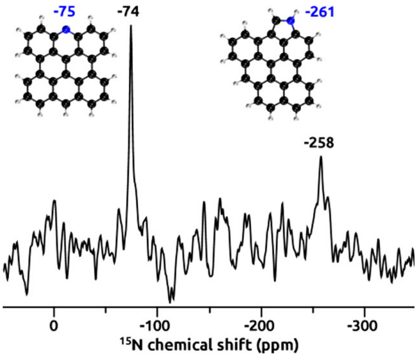

Figure 2.2: Directly excited ^{15}N MAS NMR spectra of the SK_N sample collected at 7 kHz MAS and 14.1 T, shown together with chemical shifts calculated for hypothetical structural motifs. Experimental chemical shifts are given in black, calculated ^{15}N shifts are in blue. All shifts are in ppm. Reproduced from Ref. [69] with permission from the Royal Society of Chemistry.

The interpretation of the measured NMR parameters in solids is rarely straightforward, and requires quantum chemical computations to rationalize the observed data. In Section 2.4.1 and 2.4.2 we review the basic principles of density functional theory in periodic solids and the subsequent calculation of EFG tensor parameters.

2.4.1 Basics of density functional theory

In order to calculate NMR parameters or any other quantity related to the electronic structure, we first must calculate the electronic structure, which is achieved by solving the time-independent Schrödinger equation:

$$\hat{H}\Psi(\mathbf{r}_1,\mathbf{r}_2,...,\mathbf{r}_N,\mathbf{R}_1,\mathbf{R}_2,...,\mathbf{R}_M) = E\Psi(\mathbf{r}_1,\mathbf{r}_2,...,\mathbf{r}_N,\mathbf{R}_1,\mathbf{R}_2,...,\mathbf{R}_M), \tag{2.93}$$

where $\hat{H}$ is the Hamiltonian, $\Psi(\mathbf{r}_1,\mathbf{r}_2,...,\mathbf{r}_N,\mathbf{R}_1,\mathbf{R}_2,...,\mathbf{R}_M)$ is the wavefunction composed of N electrons with positions $\mathbf{r}_i$ and M nuclei with positions $\mathbf{R}_j$ and E is the energy of the system. Since the electrons are much lighter than the nuclei and consequently move much faster it can be assumed that the nuclei are stationary with respect to the electrons. This is called the Born-Oppenheimer approximation and is applied to most quantum chemical calculations. [70]

Density functional theory (DFT) is based on the premise that the wavefunction can be expressed as a functional of the electron density $\rho(\mathbf{r})$. Development of DFT was pioneered by Hohenberg and Kohn, [71] who first showed that the external potential V_{ext}, hence energy E, is uniquely determined by the ground state density $\rho(\mathbf{r})$ and so the energy functional is given by:

$$E[\rho(\mathbf{r})] = F[\rho(\mathbf{r})] + \int V_{\text{ext}}(\mathbf{r})\rho(\mathbf{r})d\mathbf{r}. \tag{2.94}$$

The first term $F[\rho(\mathbf{r})]$ corresponds to the electron kinetic and electron-electron interaction energy, while second is due to electron interactions with an external potential $V_{\text{ext}}(\mathbf{r})$. Secondly, Hohenberg and Kohn demonstrated that the electron density corresponding to the energy minimum is that of the ground state. This implies that the variation principle can be employed for finding the ground state wavefunction. However, the exact form of the functional $F[\rho(\mathbf{r})]$ is unknown, so practical calculations are hindered. Improvement on the method was reported by Kohn and Sham who proposed that the system of N interacting electrons is replaced by a system of noninteracting N electrons with the same density $\rho(\mathbf{r})$. [72] Following this approach the functional $F[\rho(\mathbf{r})]$ is expressed as:

$$F[\rho(\mathbf{r})] = T_{\text{s}}[\rho(\mathbf{r})] + E_{\text{H}}[\rho(\mathbf{r})] + E_{\text{xc}}[\rho(\mathbf{r})], \tag{2.95}$$

where $T_{\text{s}}[\rho(\mathbf{r})]$ is the kinetic energy term of a non-interacting electron, $E_{\text{H}}[\rho(\mathbf{r})]$ is the electron-electron Coulombic energy functional (Hartree term) and $E_{\text{xc}}[\rho(\mathbf{r})]$ is the exchange-correlation functional, which describes deviation of the kinetic energy and Coulombic energy between the non-interacting system and the real system. Furthermore, Kohn and Sham expressed the density of the system $\rho(\mathbf{r})$ in terms of one-electron orthonormal orbitals as shown below:

$$\rho(\mathbf{r}) = \sum_{i=1}^{N} |\phi_i(\mathbf{r})|^2. \tag{2.96}$$

Starting with this definition of the electron density, Eq.2.95 can be minimized to obtain, the following one-electron Kohn-Sham equations:

$$\left(-\frac{1}{2}\nabla^2 + \int \frac{\rho(\mathbf{r}')}{|\mathbf{r}-\mathbf{r}'|} + V_{\text{ext}} + V_{\text{xc}}\right)\phi_i(\mathbf{r}) = \varepsilon_i \phi_i(\mathbf{r}), \tag{2.97}$$

where V_{xc} is the exchange-correlation potential given by:

$$V_{\text{xc}} = \frac{\delta E_{\text{xc}}[\rho(\mathbf{r})]}{\delta \rho(\mathbf{r})}. \tag{2.98}$$

The Kohn-Sham equations take a similar form to the Schrödinger equation. These equations can be solved following a self-consistent method. The procedure begins with a guess density and the calculation of the potentials. Afterwards, the Kohn-Sham equations are solved, which give a new set of single-electron orbitals and electron density. The new density is utilized in the second iteration, and so forth until the eigenvalues between two iterations do not change within a certain precision.

Apart from the Born-Oppenheimer approximation the DFT description has been exact, however, the form of the exchange-correlation functional is unknown. The main advantage of the current DFT formalism is that the energy contribution due to the exchange-correlation functional is significantly smaller than the single-electron kinetic or the Hartree term and approximations can be applied to the exchange-correlation functional. Thus, predominantly different DFT methods only differ in the form of the exchange-correlation functional. One of the simplest form, in which the exchange functional is approximated by treating the local electron density as a uniform gas. The method has been denoted as local density approximation (LDA), however, it performs poorly in most systems apart from metals. [73] An improvement in the method is obtained by assuming a nonuniform gas. In this approach the exchange-correlation functional depends both on the density and the first derivative of the density. The method is called the generalized gradient approximation (GGA). [74] The functional proposed by Perdew, Ernzerhof and Burke (PBE) [75] is one of the most popular GGA methods and is also used in Paper IV.

However, a significant problem remains, which is inherent to the DFT formulation reviewed above. An error arises due to the Coulombic energy term, which includes an interaction of the electron density with itself, hence has been called the self-interaction error. [76] Neither LDA or GGA approaches can compensate for the error, and these methods suffer from excessive delocalization of the electrons due to the self-repulsion of the electron density. Hybrid DFT, which includes a fraction of exact (Hartree-Fock) exchange energy, has been proposed to mitigate the self-interaction errors. [77] However, the calculation of the exact exchange is computationally expensive and may lead to overlocalization of electrons. Alternatively, the self-interaction error can be alleviated using a computationally less demanding approach, such as DFT+U. [78; 79] The method treats the delocalized states using a Hubbard model, while the rest of the electrons are treated with the conventional DFT formalism. Delocalization effects are most significant for d and f orbitals and, in general, the Hubbard-like term is added to electrons occupying these orbitals. The total DFT+U energy (including the additional on-site interaction energy) is expressed as follows:

$$\begin{aligned} E_{\text{tot}}^{\text{DFT+U}}[\rho(\mathbf{r})] &= E_{\text{tot}}^{\text{DFT}}[\rho(\mathbf{r})] \\ &+ \sum_{I}\left(\frac{U}{2}\sum_{m,\sigma\neq m',\sigma'} n_{m}^{I\sigma} n_{m'}^{I\sigma'} - \frac{U^{I}}{2} n^{I}(n^{I}-1)\right), \end{aligned} \tag{2.99}$$

where $E_{\text{tot}}^{\text{DFT}}[\rho(\mathbf{r})]$ is the standard DFT energy functional. The first term in the braces represents the Hubbard term, while the second term is a double counting correction, to account for the part included in the standard DFT functional interaction energy. $n_{m}^{I\sigma}$ are the occupation numbers defining an orbital on atom I, in state m with spin σ.

Typically, the U parameter is chosen so that calculated bandgap would be match the experimental value. [80] However, the U value can be determined without the use of experimental parameters. For instance, in Paper IV the U parameter is selected so that the total energy of the system is linearly dependent on filling a defect level, which is a property of an exact exchange-correlation functional described previously. [81]

2.4.2 DFT in periodic solids

Until now, we have not discussed the form of the Kohn-Sham orbitals. For isolated molecules we find it convenient to expand the orbitals in terms of a linear combination of atomic orbitals generating a basis set. In solids atoms comprise an infinitely periodic lattice, hence any physical quantity of the system is equivalent at points related by translation of the lattice constant. In calculations this is realized by employing the periodic boundary condition, which greatly reduces the size of the system. In a periodic lattice with a lattice vector **R** according to Bloch's theorem the single particle wavefunction can be expressed as a plane wave function:

$$\phi_{n,\mathbf{k}}(\mathbf{r}) = u_{n,\mathbf{k}}(\mathbf{r})\mathrm{e}^{i\mathbf{k}\cdot\mathbf{r}}, \tag{2.100}$$

where **k** is the wavevector of the cell. n defines different states at the same k-point. $u_{n,\mathbf{k}}(\mathbf{r})$ is a function with a periodicity of the lattice ($u_{\mathbf{k}}(\mathbf{r}) = u_{\mathbf{k}}(\mathbf{R}+\mathbf{r})$), which is expressed as a Fourier series:

$$u_{n,\mathbf{k}}(\mathbf{r}) = \frac{1}{\sqrt{\Omega}}\sum_{\mathbf{G}} c_{n,\mathbf{k},\mathbf{G}}\mathrm{e}^{i\mathbf{G}\cdot\mathbf{r}}. \tag{2.101}$$

Here Ω is the unit cell volume, **G** represents the reciprocal lattice vectors and $c_{n,\mathbf{k},\mathbf{G}}$ are Fourier coefficients. Thus, the single electron wavefunction is given by:

$$\phi_{n,\mathbf{k}}(\mathbf{r}) = \frac{1}{\sqrt{\Omega}}\sum_{\mathbf{G}} c_{n,\mathbf{k},\mathbf{G}}\mathrm{e}^{i(\mathbf{k}+\mathbf{G})\cdot\mathbf{r}} \tag{2.102}$$

It follows from Bloch's theorem that if $\phi_{n,\mathbf{k}}(\mathbf{r})$ is a solution, then $\phi_{n,\mathbf{k}+\mathbf{G}}(\mathbf{r})$ is as well. As a result the wavefunction can be evaluated in the first Brillouin zone (BZ) , which is the primitive reciprocal space unit cell. In principle, the BZ constitutes an infinite number of k-points, however, in practice, to reduce the computational demand the BZ is discretely sampled. In Paper IV we employ the k-point sampling method introduced by Monkhorst and Pack. [82] Furthermore, Eq.2.102 indicates that for a complete basis set the plane wave expansion contains an infinite number of vectors **G**. Therefore, the expansion is usually truncated to include a finite number of plane wave functions within a sphere of maximum kinetic energy, given by the energy cut-off (E_{cut}):

$$\frac{\hbar^2}{2m}|\mathbf{k}+\mathbf{G}|^2 \leq E_{\mathrm{cut}} \tag{2.103}$$

The parameter E_{cut} is typically chosen by examining the convergence of the total energy of the system with respect to E_{cut}. Needless to say, the computational effort scales with increasing E_{cut}. Close to the nucleus a large number of **G**-vectors (high E_{cut}) are required due to the rapid oscillations of the core electron wavefunctions. This complication is solved by applying the pseudopotential approximation, which assumes that the core electrons are essential unaffected by chemical bonding and can be considered as fixed (or frozen) in the atomic configuration. [83] In this treatment the core electrons are replaced by an effective field acting on the valence electrons. This potential is constructed such that the true wavefunction is reproduced beyond a specific distance from the nucleus, while the core electron wavefunctions are represented by a smooth pseudopotential.

The pseudopotential approach significantly reduces the computational effort, however, it fails in calculating physical properties at the nuclear sites, for instance, the EFG tensor. Accurate properties can be computed by reconstruction of the true all-electron density. Projector augmented wave (PAW) [84] approach has been proposed for calculation of these parameters, along with the extension of gauge invariant projector augmented wave (GIPAW) [85; 86] method. The PAW method employs a linear transformation to project the pseudo wavefunction corresponding to the core electrons onto the true all-electron wavefunction. This allows the calculation of the ground state charge density and subsequently the EFG tensor. We find these calculations very useful in Paper IV in order to determine the hydrogen occupancy in barium titanium oxyhydride.

3

Separation of the shift and quadrupolar interactions in static powders

Typically solid-state NMR is employed to study microcystalline powders. Crystallites in these samples take random orientations with respect to the applied magnetic field. For each crystallite orientation nuclear spins subject to anisotropic interactions lead to distinct signals the superposition of which is known as the powder pattern (see Fig.3.1(a)). A representative powder pattern spectrum of a spin $I = 1$ (or any other spin) subject to exclusively the shift interaction is shown in Fig.3.1(a). In an environment with an anisotropic electric-field gradient (EFG) the spin transitions of a spin $I = 1$ nucleus are also affected by the quadrupolar interaction. A powder spectrum of a spin $I = 1$ nuclei subject to the first-order quadrupolar interaction is given in Fig.3.1(b). The lineshape is often referred to as the Pake doublet. [87] The origin of the doublet can be viewed as the superposition of two mirror-image shift interaction powder pattern spectra arising from each of the transitions evolving in opposite direction (blue and orange in Fig.3.1(b)). In the case, when both interactions are present the spectrum becomes more complex (Fig.3.1(c)) and quantitative analysis of the interaction tensor parameters becomes complicated.

In principle these spectra can be obtained using the simplest NMR experiment, the one-pulse sequence. However, in practice we do not observe ideal performance of the sequence due to instrumental limitations. Firstly, the signal acquisition cannot be started immediately after the pulse, since the change from excitation to detection mode is not instantaneous. Secondly, the use of pulses with high RF field amplitude can introduce ringing artefacts at the beginning of the time domain signal (the free induction decay (FID)), which leads to severe

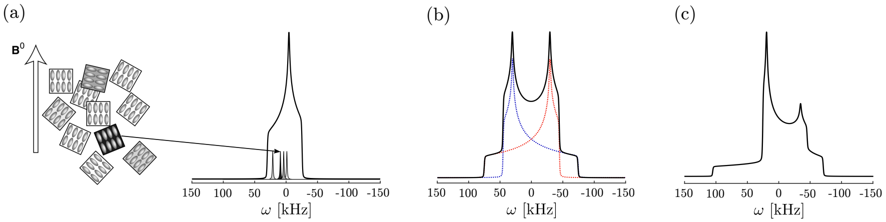

Figure 3.1: Simulated static NMR spectra of powders. (a) shows crystallites with different orientations with respect to the external magnetic field and the resulting spectra of four of these unique crystallite orientations. Superimposed is the overall powder pattern lineshape. The spin $I = 1$ nucleus is subject to only the shift interaction in this case. In (b) we have the spectrum of a spin $I = 1$ system subject to only the first-order quadrupolar interaction. Superimposed are the spectra of each of the two transitions shown in orange and blue. (c) shows the spectrum of a spin $I = 1$ nucleus subject to both the shift and first-order quadrupolar interactions. In the simulations shift tensor parameters are $\delta_{\text{iso}} = 0$, $\Delta\delta = 500$ ppm and $\eta_{\text{S}} = 0.7$ and the quadrupolar tensor parameters are $C_{\text{Q}} = 100$ kHz and $\eta_{\text{Q}} = 0.2$. Apdated from [88] with permission of Wiley.

distortions of the baseline in the frequency domain. These issues are usually mitigated by including a delay, called the dead time δ_{de}, before the start of the acquisition (see Fig.3.2(a)). However, evolution due to both the isotropic and anisotropic interactions commences with excitation of transverse magnetization. Hence incorporation of the dead time in the sequence neglects the first few points of the FID and the beginning of the evolution as a result induces considerable phase dispersion across the spectrum as shown in Fig.3.2(a). These effects are exacerbated for very broad resonances (as observed in systems with paramagnetic shift and quadrupolar interactions), since the period of evolution of the interaction decreases and a larger phase is accrued due to the interaction for the same dead time length.

For a spin $I = 1/2$ system (or spin $I = 1$ subject to a negligible quadrupolar interaction) this has been resolved by using the spin- (p-) echo sequence given in Fig.3.2(b), [89] which incorporates the dead time into the second delay τ. The $\pi/2$ pulse is the excitation pulse followed by a π pulse sandwiched in between two delays τ. The second part of the sequence ($\tau - \pi - \tau$) has the property of refocussing interactions dependent on coherence p. The refocussing properties of the sequence are explained as follows: the isotropic and anisotropic shift interactions are time-independent in the present case and so the accrued phase during the first period τ is given by $\Omega_{\text{S}}\tau$. The π pulse changes the sign of the coherence order p, hence the acquired phase during the second delay is $-\Omega_{\text{S}}\tau$. The overall phase cancels at the end of this sequence, thus at the beginning of the signal acquisition the shift interaction is refocussed. This is illustrated in Eq.3.1 using single element operators.

$$\hat{I}_{+}^{(+1,0)} \xrightarrow{\hat{H}_{\text{S}}\tau} \exp[-i\Omega_{\text{S}}\tau]\hat{I}_{+}^{(+1,0)} \xrightarrow{\pi\hat{I}_x} \exp[-i\tau\Omega_{\text{S}}]\hat{I}_{-}^{(0,-1)} \xrightarrow{\hat{H}_{\text{S}}\tau} \hat{I}_{-}^{(0,-1)} \tag{3.1}$$

Therefore, all the points of the FID are collected and the spectrum remains free of any phase dispersion. However, the evolution due to the first-order quadrupolar interaction depends on the satellite order d and would not be refocussed by the spin-echo sequence. The refocussing

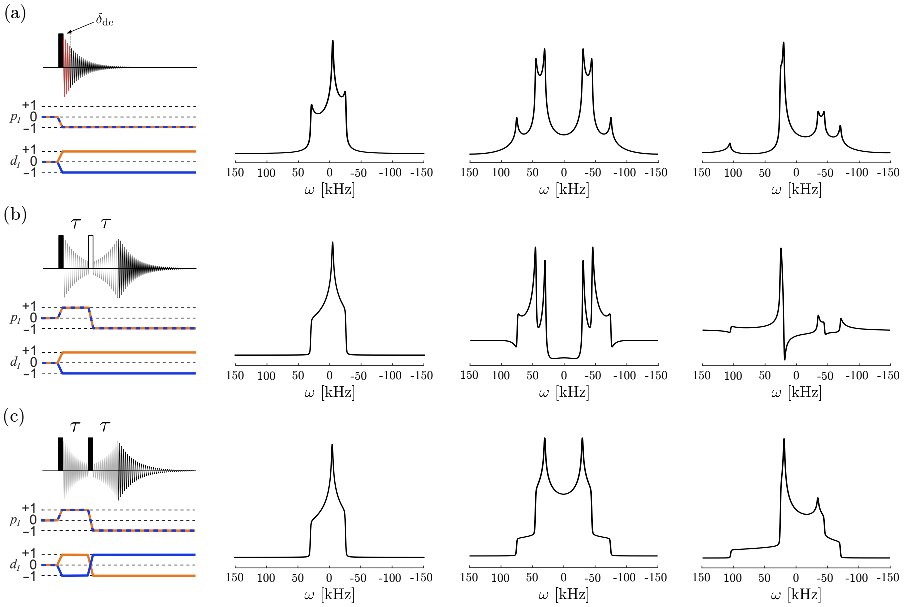

Figure 3.2: Sequences for acquiring 1D NMR spectra. On the left pulse sequences along with symmetry pathways are shown for the single pulse with a dead time (a), spin-echo (b) and solid-echo (c) experiments. On the right side are shown the corresponding simulated spectra for a spin $I = 1$ nucleus subject to either the shift, first-order quadrupolar or both interactions. Here the filled rectangle and empty rectangle represent $\pi/2$ and π, respectively. For simulations shift tensor parameters are $\delta_{\text{iso}} = 0$, $\Delta\delta = 500$ ppm and $\eta_{\text{S}} = 0.7$ and the quadrupolar tensor parameters are $C_{\text{Q}} = 100$ kHz and $\eta_{\text{Q}} = 0.2$.

properties of the sequence are demonstrated with simulations for different interactions in Fig.3.2(b).

The solid-echo sequence given in Fig.3.2(c) can be employed to refocus the evolution of both interactions or just the first-order quadrupolar interaction. [90; 91] In analogy to the spin-echo sequence the first pulse excites the coherences and is followed by an evolution period τ and a refocussing pulse.

$$\begin{aligned}&\hat{I}_{+}^{(+1,0)} \xrightarrow{[\hat{H}_{\text{S}}+\hat{H}_{\text{Q}}]\tau} \exp[-i\tau(\omega_{\text{Q}}+\Omega_{\text{S}})]\hat{I}_{+}^{(+1,0)} \xrightarrow{\pi/2\hat{I}_x} \\ &\frac{1}{2}\exp[-i\tau(\omega_{Q}+\Omega_{\text{S}})]\hat{I}_{+}^{(0,-1)} + \frac{1}{2}\exp[-i\tau(\omega_{Q}+\Omega_{\text{S}})]\hat{I}_{-}^{(+1,0)}\end{aligned} \tag{3.2}$$

We notice that the second $\pi/2$ pulse generates two terms with positive $\hat{I}_{+}^{(0,-1)}$ and negative $\hat{I}_{-}^{(+1,0)}$ coherence as shown in Eq.3.2. The two operators have the same satellite order d, which is opposite to the initial operator $\hat{I}_{+}^{(+1,0)}$. Employing coherence selection methods [92] we can choose to retain one of the two terms in the second line of Eq.3.2. If we select the first term a d-echo is formed, while the shift interaction evolves throughout the period 2τ:

$$\xrightarrow{\text{select}\,p=+1} \frac{1}{2}\exp[-i\tau(\omega_Q+\Omega_{\mathrm{S}})]\hat{I}_{+}^{(0,-1)} \xrightarrow{[\hat{H}_{\mathrm{S}}+\hat{H}_{\mathrm{Q}}]\tau} \frac{1}{2}\exp[-2i\tau\Omega_{\mathrm{S}}]\hat{I}_{+}^{(0,-1)}. \tag{3.3}$$

On the other hand if we select the second term both p- and d-echoes are formed, effectively refocussing the evolution due to both the first-order quadrupolar and the shift interaction as shown below:

$$\xrightarrow{\text{select}\,p=-1} \frac{1}{2}\exp[-i\tau(\omega_Q+\Omega_{\mathrm{S}})]\hat{I}_{-}^{(0,1)} \xrightarrow{[\hat{H}_{\mathrm{S}}+\hat{H}_{\mathrm{Q}}]\tau} \frac{1}{2}\hat{I}_{-}^{(0,1)}. \tag{3.4}$$

Furthermore, we illustrate the refocussing of both interactions with simulations in Fig.3.2(c), which show intact spectra in all three cases with the shift or first-order quadrupolar interactions only and the combination of the two. However, Eq.3.4 also alludes to a significant disadvantage of the sequence that the sensitivity is reduced by a factor of two, since we retain only half of the available signal components. Nevertheless, the solid-echo is a valuable sequence for acquiring spectra of spin $I = 1$ nuclei. Moreover, the 1D spectra, in which the shift or the first-order quadrupolar interaction dominate (see Fig.3.1(a) and 3.1(b)) can be used to extract the tensor parameters of the dominating interaction. For systems in which both interactions are of similar magnitude the individual NMR parameters are not readily extracted (see Fig.3.1(c)). The interpretation of the NMR data is particularly complicated in paramagnetic systems, which give rise to featureless spectra due to the combination of large shift anisotropies, BMS effects and the quadrupolar interaction.

This issue has been addressed previously by employing methods for separation of the shift (including the isotropic shift, shift anisotropy, and BMS contributions) and first-order quadrupolar interactions. Two classes of such sequences have been reported the shifting echo [93; 94] and the asymmetric π-pulse-inserted quadrupole-echo [95; 96] experiments. However, the sequences display suboptimal performance for routine applications due to either low sensitivity or poor excitation bandwidth. Moreover, the resulting spectra from each sequence are often contaminated with a sharp artefact. In Paper I we examine the shifting echo sequences and rationalize how the methods can be improved by employing adiabatic pulses. Our findings are summarised in Sections 3.1 and 3.2.

3.1 Shifting *p*- and *d*-echo sequences

Antonijevic and Wimperis pioneered a two-dimensional (2D) static NMR experiment for separating the shift from the first-order quadrupolar interaction. [93] The sequence consists of three $\pi/2$ pulses as shown in Fig.3.4(a). The first pulse excites the coherences, while the second is a solid-echo that forms a d-echo at $t = t_1$, but allows the interactions dependent on p to evolve. Consequently, the evolution due to the first-order quadrupolar interaction is refocussed, while the shift interaction evolves for the duration of t_1. The last pulse acts as a second solid-echo during which the evolution is refocussed of both interactions. As a result, in the acquisition period a d-echo forms at $t_2 = 0$, while a p-echo at $t_2 = t_1$. The

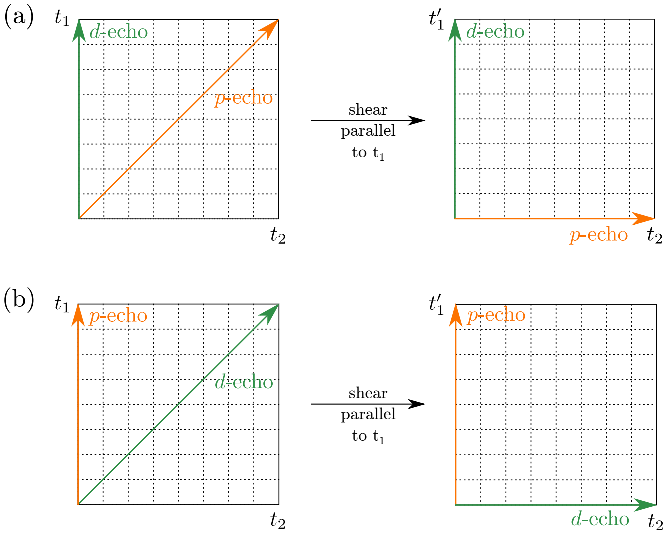

Figure 3.3: Schematic representation of the time domain shifting *p*- and *d*-echo experiments. (a) and (b) show the respective shifting *p*- and *d*-echo experiment time domain data before and after shearing. The green and orange arrows represent *d*- and *p*-echo ridges in the time domain. Reproduced from [97], with permission of Elsevier.

echo ridges in the 2D time domain data are illustrated schematically in Fig.3.3(a). Since the position of the *p*-echo in the time domain moves with increasing t_1 the sequence has been called as the shifting *p*-echo. Signal detection in the sequence begins after the final $\pi/2$ pulse so that the whole echo is acquired and pure 2D absorption-mode lineshapes are obtained after Fourier transform. The 2D frequency-domain projection onto the indirect dimension ω_1 would give a lineshape corresponding to the shift interaction, while the lineshape in the direct dimension ω_2 consists of a convolution of both the shift and the first-order quadrupolar interaction. Complete separation of the two interactions is achieved by applying a shearing transformation parallel to t_1 with a shear ratio $\kappa = -1$. After the shearing transformation the *p*-echo ridge becomes parallel to the t_2 axis (see Fig.3.3(a)), hence the shift interaction does not evolve in this dimension. A simulated Fourier transformed and sheared spectrum is provided in Fig.3.4(a). Pure shift and first-order quadrupolar interactions are observed in the projections onto each of the axis, which allows extraction of the tensor principal components. Furthermore, the 2D lineshape can be used to determine the Euler angles relating the two tensors.

Walder et al. devised an alternative sequence for separation of the two interactions that has a higher sensitivity, but a poorer excitation bandwidth. [94] The difference in the performance between the sequences arises due to the substitution of the second $\pi/2$ pulse with a π pulse (see Fig.3.4(a),(b)). The π pulse forms a spin-echo during t_1 period, which refocusses the evolution of the shift interaction, while the first-order quadrupolar interaction evolves. The final $\pi/2$ pulse, in analogy to the previous sequence, generates p- and d-echoes. However, in this case the p-echo forms at the time point $t_1 = 0$, while the d-echo at $t_2 = t_1$, consequently the pulse sequence is designated as the shifting d-echo experiment. Similarly as before a shearing transformation with the same coefficient is required for complete separation of the two interactions (see Fig.3.3(b)). In contrast to the preceding experiment the pure interaction lineshapes are located on the orthogonal axis as shown in the simulated spectrum in Fig.3.4(b). As discussed earlier a solid-echo selects only half of the signal components, therefore the use of a π pulse doubles the detected signal intensity. Although the longer pulse duration leads to a reduction in the excitation bandwidth.

In Paper I we examine the performance of the two pulse sequences on ^{2}H in deuterated copper(II) chloride dihydrate and deuterated barium titanium oxyhydrides. The sheared and Fourier transformed experimental ^{2}H spectra of $CuCl_2 \cdot 2D_2O$ are given in Fig.3.4(a) and 3.4(b). For both experiments besides the expected 2D ^{2}H lineshape we observe a sharp artefact in the middle of the quadrupole dimension. The artefact emerges as a result of flip-angle misset and pulse imperfections such as finite-pulse effects and RF inhomogeneity. Assuming that these effects account for a pulse flip angle error of ε, the signal components present in the shifting p-echo sequence after the t_1 period are given below:

$$\hat{I}_+^{(+1,0)} \rightarrow \frac{1}{2}\exp[-i\Omega_S t_1]\hat{I}_+^{(0,-1)} - \frac{1}{2}\varepsilon \exp[-i(\Omega_S + \omega_Q)t_1]\hat{I}_+^{(+1,0)}. \tag{3.5}$$

We see that two terms are available, which have the same coherence order, but different satellite order. Hence the terms cannot be separated with phase cycling, since only p coherences are selected explicitly, while d coherences are selected indirectly. The second term arises from an unwanted symmetry order pathway, in which the sign of both p and d remain unchanged after the second $\pi/2$ pulse. Therefore, the phase factor in the latter term shows that both the shift and the first-order quadrupolar interaction have evolved during t_1 and will lead to an artefact appearing along the anti-diagonal $\omega_1 = -\omega_2$. Following the shearing transformation described above the artefact will be positioned at zero frequency in the quadrupole dimension as observed in Fig.3.4(a).

For the shifting d-echo sequence the artefact will also occur due to the appearance of unwanted d pathways. We show that at the end of t_1 the operator has evolved as:

$$\hat{I}_-^{(0,-1)} \rightarrow (1-3\varepsilon^2)\exp[-i\omega_Q t_1]\hat{I}_+^{(+1,0)} + 2\varepsilon^2\hat{I}_+^{(0,-1)}. \tag{3.6}$$

The second term originates from an unwanted symmetry order pathway, in which the sign of both the p and d coherences have changed. This leads to the simultaneous refocussing of the evolution of the shift and first-order quadrupolar interaction, hence a sharp peak appears in the quadrupole dimension.

To summarise, here we have demonstrated that the shifting p- and d-echo sequences achieve separation of the shift and first-order quadrupolar interactions, however, the spectra are readily contaminated with an artefact resulting from unwanted symmetry order pathways. These artefacts interfere with the signal of interest and complicate the interpretation the spectra, particularly when multiple local ^{2}H environments are present. In Section 3.2 we introduce new sequences which are void of any artefacts and achieve broadband excitation.

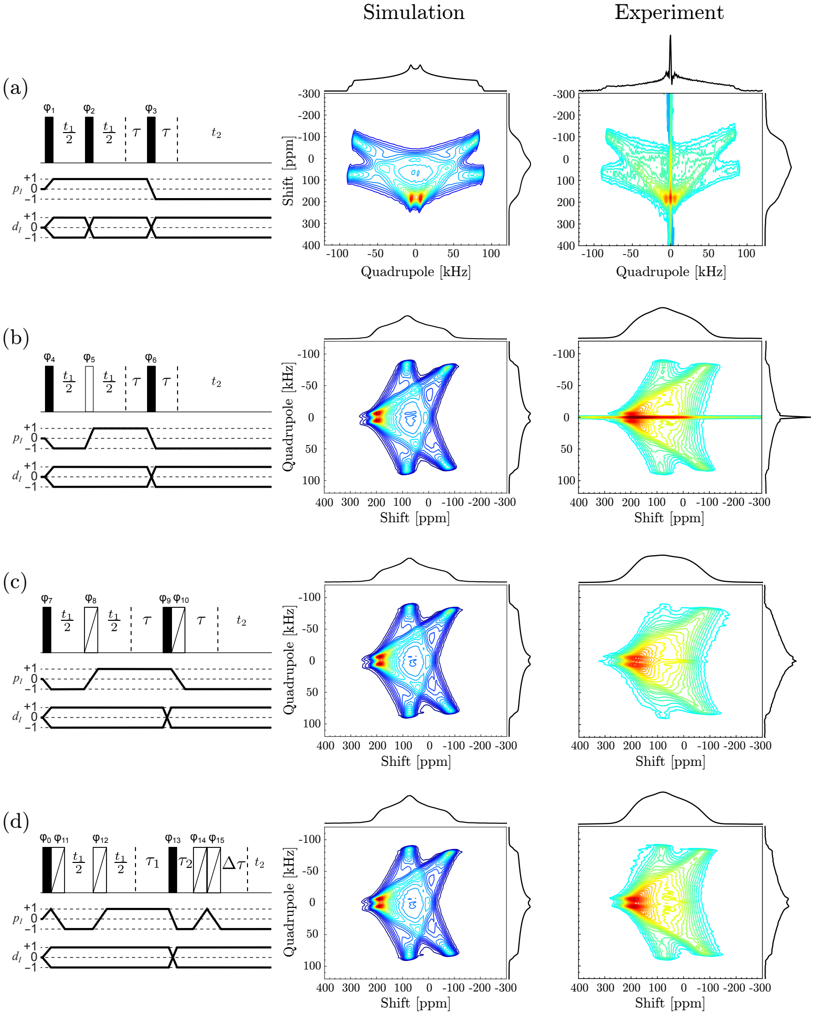

Figure 3.4: 2D spectra and pulse sequences for separation and correlation of shift and first-order quadrupolar interactions. Shifting p- (a), shifting d- (b), double adiabatic shifting d- (c) and quadruple adiabatic shifting d- (d) echo sequences and the corresponding experimental and simulated 2D spectra of ^{2}H in $CuCl_2{\cdot}2D_2O$. Here the filled rectangle, empty rectangle and rectangle with a diagonal represent $\pi/2$, π and adiabatic pulses, respectively. Time periods t_1 and t_2 are the evolution periods in the indirect and direct dimension, respectively, and τ, τ_1, τ_2, $\Delta\tau = \tau_1 - \tau_2$ are free precession periods to facilitate correct echo formation. p_I and d_I are the symmetry pathways for the experiments. Reproduced from [97], with permission of Elsevier.

3.2 Adiabatic shifting *d*-echo sequences

In Paper I we demonstrate that the issues of the two pulse sequences outlined in the Section 3.1 can be overcome by implementing adiabatic pulses. Application of a single short-high power adiabatic pulse (SHAP) to a spin $I = 1$ nucleus subject to both shift and first-order quadrupolar interactions induces a sign change of the coherence order p, however, a phase is accrued during the SHAP due to the evolution of the two interactions:

$$\hat{I}_{-}^{(0,-1)} \xrightarrow{\hat{U}_{\mathrm{SHAP}}} -\exp[i(\xi_{\mathrm{S}} - \xi_{\mathrm{Q}} - 2\phi_{\mathrm{max}})]\hat{I}_{+}^{(+1,0)}. \tag{3.7}$$

The propagator $\hat{U}_{\mathrm{SHAP}}$ expresses the transformation of a spin $I = 1$ nucleus throughout a SHAP as defined in Eq.2.62. ξ_{S} and ξ_{Q} are the accrued phases resulting from the evolution of the shift and first-order quadrupolar interaction, respectively. The additional phase $2\phi_{\mathrm{max}}$ emerges from the time-dependent adiabatic pulse phase function. Together these phases will induce distortions across the spectrum. In order to remove the unwanted phase factor the excitation sculpting principle is employed. [98; 99] More specifically a tandem of SHAPs, otherwise called the double adiabatic echo sequence, is used for spin $I = 1/2$ nuclei to cancel the accrued phases due to the shift evolution and the pulse phase as shown below:

$$-\exp[i(\xi_{\mathrm{S}} - \xi_{\mathrm{Q}} - 2\phi_{\mathrm{max}})]\hat{I}_{+}^{(+1,0)} \xrightarrow{\hat{U}_{\mathrm{SHAP}}} \exp[-2i\xi_{\mathrm{Q}}]\hat{I}_{-}^{(0,-1)}. \tag{3.8}$$

We notice that the phase due to the first-order quadrupolar interaction remains, since the sign of the satellite order d was unaffected by the SHAPs. For the same reason the sequence fails to refocus the evolution due to the first-order quadrupolar interaction during the interpulse delays, which have been ignored in Eq.3.8 to facilitate the current discussion.

Introduction of a $\pi/2$ pulse between the two SHAPs will effectively refocus both interactions and remove any accrued phases resulting from the SHAPs. Choosing the operator in Eq.3.7 as the starting point we can show that the density operator at the end of the sequence is free of any phase factors:

$$\begin{aligned} &-\exp[i(\xi_{\mathrm{S}} - \xi_{\mathrm{Q}} - 2\phi_{\mathrm{max}})]\hat{I}_{+}^{(+1,0)} \xrightarrow{\pi/2\hat{I}_x} \xrightarrow{\text{select } p=+1} \\ &-\tfrac{1}{2}\exp[i(\xi_{\mathrm{S}} - \xi_{\mathrm{Q}} - 2\phi_{\mathrm{max}})]\hat{I}_{+}^{(0,-1)} \xrightarrow{\hat{U}_{\mathrm{SHAP}}} \tfrac{1}{2}\hat{I}_{-}^{(+1,0)}. \end{aligned} \tag{3.9}$$

Again we have omitted the evolution of the interactions during the interpulse delays to simplify the equation. Another approach for refocussing both of the interactions and cancelling any unwanted phases arising from the SHAPs would be to position a pair of SHAPs before and after the $\pi/2$ pulse. Beginning with the density operator after the double adiabatic echo in Eq.3.8 we explicitly show that the accrued phases are removed using this arrangement of pulses:

$$\begin{aligned} &\exp[-2i\xi_{\mathrm{Q}}]\hat{I}_{-}^{(0,-1)} \xrightarrow{\pi/2\hat{I}_x} \xrightarrow{\text{select } p=+1} \tfrac{1}{2}\exp[-2i\xi_{\mathrm{Q}}]\hat{I}_{+}^{(0,-1)} \xrightarrow{\hat{U}_{\mathrm{SHAP}}} \\ &-\tfrac{1}{2}\exp[-i(\xi_{\mathrm{S}} + \xi_{\mathrm{Q}} - 2\phi_{max})]\hat{I}_{-}^{(-1,0)} \xrightarrow{\hat{U}_{\mathrm{SHAP}}} \tfrac{1}{2}\hat{I}_{+}^{(0,-1)}. \end{aligned} \tag{3.10}$$

We continue by demonstrating that these sequences can be employed for separating and correlating the shift and first-order quadrupolar interactions. Provided that we choose the pulse timings according to the pulse schemes given in Fig.3.4(c) and 3.4(d) the two sequences yield analogous spectra to the shifting d-echo sequence. Therefore, the sequences are denoted as the double adiabatic shifting d-echo (see Fig.3.4(c)) and quadruple adiabatic shifting d-echo (see Fig.3.4(d)) experiments, respectively.

In the former sequence the first adiabatic pulse refocusses the shift interaction during the t_1 period. The $\pi/2$ pulse inverts the sign of satellite order d, while the adjoining SHAP changes the p order to generate p- and d-echoes at the same position in time as for the conventional shifting d-echo experiment. Under ideal conditions the obtained spectra using the two shifting d-echo sequences are indistinguishable as shown by simulations in Fig.3.4(b) and 3.4(c). In practice, instrumental limitations such as insufficient RF power and RF inhomogeneity lead to the appearance of a sharp artefact in the conventional experiments. However, adiabatic pulses are impervious to RF field inhomogeneity provided the adiabatic condition holds, hence substitution of the second pulse in the sequences with a SHAP would remove or significantly reduce the artefact. This is confirmed by the sheared ^{2}H 2D spectrum of $CuCl_2 \cdot 2D_2O$ acquired using the double adiabatic sequence shown in Fig.3.4(c). As expected the artefact is almost negligible, however, the overall 2D lineshape of the signal is distorted. The observed distortion in the spectrum can be explain by pulse angle errors in the second $\pi/2$, which lead to an incomplete elimination of the accrued phases during the SHAPs.

In the quadruple shifting d-echo sequence (Fig.3.4(d)) the first pair of SHAPs refocusses the evolution of the shift interaction during t_1 and removes phase errors due to the shift interaction and the pulse phase. The following $\pi/2$ pulse reverses the signs of p and d orders, while the second pair of SHAPs effectively leaves the symmetry orders unchanged, but cancels the accrued phase due to the evolution of the first-order quadrupolar interaction during the first pair of SHAPs. Therefore, p- and d-echoes form at the same time points as in the previous shifting d-echo sequences. Since each pair of SHAPs cancel part of the phase error, the overall elimination of the accrued phase should improve. This conjecture is supported by the experimental ^{2}H spectrum in Fig.3.4(d), which shows an artefact-free intact 2D lineshape. The correctness of the 2D lineshape was further verified by extracting the shift and quadrupole tensor parameters along with the Euler angles, which match well with previously reported values. [93; 94]

In conclusion, the new shifting d-echo sequence containing four SHAPs yields artefact-free spectra with undistorted 2D lineshapes. Moreover, the sequence has a greater excitation bandwidth than the conventional shifting d-echo, while maintaining the same sensitivity. However, the sequence may not be suitable for investigating systems with spin $I = 1$ nuclei, which exhibit very short coherence lifetimes due to the relatively long pulse length of SHAPS (each 50 μs). Nevertheless, we conclude that the new quadruple adiabatic shifting d-echo sequence is superior to the previous pulse schemes for separation and correlation of the shift and first-order quadrupolar interactions. In Paper IV we apply the novel sequence to study the hydride local environment and the electronic structure in the barium titanium oxyhydrides.

4

Separation of the shift and quadrupolar interactions in spinning powders

In the Chapter 3 we introduced some of the most elegant static solid-state NMR sequences. However, these experiments exhibit very low sensitivity and resolution, on the account of the signal extending over a continuum of frequencies under static conditions. Sample spinning can increase both the sensitivity and resolution, since the anisotropic interactions are averaged concentrating the signal into discretely spaced sidebands as shown in Fig.4.1(c) and 4.1(d). [100; 101] The origin of sidebands is explained by the periodically time-dependent modulation of the spatial part of the interactions, while the remaining time-independent components broaden the spinning sidebands. For interactions with space rank-2, such as the shift and first-order quadrupolar interactions, the time-independent contribution is removed by rotating about an axis at the "magic-angle" ($\beta_{\mathrm{RL}} = \arctan\sqrt{2}$) with respect to the main magnetic field. Therefore, magic-angle spinning (MAS) provides an additional improvement in the resolution for rank-2 interactions.

The form of the spinning sideband manifold is affected by the spinning frequency. For instance, when the MAS frequency exceeds the span of frequencies in a stationary sample (Δ) due to the combination of all anisotropic interactions the majority of the signal is concentrated into the centreband (the sideband located at the isotropic position) and the spectrum is void of any orientation-dependent information (Fig.4.1(c)). While at "slower" spinning frequencies ($\Delta > \omega_r$) spectra contain sidebands, which encode the anisotropic part of the interactions, and allows the extraction of the tensor parameters (Fig.4.1(d)). However, as discussed in Chapter 3 the presence of several interactions in static spectra of spin $I = 1$ nuclei can impose

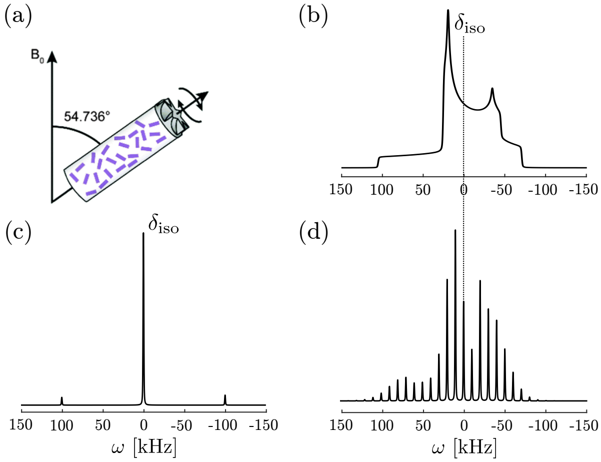

Figure 4.1: NMR spectra of a powder sample under MAS. (a) Schematic showing the MAS rotor oriented at the magic-angle with respect to the external magnetic field. Simulated powder spectra of a spin $I = 1$ system subject to the shift and first-order quadrupolar interaction under static conditions (b), 10 kHz MAS (c) and 100 kHz MAS (d). Reproduced from Ref. [102] with permission from the Royal Society of Chemistry.

difficulties on deconvolving the individual interaction parameters. Analogous problems are encountered in spectra obtained under MAS, therefore, pulse sequences for separation of interactions are required.

Previously, Spaniol et al. [103] suggested two sequences for the separation of the shift and first-order quadrupolar interactions under MAS, the so-called two-pulse and three-pulse sequence. The two-pulse sequence is, in principle, a spin-echo sequence, and exhibits excellent sensitivity (retains all of the available signal components), however, the sequence has a poor excitation bandwidth and the spectrum consists of sidebands with phase-twist lineshape. [104] The three-pulse sequences displays broadband excitation and gives rise to pure absorption-mode lineshapes for the sideband manifold in the spectrum. The improvement comes with a tradeoff of reduced sensitivity by a factor of 3. However, for both sequences the main objective of separating the shift and first-order quadrupolar interactions is achieved only partially, therefore, limiting the practical use of the sequences for studying spin $I = 1$ nuclei. More recently, a spin-echo sequence with off-MAS was employed to separate and correlate the time-independent parts of the rank-2 anisotropies. [105] The experiment requires precise calibration of the “off-angle” value, which proves to be difficult for conventional MAS probes. In addition, the resolution is lowered compared to standard MAS experiments, which could impede the study of systems with multiple resonances.

In Paper II we report that the phase-adjusted spinning sideband (PASS) experiment can be employed for separating and correlating the anisotropic parts of the shift and first-order quadrupolar interactions under MAS. Our findings are summarised in Sections 4.1 and 4.2.

4.1 Theoretical description of the PASS sequence

Originally the phase-adjusted spinning sideband experiment was introduced by Dixon [106; 107] and was intended for separating the isotropic and anisotropic parts of the shift tensor. Excluding the excitation pulse, the sequence is composed of four π pulses the positions of which are modified with each increment so that the isotropic shift is refocussed, while the shift anisotropy progressively evolves. However, the time period containing the π pulses is not constant, which induces an additional modulation due to the transverse relaxation and hinders complete separation of the isotropic and anisotropic parts.

More recently, Antzutkin and coworkers [108] reported a constant time experiment with five π pulses (see Fig.4.2), which solves this complication. The constant delay T, which begins immediately after the excitation pulse and ends at the start of the acquisition, is fixed to an integer multiple of rotor periods $N\tau_r$, where $N = 1+6n$ and n is a non negative integer. Setting the start of the acquisition at time point $t = 0$, the position of the qth pulse is defined at time $-T + \tau_q$. We proceed by demonstrating analytically that the sequence can also separate the shift anisotropy from first-order quadrupolar interaction. Considering a spin $I = 1$ nucleus subject to the shift interaction, the integrated phase due to the evolution in the PASS sequence is given by:

$$\begin{aligned}\Phi_{\mathrm{S}}(t_2;\gamma_{\mathrm{SR}}) = \Omega_{\mathrm{iso}}(\tau_{\mathrm{seq}}-t_2)+2\sum_{q=1}^{5}(-1)^{q+1}\xi_{\mathrm{c}}(-T+\tau_q;\gamma_{\mathrm{SR}})\\ -\xi_c(-T;\gamma_{\mathrm{SR}})-\xi_c(t_2,\gamma_{\mathrm{SR}}),\end{aligned} \tag{4.1}$$

where $\xi_c(t;\gamma_{\mathrm{SR}})$ is a phase function given by:

$$\xi_c(t;\gamma_{\mathrm{SR}}) = \sum_{z=-2,z\neq 0}^{+2} \frac{\omega_c^{(z)}(\gamma_{\mathrm{SR}})}{-iz\omega_r}\exp(-iz\omega_r t). \tag{4.2}$$

Furthermore, τ_{seq} in Eq.4.1 is:

$$\tau_{\mathrm{seq}} = -T+2\sum_{q=1}^{n}(-1)^{q+1}\tau_q. \tag{4.3}$$

In the PASS experiment we map the evolution of the shift anisotropy in the indirect dimension. The extent of evolution is quantified by introducing a "pseudo-t_1" variable denoted as the pitch Θ. If N_{inc} increments are used in the experiment, then the pitch for the ith increment ($i = 1,2,\ldots,N_{\mathrm{inc}}$) is $\Theta = 2N\pi(i-1)/N_{\mathrm{inc}}$. The progressive evolution of the shift anisotropy and concurrent refocussing of the isotropic shift with increasing pitch is controlled by the pulse positions τ_q according to:

$$2\sum_{q=1}^{5}(-1)^{q+1}\xi_{\mathrm{c}}(-T+\tau_q;\gamma_{\mathrm{SR}})-\xi_c(-T;\gamma_{\mathrm{SR}}) = \xi_c(\Theta/\omega_r;\gamma_{\mathrm{SR}}) \tag{4.4}$$

$$\tau_{\mathrm{seq}} = 0 \tag{4.5}$$

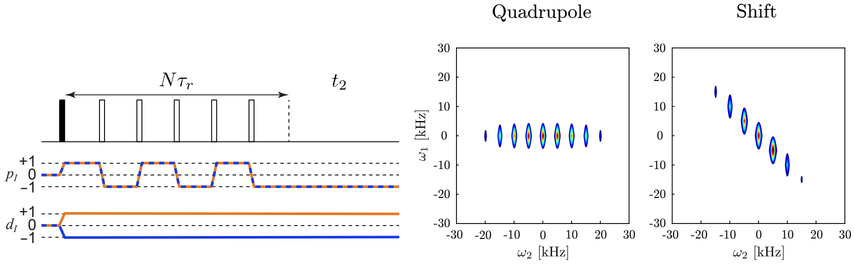

Figure 4.2: PASS pulse sequence. On the left we have the PASS pulse sequence with the symmetry pathways. On the right simulated PASS spectra are shown for a spin $I = 1$ nucleus subject to either the first-order quadrupolar interaction or the shift anisotropy. Reproduced from [109], with permission of AIP Publishing.

In practice these equations are solved numerically to give pulse position times τ_q for each increment i and have been tabulated previously. [108] Based on Eq.4.4 and 4.5 we can derive the time domain powder averaged signal of the PASS sequence, which is given by a Fourier series:

$$S(\Theta;t_2) = \sum_{m=\infty}^{+\infty} \bar{I}_m \exp[i(\Omega_{\text{iso}} + m\omega_r)t_2] \exp[-im\Theta]. \tag{4.6}$$

$\bar{I}_m$ corresponds to the sideband intensity expressed as:

$$\bar{I}_m = \frac{1}{4\pi} \int_0^{2\pi} d\alpha_{\text{SR}} \int_0^{\pi} \left[C_q^{(m)}\right]^2 \sin(\beta_{\text{SR}}) d\beta_{\text{SR}}. \tag{4.7}$$

Inspection of Eq.4.6 reveals that the “pseudo-t_1” dimension is modulated only by the shift anisotropy, while both parts of the shift interaction evolve in the direct dimension. According to Eq.4.6 the correlation between the two dimensions leads to generation of sidebands along the antidiagonal $\omega_2 = -\omega_1$ (see Fig.4.2). In order to ensure pure absorption-mode lineshapes the number of increments N_{inc} is chosen as 2^k with $k = 1,2,3....$ This constraint arises as a result of the Fourier transform of the indirect dimension yielding a Dirac delta function $\delta(\omega_1 - m\omega_r)$.

We now turn to discussing the PASS spectrum of a single spin $I = 1$ nucleus subject to the first-order quadrupolar interaction. From the satellite order d diagram in Fig.4.2 we notice that the d-order remains unaffected throughout the sequence and under static conditions this would indicate that evolution occurs during this time period. However, MAS provides a periodic modulation of the spatial part of the interaction and refocusses the interaction every rotor period if the spin part is not perturbed. Since the constant time period T is a multiple of a rotor period, at beginning of the acquisition at $t = 0$ the first-order quadrupolar interaction is refocussed. Thus, we write the expression of the accrued phase for each transition as:

$$\pm\Phi_{\text{Q}}(0;\gamma_{\text{QR}}) = \pm\xi_{\text{q}}\left(t_2 + \frac{\gamma_{\text{QR}}}{\omega_r};0\right) \mp \xi_q\left(\frac{\gamma_{\text{QR}}}{\omega_r};0\right). \tag{4.8}$$

Table 4.1: Best fit tensor parameters obtained from the 2D quadruple shifting d-echo (static) and PASS (MAS) spectra of $CuCl_2{\cdot}D_2O$.

Method	δ_{iso} (ppm)	$\Delta\delta$ (ppm)	η_S	C_Q (kHz)	η_Q
Static	78 ± 2	-153 ± 3	0.87 ± 0.03	118.3 ± 0.6	0.86 ± 0.01
MAS	76.8 ± 0.2	-179 ± 5	0.77 ± 0.03	120.0 ± 1.8	0.84 ± 0.03

Sample	α (°)	β (°)	γ (°)
Static	94.5 ± 0.3	89.8 ± 0.9	3.5 ± 0.3
MAS	108 ± 6	117 ± 3	2 ± 4

Again we can derive the powder averaged time domain signal:

$$S(t_2) = \sum_{n=-\infty}^{+\infty} \left(\bar{I}_n + \bar{I}_{-n}\right) \exp[in\omega_r t_2], \tag{4.9}$$

where the amplitude $\bar{I}_n$ is the sideband intensity due to one of the spin transitions:

$$\bar{I}_n = \frac{1}{4\pi} \int_0^{2\pi} d\alpha_{\text{QR}} \int_0^{\pi} \frac{1}{2} \left[C_q^{(n)}\right]^2 \sin(\beta_{\text{QR}}) d\beta_{\text{QR}}. \tag{4.10}$$

In the spectrum the spinning sideband manifolds of each transition are superimposed, and so the sideband intensity is a sum of the amplitudes $\left(\bar{I}_n + \bar{I}_{-n}\right)$. As predicted the first-order quadrupolar interaction does not evolve during the "pseudo-t_1" dimension and the sidebands are observed at zero frequency (see Fig.4.2).

We have established that the shift anisotropy evolves during the "pseudo-t_1" period, while the projection on the direct dimension will comprise contributions from both interactions. Elimination of the shift anisotropy from the direct dimension is achieved by performing a shearing transformation parallel to the "pseudo–t_1" dimension with a shear ratio of $\kappa = -1$, in analogy to the static experiments described in Chapter 3. The projection onto one axis shows the shift anisotropy, while the second gives first-quadrupolar interaction together with the isotropic shift. Therefore, we denote these dimensions as shift anisotropy and isotropic shift/quadrupole dimensions. Furthermore, the sideband intensities of the 2D spinning sideband manifold provide information about the relative orientation between the two tensors. However, we note that a major disadvantage of the sequence is the poor excitation bandwidth due to the use of five π pulses.

4.2 Experimental performance of the PASS sequence

We continue by evaluating the performance of the sequence experimentally and compare the results with the static methods. In Paper II we have examined two paramagnetic systems $Ni(CD_3COO)_2 \cdot 4H_2O$ and $CuCl_2 \cdot 2D_2O$ and two different samples of an anion conductor oxhydride $BaTiO_{3-x}D_y$. However, here we will only focus on the most challenging

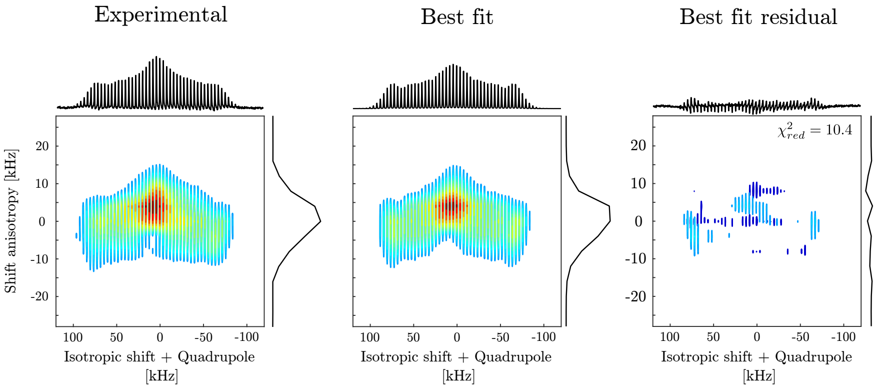

Figure 4.3: Experimental and simulated ^{2}H PASS spectra of $CuCl_2 \cdot 2D_2O$. From left to right are given experimental, best fit, and best fit residual ^{2}H PASS spectra of $CuCl_2 \cdot 2D_2O$. Both experimental and simulated spectra have been sheared. The projection of the isotropic shift/quadrupole dimension shows the spinning-sideband manifold, while the projection of the shift anisotropy dimension shows the profile of the spinning sideband intensities. Spectra were acquired/simulated at 4 kHz MAS. Reproduced from [109], with permission of AIP Publishing.

case $CuCl_2 \cdot 2D_2O$, which exhibits the largest anisotropic interactions for ^{2}H among the studied samples. The sheared and Fourier transformed spectrum of $CuCl_2 \cdot 2D_2O$ is given in Fig.4.3. Inspection of the spectrum reveals considerable phase distortions in the isotropic shift/quadrupole dimension, which arise due to the poor excitation bandwidth of π pulses. In order to quantify the impact of the finite pulse effects and pulse imperfections on the 2D lineshape we proceed by extracting the NMR parameters of the individual interactions and the Euler relating the two tensors.

In an effort to obtain the isotropic shift and EFG tensor components we fit the isotropic shift/quadrupole dimension. Subsequently, the 2D lineshape was fit to procure the shift anisotropy and assymetry together with the Euler angles defining the orientation between the two tensors. The best fit values from the PASS and static quadruple adiabatic shifting d-echo experiment are collected in Table 4.1. While the isotropic shift and the quadrupolar parameters are in agreement between the static and MAS experiments, the shift anisotropy and asymmetry exhibit considerable differences and do not match within the margin of error (Table 4.1). The discrepancy is most likely a result of the poor excitation bandwidth of the π pulses, which generate unwanted satellite order d pathways. As discussed in Chapter 3 phase cycling cannot eliminate these undesirable pathways, since the d-order is selected indirectly. The artefact pathways lead to incomplete refocussing of the evolution due to the first-order quadrupolar interaction during the "pseudo-t_1" evolution period. This evolution of the first-order quadrupolar interaction provides an additional source of broadening to the shift anisotropy dimension, thus increasing the extracted shift anisotropy value and influencing the accuracy of the asymmetry parameter. Similarly, the α and β Euler angles relating the orientation between the two tensors show significant differences ($15 - 30^\circ$) between the static and MAS experiments. Again we can rationalize this systematic error on the basis of the low excitation bandwidth.

Nevertheless, we conclude that accurate tensor components can be procured, in particular of the quadrupolar parameters and isotropic shift, employing the PASS sequence. In addition, due to MAS the sensitivity is significantly increased, hence shortening the experimental time. Furthermore, the sequence opens the avenue to study more complex samples containing multiple local hydrogen environments.

5

Excitation of large anisotropic interactions by low-power irradiation

The discussed solid-state NMR techniques have hitherto focussed on experiments that perform well on systems with anisotropic interactions smaller or similar in magnitude to the available RF field amplitude. In many cases the nuclear hyperfine interaction and first-order quadrupolar interaction spread the resonances over several MHz, which renders the excitation and manipulation of the signal by conventional pulses and even adiabatic pulses ineffective. Furthermore, due to the very broad resonance a reduction in both sensitivity and resolution is observed for these systems. In the context of spin $I = 1$ nuclei this is one of the main challenges for widespread investigation of the ^{14}N, the most prevalent isotope of nitrogen with a natural abundance of 99.6%. Several approaches have been proposed for broadband excitation of these resonances. [110–113]

In static solids adiabatic pulses have been employed to achieve excitation windows up to 1 MHz, still acquisition of several subspectra at different transmitter offset frequencies are necessary to obtain the complete lineshape. This leads to long experimental times, which can be improved by using the Carr-Purcell-Meiboom-Gill acquisition that refocusses the magnetization dephasing due to the anisotropic interactions during the FID and increases the sensitivity of the experiment. [110; 111] As explained in Chapter 4 MAS experiments have the advantage over static methods in terms of sensitivity and resolution. Under MAS broadband excitation can be obtained by using the delays alternating with nutation for tailored excitation pulse scheme, [112; 113] which splits the excitation pulse into shorter pulses separated by a rotor period. As a result the excitation bandwidth is divided into a comb with the tines located at the positions of the sidebands. However, the bandwidth of the isotropic resonances is limited, since the breadth of each tine is a few kHz.

Typically higher resolution is achieved by probing the ^{14}N resonances indirectly via a spin $I = 1/2$ nucleus. Originally, this was addressed in 1D experiments using the transfer of populations in double resonance (TRAPDOR) method. [114; 115] More recently, 2D methods have been introduced separately by Gan et al. [116–118] and Bodenhausen et al. [119–122] for correlating single-quantum (SQ) ^{14}N coherences with spin $I = 1/2$ nuclei. The advantage of these methods is two-fold. First, the resolution is significantly increased due to the larger spectral dispersion of 2D experiments and the narrower linewidth of spin $I = 1/2$ nuclei. Second, the sensitivity is enchanced due to the higher gyromagnetic ratio of ^{1}H or ^{13}C. Most of the methods can be categorized as heteronuclear multiple-quantum correlation (HMQC) methods, but the experiments differ in the ^{1}H to ^{14}N polarization transfer approach. Many different strategies for the polarization transfer have been employed, for instance, transfer via the J-coupling and residual dipolar splitting, [116; 119–121] rotary resonance, [117; 122] symmetry-based recoupling, [123; 124] TRAPDOR [125; 126] or cross-polarization. [127] However, these experiments limit the spectral window in the ^{14}N dimension in order to refocus the first-order quadrupolar interaction. Although recently a TRAPDOR-HMQC experiment was proposed for removing this restriction. [128]

Alternatively, this can be solved by exciting double-quantum (DQ) ^{14}N resonances. Since the transition is symmetric for spin $I = 1$ nuclei it is not affected by the first-order quadrupolar interaction, which potentially allows to choose the spectral window freely. Furthermore, the sideband linewidth is less sensitive to the magic-angle misset. The excited DQ coherences can be detected directly via ^{14}N overtone spectroscopy. [129–131] However, the low excitation efficiency and poor bandwidth has hindered routine application of the method. On the other hand, the DQ spectrum can be obtained by indirect detection via the single-quantum coherence of ^{14}N [66; 132] or a spin $I = 1/2$ nucleus. [119–122; 133]. However, the available DQ excitation sequences exhibit low and nonuniform excitation efficiency, meaning that crystallites with different orientations are not excited equally.

In Paper III we address the issue of excitation of large anisotropic interactions under MAS using phase-modulated pulse sequences with low-power pulses. We begin by providing a general theoretical framework applicable to any spin system subject to interactions among which the Hamiltonians commute. We exemplify the utility of the framework by describing DQ excitation of spin $I = 1$ nuclei in the low-power regime. In Section 5.1 we provide an overview of the new theoretical formalism for analysing low-power excitation of large anisotropic interactions. Followed by an application of the theoretical framework to DQ excitation of spin $I = 1$ nuclei in Section 5.2.

5.1 Theoretical description of low-power irradiation of spins subject to large anisotropic interactions

5.1.1 The jolting frame description

In Paper III we provide a theoretical description of phase-modulated rotor-synchronised pulse sequences in the low-power regime. In the current context pulses with RF amplitude smaller than the spinning frequency ($|\omega_1| < |\omega_r|$) are defined as low-power pulses. Moreover, we consider anisotropic interactions as large if the magnitude of the interaction is exceedingly larger than the spinning frequency ($|\Omega^{(\Lambda)}| \gg |\omega_r|$). The phase-modulated rotor-synchronised pulse sequences are often called as symmetry-based sequences [134; 135] and, in general, are composed of N pulse elements $q = 0, 1, 2, ..., N-1$ in n rotor periods such that the qth pulse element with phase ϕ_q begins at time $t_q^{(0)} = q\tau_p$. τ_p is the length of each pulse element. The Hamiltonian of the qth pulse is expressed as:

$$\hat{H}_1(t_q) = \hat{R}_z(\phi_q)\hat{H}_1(t_0)\hat{R}_z(\phi_q)^{-1}, \tag{5.1}$$

where t_q is the time point within the qth pulse ($t_q^{(0)} \leq t_q < t_{q+1}^{(0)}$). $\hat{H}_1(t_0)$ is the RF field Hamiltonian of the zeroth ($q = 0$) pulse element. Assuming that $\phi_0 = 0$, the Hamiltonian is given by $\hat{H}_1(t_0) = \omega_1 \hat{I}_x$. Furthermore, following the approach of Levitt et al. [134; 135] for symmetry-based methods the phase of the qth pulse is expressed as:

$$\phi_q = 2\nu\pi q/N, \tag{5.2}$$

where ν is the spin winding number. We notice that each pulse element considered here will produce a rotation about an axis located in the transverse (xy-) plane, thus we designate these sequences as $\mathrm{X}N_n^{\nu}$.

We note that the total Hamiltonian $\hat{H}(t)$, which includes the internal spin interactions given in Eq.2.33 and RF field Hamiltonian in Eq.5.1, exhibits two sources of time dependency due to RF pulses and periodic modulation of spatial part of the interaction by MAS. In general, the Hamiltonian does not self-commute at different times, i.e. $[\hat{H}(t_1), \hat{H}(t_2)] \neq 0$, and so the spin dynamics are analyzed by finding approximate solutions, for instance, by employing average Hamiltonian theory (AHT). [33; 46] To ensure that the expansion of the average Hamiltonian converges quickly we transform into the interaction frame of the largest interaction. In the present case, we are examining low-power irradiation of nuclei subject to large anisotropic interactions, therefore we transform into the interaction frame of the large anisotropic spin interaction(s), or the so called jolting frame. [112] Formally we can express the transformation of the Hamiltonian during the qth pulse element into the jolting frame as:

$$\tilde{H}(t_q) = \hat{U}_0^{(\mathrm{large})}(t_q, 0)^{-1}\hat{H}_1(t_q)\hat{U}_0^{(\mathrm{large})}(t_q, 0) + \sum_{\Lambda,\mathrm{small}} \sum_{l,\lambda} \Omega_{l0,\lambda0}^{(\Lambda)}(t_q)\hat{T}_{\lambda0}^{(\Lambda)}. \tag{5.3}$$

The transformation occurs into the interaction frame of the periodic part of the large anisotropic interaction(s). The sum in Eq.5.3 refers to any remaining internal spin interaction terms, such as isotropic and small anisotropic interactions.

It is convenient to examine the features of the jolting frame Hamiltonian by expressing it as a Fourier series as given below:

$$\tilde{H}(t_q) = \sum_{\mu=-\infty}^{+\infty} \sum_{p=0,\pm} \hat{h}_{\mu,p}(t_0) \exp(i\mu\omega_r t_0) \times \exp\left[i\frac{2\pi q}{N}(\mu n - \nu p)\right]. \tag{5.4}$$

The coefficients $\hat{h}_{\mu,p}(t_0)$ are expressed as:

$$\begin{aligned}\hat{h}_{\mu,p}(t_0) = \omega_1 \sum_{M=-I}^{+I} \frac{1}{2}\sqrt{I(I+1)-M(M+1)} \\ \times \left(A^{(p\mu)}_{c,M+1,M} \exp\left(pi\phi^{(p\mu)}_{c,M+1,M}(\gamma_{\mathrm{PR}})\right) \hat{I}_p^{(M+1,M)}\right),\end{aligned} \tag{5.5}$$

for coherences $p \neq 0$, while for coherence $p = 0$ the coefficient is given by:

$$\hat{h}_{\mu,0}(t_0) = \sum_{\Lambda,l,\lambda} \Delta_{\mu,m}\, \omega_{c,l0,\lambda 0,-\mu}(\gamma_{\mathrm{PR}}) \hat{t}^{(\Lambda)}_{\lambda,0}. \tag{5.6}$$

The Hamiltonian ($\tilde{H}(t_q)$) in Eq.5.4 describes the exact spin dynamics in the jolting frame. We see that each jolting frame Hamiltonian term exhibits a spatial dependence via the sideband-order μ of the spinning sideband manifold and a spin dependence due to the order p of the corresponding operator in the RF field Hamiltonian. This reflects the two-fold time dependence of the Hamiltonian due to the sample rotation and the pulse sequence. In the Section 5.1.2 we approximate the Hamiltonian using AHT to obtain a qualitative depiction of the spin physics.

5.1.2 Selection rules

In symmetry-based sequences the spatial part of the interaction is modulated by the sample spinning, whilst the spin part is affected by the pulse sequence. The relation between the two time dependencies can be utilized to retain or suppress certain components of the Hamiltonian. This property has been exploited to decouple or recouple certain spin interactions. Qualitatively the selection of the symmetry-allowed Hamiltonian terms is determined by selection rules. [134; 135] Therefore, here we discuss the selection rules of the low-power symmetry-based methods, which are obtained by approximating the jolting frame Hamiltonian by AHT.

Eq.5.4 is used to derive the first-order average Hamiltonian given below:

$$\overline{H}^{(1)} = \sum_{\mu=-\infty}^{+\infty} \sum_{p=0,\pm} \overline{H}^{(1)}_{\mu,p}, \tag{5.7}$$

where the components of the first-order average Hamiltonian are expressed as:

$$\begin{aligned}\overline{H}^{(1)}_{\mu,p} &= \frac{1}{\tau_p}\int_0^{\tau_p} dt_0 \sum_{\mu=-\infty}^{+\infty}\sum_{p=0,\pm} \hat{h}_{\mu,p}(t_0)\exp(i\mu\omega_r t_0)\\ &\times \frac{1}{N}\sum_{q=0}^{N-1}\exp\left[i\frac{2\pi q}{N}(\mu n-\nu p)\right]\end{aligned} \tag{5.8}$$

As expected the first-order average Hamiltonian consists of a sum of different components, which have a spatial dependence via the sideband-order μ, and a spin dependence due to the order p of the corresponding operator in the RF field Hamiltonian. Evaluating the sum in the second line of Eq.5.8 over the pulse elements q, gives the following selection rule for the first-order average Hamiltonian:

$$\overline{H}^{(1)}_{\mu,p} = 0 \quad \text{if} \quad \mu n-\nu p \neq NZ, \tag{5.9}$$

where Z is any integer. The selection rule indicates that specific terms of the average Hamiltonian can be removed by choosing a sequence with XN_n^N to satisfy $\mu n-\nu p\neq NZ$. Following a similar procedure selection rules can be derived for higher-order average Hamiltonians. For the second-order average Hamiltonian the selections rules are summarised as:

$$\overline{H}^{(2)}_{\mu_1\mu_2,p_1p_2} = 0 \quad \text{if} \quad \begin{cases}\mu_1 n-\nu p_1\neq NZ_1\\ \text{AND}\\ \mu_2 n-\nu p_2\neq NZ_2\\ \text{AND}\\ (\mu_1+\mu_2)n-\nu(p_1+p_2)\neq NZ_3,\end{cases} \tag{5.10}$$

where $\overline{H}^{(2)}_{\mu_1\mu_2,p_1p_2}$ are the second-order average Hamiltonian components and Z_1, Z_2 and Z_3 are integers. The derived selection rules are identical to the symmetry-based C sequences of Levitt et al. [134; 135]. Furthermore, in analogy to the conventional symmetry-based sequences the selection rules depend on the winding number ν, number of rotor periods n and the number of pulses N. However, here the sideband order μ of the manifold and the coherence order p encodes the spatial and spin dependence in the jolting frame Hamiltonian, respectively, while in the formalism developed by Levitt et al. [134; 135] the spin and space order encode the spin and spatial parts in the Hamiltonian. The selection rules provide a qualitative assessment of which components are symmetry forbidden. However, the approach does not give any quantitative insights on the non-zero terms, which in certain cases can be zero due to "hidden" symmetry. In order to gain information about the magnitude of the non-zero components numerical simulations or explicit calculations are necessary.

The discussion of the theoretical formalism has been hitherto general and can be employed to characterize the spin dynamics of any spin I provided the low-power regime is satisfied. In Section 5.2 we demonstrate the applicability of the theoretical approach by investigating double-quantum (DQ) excitation for spin $I=1$ nuclei.

5.2 Application to DQ excitation in spin $I = 1$ nuclei

5.2.1 Theoretical description of double-quantum excitation in spin $I = 1$ nuclei

In order to analyse the DQ excitation of spin $I = 1$ nuclei we consider a simplified spin system, which consists of an isolated spin $I = 1$ nucleus subject to the isotropic shift and first-order quadrupolar interactions. We find the approximation to be justified for the systems studied here, since the first-order quadrupolar interaction is expected to be at least an order of magnitude larger than the shift anisotropy or the second-order quadrupolar interaction. Transforming the total Hamiltonian $\hat{H}(t)$ into the interaction frame of the first-order quadrupolar interaction, yields a jolting frame Hamiltonian with the following coefficients:

$$\begin{aligned}\hat{h}_{\mu,\pm1}(t_0) = {} & \frac{\sqrt{2}}{2}\omega_1 A^{(\pm\mu)}_{c,0,-1}\exp\left(\pm i\phi^{(\pm\mu)}_{c,0,-1}(\gamma_{\mathrm{QR}})\right)\hat{I}^{(0,-1)}_{\pm} \\ & +\frac{\sqrt{2}}{2}\omega_1 A^{(\pm\mu)}_{c,+1,0}\exp\left(\pm i\phi^{(\pm\mu)}_{c,+1,0}(\gamma_{\mathrm{QR}})\right)\hat{I}^{(+1,0)}_{\pm}\end{aligned} \tag{5.11}$$

for $p \neq 0$ and

$$\hat{h}_{\mu,0}(t_0) = \Delta_{\mu,0}\Omega_0\hat{I}_z \tag{5.12}$$

when $p = 0$. We note that the spinning sideband manifold due to the first-order quadrupolar interaction is symmetric with respect to the centreband and so the sidebands of the two transitions are related by a reversal about the centreband. The sideband amplitude and phase can be redefined as:

$$A^{(\mu)}_{c,+1,0} = B^{(\mu)}_q, \quad \phi^{(\mu)}_{c,+1,0}(\gamma_{\mathrm{QR}}) = \xi^{(\mu)}_q(\gamma_{\mathrm{QR}}) \tag{5.13}$$

$$A^{(\mu)}_{c,0,-1} = B^{(-\mu)}_q, \quad \phi^{(\mu)}_{c,0,-1}(\gamma_{\mathrm{QR}}) = -\xi^{(-\mu)}_q(\gamma_{\mathrm{QR}}) \tag{5.14}$$

This symmetry property of the first-order quadrupolar interaction will greatly simplify the form of the average Hamiltonians of the DQ excitation sequences.

Excitation of DQ coherences from magnetization at thermal equilibrium ($\hat{I}_z = 2\hat{I}^{(+1,-1)}_z$) occurs if the RF field term contains DQ spin operators ($\hat{I}^{(+1,-1)}_{\pm}$) as summarised by the transformation below:

$$\exp\left(-i\phi\hat{I}^{(+1,-1)}_x\right)\hat{I}^{(+1,-1)}_z\exp\left(+i\phi\hat{I}^{(+1,-1)}_x\right) = \cos(\phi)\hat{I}^{(+1,-1)}_z - \sin(\phi)\hat{I}^{(+1,-1)}_y. \tag{5.15}$$

Spin operators with order $p = \pm2$ emerge in the Hamiltonian only with the second-order average Hamiltonian, therefore, the Hamiltonian must be evaluated at least to the second-order.

DQ excitation with a single-sideband-selective pulse. First we consider the simplest DQ excitation scheme in the low-power regime a single-sideband-selective pulse. To facilitate the discussion we henceforth refer to it as a single pulse and label it as $\mathrm{X}1^0_1$ in accordance with the notation introduced in Section 5.1. We begin by deriving the first-order average Hamiltonian.

Based upon the sequence parameters $n = 1, N = 1$ and $\nu = 0$ and the selection rules we notice that Hamiltonian components are symmetry allowed for all sideband-orders μ. In contrast, the integral in Eq.5.8 is non-zero only for $\mu = 0$, which demonstrates an instance of "hidden" symmetry within each pulse sequence element that is not predicted by the selection rules. Hence the first-order average Hamiltonian is given by:

$$\begin{aligned}\overline{H}^{(1)}_{\mathrm{QX1}_1^0} = \sqrt{2}\omega_1 B_q^{(0)} \Big(&\hat{R}_z^{(+1,0)}(\gamma_{\mathrm{QR}})\hat{I}_x^{(+1,0)}\hat{R}_z^{(+1,0)}(\gamma_{\mathrm{QR}})^{-1} \\ &+ \hat{R}_z^{(0,-1)}(\gamma_{\mathrm{QR}})\hat{I}_x^{(0,-1)}\hat{R}_z^{(0,-1)}(\gamma_{\mathrm{QR}})^{-1}\Big) + \Omega_0\hat{I}_z. \qquad (5.16)\end{aligned}$$

The Hamiltonian can be interpreted as the application of a RF field to each of the two SQ transitions. Additionally we have a term due to the evolution of the isotropic shift. Clearly, DQ coherences are not excited by this Hamiltonian.

We continue by evaluating the second-order average Hamiltonian. The selection rules reveal that the Hamiltonian components are non-zero for all pairs of (μ_1, μ_2). As before, the second-order average Hamiltonian contains terms with "hidden" symmetry, hence sideband-order pairs of (0,0),$(-\mu,\mu)$, and $(0,\mu)$ are non-zero. The explicit derivation of the "hidden" symmetry allowed components and second-order average Hamiltonian is mathematically more involved and is provided in Paper III. The obtained second-order average Hamiltonian is given by:

$$\overline{H}^{(2)}_{\mathrm{QX1}_1^0} = \frac{\omega_1^2}{2\omega_r} d_\Sigma \left(\hat{I}_x^{(+1,-1)} + \hat{I}_z^{(+1,0)} - \hat{I}_z^{(0,-1)}\right), \qquad (5.17)$$

where d_Σ is a dimensionless quantity the value of which is determined by the sideband amplitude and phase as shown below:

$$\begin{aligned}d_\Sigma = \sum_{\mu\neq 0} \frac{1}{\mu} \Bigg[&\left(B_q^{(\mu)}\right)^2 - \left(B_q^{(-\mu)}\right)^2 - 2B_q^{(0)}B_q^{(\mu)}\cos\left(\xi_q^{(\mu)}(\gamma_{\mathrm{QR}}) - \xi_q^{(0)}(\gamma_{\mathrm{QR}})\right) \\ &+ 2B_q^{(0)}B_q^{(-\mu)}\cos\left(\xi_q^{(-\mu)}(\gamma_{\mathrm{QR}}) - \xi_q^{(0)}(\gamma_{\mathrm{QR}})\right)\Bigg] \qquad (5.18)\end{aligned}$$

The Hamiltonian comprises a rank-2 longitudinal spin operator $\hat{I}_z^{(+1,0)} - \hat{I}_z^{(0,-1)}$ and a DQ spin operator. The $\hat{I}_z^{(+1,0)} - \hat{I}_z^{(0,-1)}$ operator commutes with $\hat{I}_z$, thus does not influence the equilibrium magnetization, while the DQ spin operator will excite DQ magnetization. Analysis of the Hamiltonian also provides insights about the disadvantages of this sequence. The excitation scheme apart from DQ coherences also generates SQ coherences, which can potentially reduce the excitation efficiency of DQ magnetization, in particular for long irradiation times. Furthermore, the second-order average Hamiltonian depends on the Euler angle γ_{QR} through the sideband phase in the expression d_Σ. This means that the DQ excitation scheme is not γ-encoded and will lead to the appearance of "artefact" spinning sidebands in the DQ dimension, unless rotor-synchronization is employed, which reduces the spectral window.

DQ excitation with x-inverse-x sequence. Initially, the x-inverse-x scheme was developed for heteronuclear decoupling, [136] but since has been applied to DQ excitation of spin $I = 1$

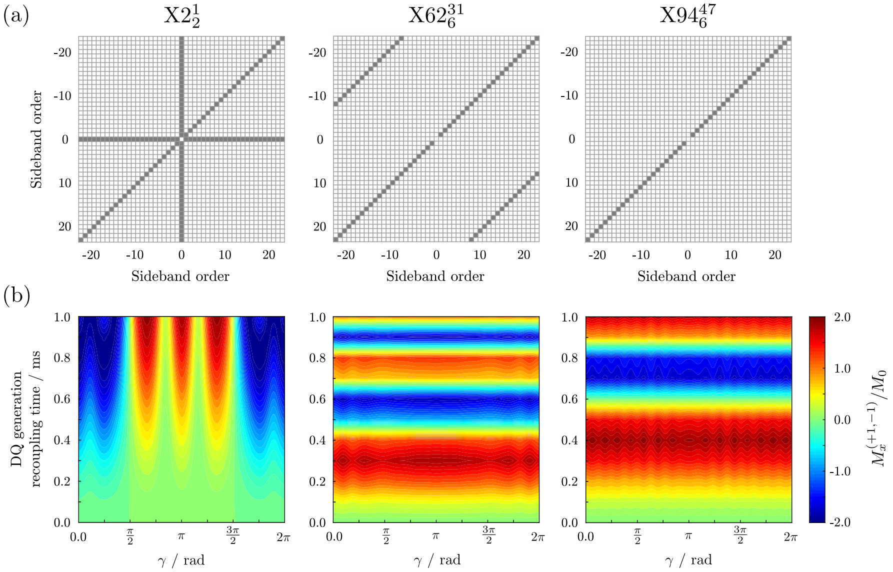

Figure 5.1: γ-encoding properties of different XN_n^ν pulse sequences. (a) shows a schematic representation of the sideband pairs contributing to the second-order average Hamiltonian for X2$_2^1$, X62$_6^{31}$ and X94$_6^{47}$ sequence. The filled and empty squares represent non-zero and zero terms, respectively. The DQ excitation efficiency as a function of irradiation time and γ_{QR} is given in (b) for a single ^{14}N spin subject to only the first-order quadrupole interaction. Details of simulations can be found in Paper III. Reproduced from [137], with permission of AIP Publishing.

nuclei in an effort to eliminate the excitation of SQ terms up to second-order. In our notation we denote the sequence as X2$_2^1$. According to the selection rules the only non-zero terms in the first-order average Hamiltonian are when $p = 0$ and $\mu = 0$. The first-order average Hamiltonian is given by:

$$\overline{H}^{(1)}_{\mathrm{QX}2_2^1} = \Omega_0 \hat{I}_z \tag{5.19}$$

We notice that the Hamiltonian does not include any RF field terms, hence SQ coherences will not be excited.

Again the derivation of the second-order average Hamiltonian is mathematically more involved and complete treatment is given in Paper III. Here we only quote the result, which is identical to the single pulse case:

$$\overline{H}^{(2)}_{\mathrm{QX}2_2^1} = \frac{\omega_1^2}{2\omega_r} d_\Sigma \left(\hat{I}_x^{(+1,-1)} + \hat{I}_z^{(+1,0)} - \hat{I}_z^{(0,-1)} \right) \tag{5.20}$$

As expected, we see that the Hamiltonian up to the second-order only generates DQ coherences, and so theoretically should give rise to higher DQ excitation efficiencies than a single pulse sequence. Similarly as the X1$_1^0$ sequence, X2$_2^1$ scheme is not γ-encoded, since the DQ spin operator in the second-order average Hamiltonian is proportional to d_Σ, which depends on the Euler angle γ_{QR}. Closer examination of the sum d_Σ reveals that components with sideband pairs $(\mu_1, \mu_2) = (-\mu, 0)$ and $(0, \mu)$ are not γ-encoded, while terms with sideband pairs are independent of γ_{QR}, hence are γ-encoded. We illustrate the sideband contributions to the Hamiltonian schematically in Fig.5.1(a). Furthermore, spin dynamic simulations in Fig.5.1(b) demonstrate the variation of the DQ excitation magnitude as a function of γ_{QR}. Therefore, we suspect that the design of a γ-encoded sequence would be possible by choosing a set of (n, N, ν) so that the second-order average Hamiltonian would only depend on the terms with antidiagonal sideband pairs.

New DQ excitation pulse schemes. Here we are interested in designing a γ-encoded pulse sequence. We begin by considering a general $\mathrm{X}N_n^\nu$ sequence. First a restriction is set on the sequence parameters so that no SQ coherences are excited. From the selection rules in Eq.5.9 Hamiltonian terms with $p = \pm 1$ can be removed if n, N are even, and $\nu = N/2$ is odd. We note that this is but one of many options for eliminating RF field terms in the first-order average Hamiltonian.

For the second-order average Hamiltonian only the third condition of the selection rules in Eq.5.10 is met with the chosen n, N and ν values. Furthermore, only $p_1 + p_2$ values of $+2$, 0, -2 are relevant in the present case (see Paper III for more detail) and the selection rule is reduced to:

$$\mu_1 + \mu_2 = \frac{N}{n} Z. \tag{5.21}$$

We see that the allowed Hamiltonian terms are $\mu_1 + \mu_2 = 0, \pm N/n, \pm 2N/n, \pm 3N/n, \ldots$ Therefore setting N sufficiently larger than n we can remove any terms other than with $\mu_1 + \mu_2 = 0$, which are γ-encoded. Assuming that we only retain Hamiltonian terms with $\mu_1 + \mu_2 = 0$ the second-order average Hamiltonian is given by:

$$\begin{aligned} \overline{H}^{(2)}_{\mathrm{QX}N_n^\nu\mathrm{ad}} = \frac{\omega_1^2}{2n\pi\omega_r} \sum_{\mu \neq 0} \left[\frac{\left(B_q^{(\mu)}\right)^2 - \left(B_q^{(-\mu)}\right)^2}{\mu^2} \right] \\ \times \left[\mu n \pi - N \tan\left(\frac{\mu n \pi}{N}\right) \right] \left[\hat{I}_x^{(+1,-1)} + \hat{I}_z^{(+1,0)} - \hat{I}_z^{(-1,0)} \right] \end{aligned} \tag{5.22}$$

We notice that the Hamiltonian only comprises terms with antidiagonal sideband pairs, thus sequences $\mathrm{X}N_n^\nu$ with N/n greater than the number of sidebands are γ-encoded up to the second-order. In order to verify these analytical results we examine the $\mathrm{X}62_6^{31}$ sequence. Fig.5.1(a) shows that for this sequence a few off-antidiagonal terms will still contribute, however, the sideband intensity products of these pairs will be very small and the resulting Hamiltonian terms almost negligible. We confirm this by simulating the DQ excitation efficiency as a function of the γ_{QR} angle, which displays an approximately constant DQ excitation amplitude profile (Fig.5.1(b)). The slight modulations of the DQ efficiency are explained by the interference from higher-order Hamiltonians. Finally, we give an example of a sequence ($\mathrm{X}94_6^{47}$) for which the off-antidiagonal terms are completely removed (see Fig.5.1). Again small deviations from a constant character of the DQ excitation magnitude are observed, in analogy to the $\mathrm{X}62_6^{31}$ sequence. Nevertheless, we expect both sequences to be γ-encoded.

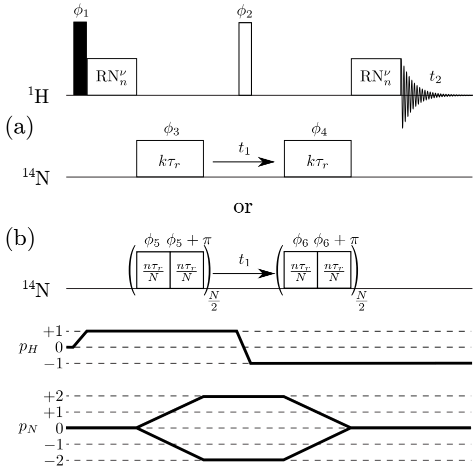

Figure 5.2: Dipolar double-quantum heteronuclear multiple-quantum correlation (D-DQ-HMQC) pulse sequences. D-DQ-HMQC with DQ excitation/reconversion blocks using a single pulse (a) and $\mathrm{X}N_n^\nu$ scheme (b) are provided along with the ^{1}H and ^{14}N coherence pathways. The filled and empty rectangle represent $\pi/2$ and π pulses, respectively. RN_n^ν are the symmetry-based heteronuclear dipolar recoupling sequences. Reproduced from [137], with permission of AIP Publishing.

5.2.2 Experimental evaluation of the DQ excitation pulse sequences

Finally we examine the performance of the DQ excitation schemes experimentally and complement our results with numerical simulations of spin dynamics. As discussed earlier the DQ coherences can be detected directly via overtone spectroscopy or indirectly by correlation with SQ coherences of ^{14}N or another nucleus. The theoretical description in the current form is not valid for overtone spectroscopy and so we opt for the latter strategy. Hence we incorporate the DQ excitation scheme into a HMQC type sequence as shown in Fig.5.2 and to increase experimental sensitivity we choose to correlate ^{14}N DQ signals with ^{1}H.

Briefly, the first pulse in the sequence given in Fig.5.2 acts on the ^{1}H and excites the ^{1}H coherences. The magnetization is transferred to ^{14}N via a symmetry-based hereonuclear dipolar recoupling scheme ($\mathrm{R}N_n^\nu$). Next we excite the DQ coherences of ^{14}N, which is followed by the t_1 evolution period. Afterwards, we have the DQ reconversion and the heteronuclear dipolar reconversion schemes (both identical to the schemes at the beginning of the sequence) that together generate ^{1}H SQ coherences, which are detected. Finally we note that the π pulse on the ^{1}H channel refocusses the evolution of any heteronuclear dipolar and J-coupling evolution. Henceforth, we refer to the sequence as the dipolar double-quantum heteronuclear multiple-quantum correlation (D-DQ-HMQC).

In Paper III we investigate the performance of the DQ sequences on ^{14}N in glycine and N-acetyl-valine, which represent cases with “moderate” and “large” quadrupolar interactions, respectively. However, here we review only the results obtained with glycine. We first exam-

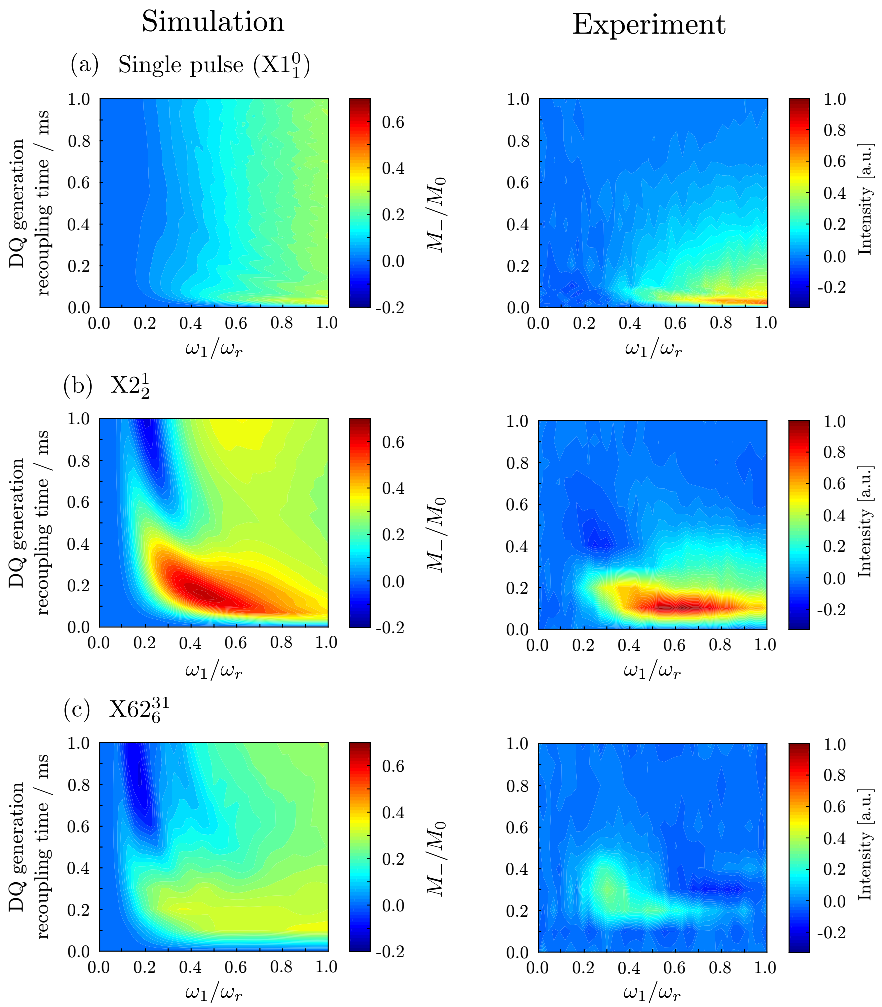

Figure 5.3: Experimental and simulated contour plots for generation of ^{14}N DQ coherence from microcrystalline powder of glycine. From left to right are shown simulated and experimental DQ coherence generation efficiency plots as a function of irradiation time and RF field amplitude using a single pulse (a), $X2_2^1$ (b) and $X62_6^{31}$ (c) for DQ excitation and reconversion. The simulated DQ generation efficiency was obtain from a DQ-filtered experiment by varying the irradiation time and RF field amplitude symmetrically of both the excitation and reconversion blocks. The simulations included the first- and second-order quadrupolar interactions. See Paper III more simulation and experimental details. Reproduced from [137], with permission of AIP Publishing.

ine the DQ excitation/reconversion efficiency. Fig.5.3 shows the simulated and experimental DQ excitation/reconversion efficiency as a function of irradiation time and RF field amplitude for $\mathrm{X}1_1^0$ (a), $\mathrm{X}2_2^1$ (b) and $\mathrm{X}62_6^{31}$ (c) sequences. For short irradiation times (< 0.3 ms) the experimental and simulated plots match very well in the case of $\mathrm{X}1_1^0$ and $\mathrm{X}2_2^1$. We notice that $\mathrm{X}2_2^1$ yields greater DQ excitation efficiency and exhibits good excitation over a larger set of values. The observed differences are in line with our predictions based on the form of the average Hamiltonians of the two sequences. For the single pulse SQ coherences are excited, which leads to lower DQ efficiencies, especially for longer recoupling times. The discrepancy between the experiment and simulation for longer irradiation times (> 0.3 ms) can be explained by ^{14}N coherence relaxation. In the case of $\mathrm{X}62_6^{31}$ both simulated and experimental plots of DQ excitation/reconversion efficiency reveal relatively low excitation efficiency. Moreover, significant differences between experimental and simulated plots are observed. We ascribe these discrepancies mainly to RF pulse imperfections. In particular, to the phase transients, which can form due to the abrupt phase change from 0 to π in the $\mathrm{X}N_n^\nu$ sequence.[138; 139] Subsequent accumulation of the phase errors decreases the DQ excitation efficiency. Similar detrimental effects are expected for the $\mathrm{X}2_2^1$, however, due to the fewer number of pulses the DQ generation is less affected.

While the design of pulse sequences with high DQ excitation efficiency is beneficial for increasing the experimental sensitivity, uniform excitation of all the crystallite orientations is equally desirable. Uniform excitation allows the acquisition of spectra with intact rank-4 second-order quadrupolar lineshapes, hence accurate EFG tensor parameters can be extracted. Therefore, we continue by assessing the DQ excitation efficiency dependence on the crystallite orientation. 2D D-DQ-HMQC experiments of glycine were acquired using three different DQ excitation schemes. Fig.5.4(a) shows the obtained ^{14}N DQ projections for each of the sequences. The isotropic position and the linewidth essential match with the ideal simulated spectrum (see Fig.5.4(b) in red), however, any clear-cut features of the quadrupolar lineshape are absent. The difference between experiment and the simulated lineshapes are potentially caused by the combination of instrumental limitations and an insufficient description of the spin dynamics in the simulations. Associated with the technical limitations we have RF inhomogeneity, phase transients, and MAS frequency instability, that can impact the DQ excitation efficiency and produce distorted quadrupolar lineshapes. From the perspective of simulations, we assume that we have a perfectly crystalline “sample” containing an isolated spin subject to only the first-order and second-order quadrupolar interactions. While in a real sample, the spin is subject also to dipole interactions, relaxation (including anisotropic), in addition, it may lack crystallinity and exhibit structural disorder. All of these effects influence the experimental lineshape, but, in general, it is challenging to establish the prevalent contributions and the exact impact of the factors on the lineshape. Finally, we can also identify inherent factors due to the pulse sequence, for instance, the orientation dependence on the excitation/reconversion of both the heteronuclear dipolar recoupling and DQ scheme.

Here we are interested in understanding the effect of the latter scheme. Fig.5.4(b) (black) shows the simulated second-order quadrupolar lineshape using the DQ schemes $\mathrm{X}1_1^0$, $\mathrm{X}2_2^1$ and $\mathrm{X}62_6^{31}$. In order to characterize the contribution from each orientation we simulated the DQ excitation efficiency as a function of α_{QR} and β_{QR} and results are plotted using a

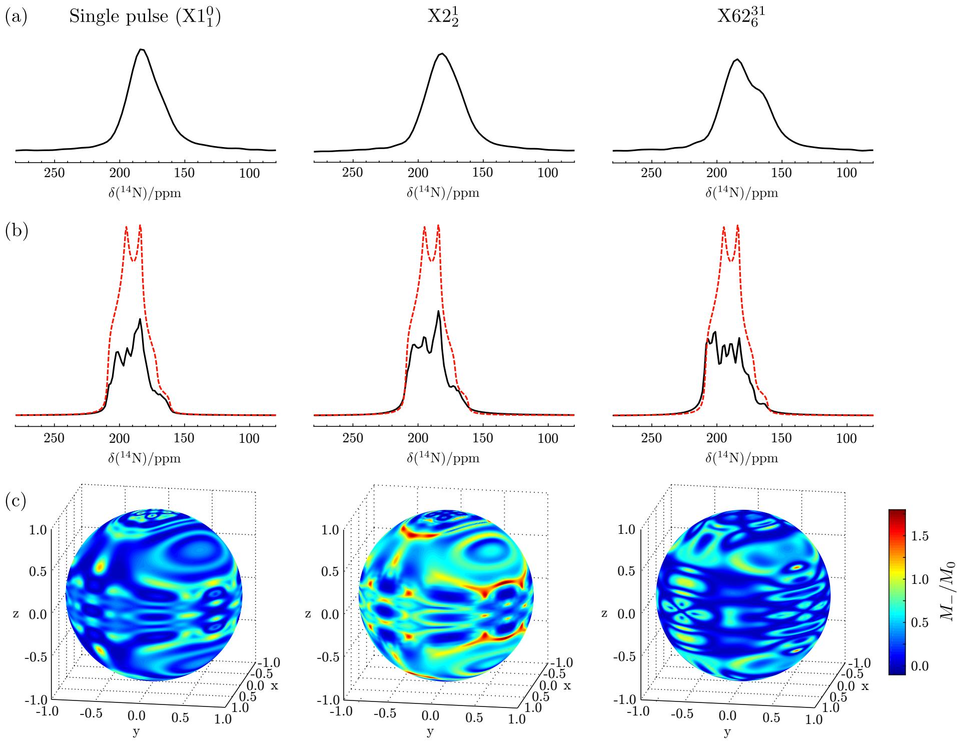

Figure 5.4: Experimental and simulated second-order quadrupolar lineshape from microcrystalline powder of glycine. (a) shows the experimental projections of the indirect dimension of 2D-D-DQ-HMQC spectra using a single pulse, $X2_2^1$ or $X62_6^{31}$ for DQ generation. Full 2D D-DQ-HMQC spectra are available in Paper III. Simulated projections of the indirect dimension of 2D DQ-SQ spectra using single pulse, $X2_2^1$ or $X62_6^{31}$ for DQ generation are provided in (b) in black, while the ideal second-order quadrupole lineshapes are given in red. The simulated DQ-SQ experiments were performed with the same irradiation times and RF powers as the experimental 2D D-DQ-HMQC. The DQ excitation efficiency for each crystal orientation (α, β) is shown in (c) using a spherical coordinate system $(1.0, \alpha, \beta)$. The intensity for each crystallite was acquired from a DQ-filtered experiment, averaging over 48 γ angles was used. Reproduced from [137], with permission of AIP Publishing.

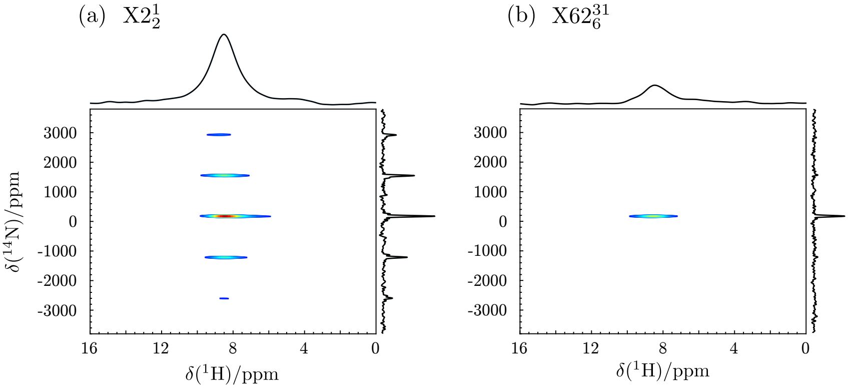

Figure 5.5: 2D D-DQ-HMQC spectra with large spectral window in the indirect dimension of glycine obtained with $X2_2^1$ (a) and $X62_6^{31}$ (b). Reproduced from [137], with permission of AIP Publishing.

spherical coordinate system (1.0, α_{QR},β_{QR}) as shown in Fig.5.4(c). Each point on the sphere displays the expectation value of the DQ magnetization for a single (α_{QR},β_{QR}) pair. The overall pattern of the excitation efficiency is very similar for the single pulse and $X2_2^1$ sequence, however, slightly lower efficiencies are observed across most (α_{QR},β_{QR}) pairs for the single pulse. This is in agreement with our analytical evaluation that revealed that the DQ excitation is governed by identical second-order average Hamiltonian for both sequences, but SQ terms are generated in the single pulse case, which lowers the DQ excitation efficiency. Whereas the $X62_6^{31}$ sequence displays a distinct excitation efficiency dependence on crystallite orientation from the other two sequences. These differences are somewhat visible in the experimental lineshape. While neither sequence produces a spectrum with well-defined quadrupolar lineshape features, still based on the peak position and the lineshape width accurate quadrupolar products can be extracted.

We now turn to examine the DQ excitation amplitude dependence of $X2_2^1$ and $X62_6^{31}$ schemes on the third Euler angle γ_{QR}. Generally, if the magnitude of the excited or recoupled coherence depends on the γ_{QR} a time modulation due to this Euler angle is introduced. This modulation induces “artefact” spinning sidebands, which may overlap with genuine peaks. In Section 5.2.1 we argued that the $X62_6^{31}$ is γ-encoded, meaning that it is independent of γ_{QR}. In order to verify our predictions we acquired 2D D-DQ-HMQC spectra with a large spectral window in the indirect dimension of the two XN_n^ν sequences. To guarantee that the signal is not modulated by γ_{QR} due to the heteronuclear dipolar recoupling sequence we employed a previously reported γ-encoded sequence. [140] The obtained spectra are shown in Fig.5.5. As expected the spectrum acquired using $X2_2^1$ sequence gives rise to spinning sidebands in the indirect dimension, while for $X62_6^{31}$ spinning sidebands are not observed. Therefore, we were able to successfully design a γ-encoded sequence ($X62_6^{31}$) following the theoretical approach introduced in Paper III.

6

Determination of the electronic structure and hydride occupancy in barium titanium oxyhydride

Here we continue by demonstrating how the new NMR methods can be employed together with density functional theory calculations to aid in the elucidation of the electronic structure barium titanium oxyhydride $BaTiO_{3-x}H_y$. The material $BaTiO_{3-x}H_y$ is typically obtained by reduction of barium titanium oxide with a hydride anion containing compound. During the synthesis the oxide ions are substituted by hydride ions or expelled to form oxygen vacancies with stoichiometry $x-y$. Moreover, due to both processes electrons are introduced in the otherwise empty Ti 3d-band as a result the material becomes an electrical conductor. In addition, the oxyhydride exhibits hydride ion conduction. Due to the mixed electron-hydride ion conduction the material has seen considerable interest for the development of energy storage devices. In order to tailor the materials conduction properties for specific applications, we must first have a complete understanding of the underlying conduction mechanisms. [141; 142]

Previously, two hydride ion diffusion mechanisms have been proposed. In the first mechanism the hydride ion transforms into a proton and diffuses interstitially through the material. In the second mechanism the hydride ion diffusion occurs by hopping between available oxygen vacancies. A number of studies employing complementary methods, such as isotope exchange, [143] quantum chemical calculations, [144] quasielastic neutron scattering (QENS) [145] and inelastic neutron scattering (INS) [146] have demonstrated that the latter mechanism is more consistent with the experimental results. Although majority of the reports on the hydride ion conduction dynamics are in agreement, the electronic structure and the corresponding electrical conductivity mechanism remains a subject of dispute.

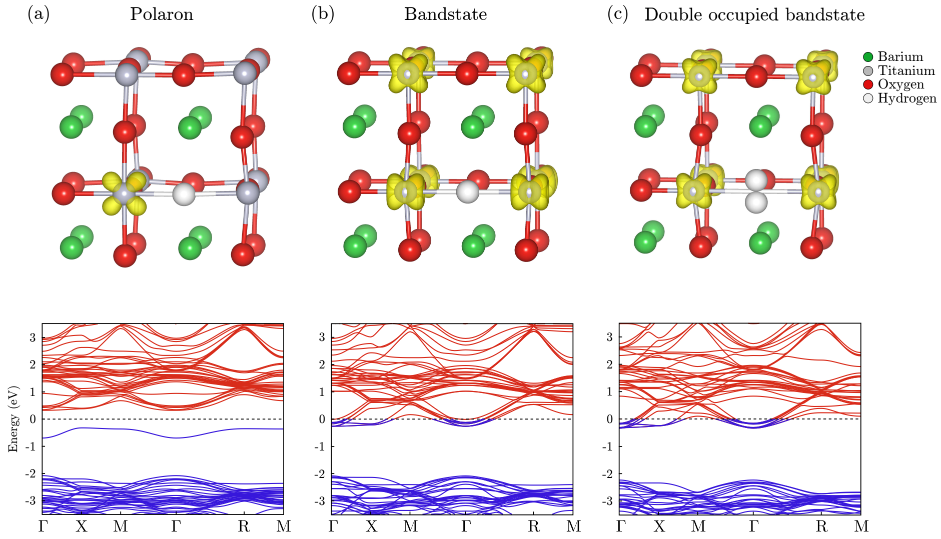

Figure 6.1: Possible electronic structures of barium titanium oxyhydride considered in this work. From left to right the DFT optimized $2 \times 2 \times 2$ supercells for a polaron (a), a bandstate (b) and a double occupied bandstate (c) scenarios are shown. Below the structures the corresponding DFT calculated electronic bandstructures are shown. The blue and red colours represent occupied and unoccupied levels, respectively. The unpaired spin density is given by the isosurface in yellow.

The first electrical conductivity experiments pointed towards a semiconducting mechanism in the bulk phase of $BaTiO_{3-x}H_y$. [141] However, the result was ambiguous since the measurements were carried out on a powder sample without sintering, which may give erroneous data due to grain-boundary effects. Recently, more reliable measurements have been performed on epitaxial thin films, which indicated that with low hydride content ($y < 0.2$) $BaTiO_{3-x}H_y$ is a semiconductor, whilst at high hydride content ($y > 0.2$) it is metallic. [147] A DFT study suggested that the observed semiconducting behaviour in the material is due to polaron formation. [144] Polarons are quasiparticles comprised of a charge carrier confined to a potential energy well that is self-generated by distorting the local lattice. [148] In $BaTiO_{3-x}H_y$ the substitution of an oxide ion with hydride adds an electron to the empty Ti 3d-band, where it can potentially localize generating an electron polaron (see Fig.6.1(a)). Thermally activated polarons can jump between neighboring Ti ions, hence the bulk phase would exhibit semiconductor-like conductivity. [149] More recently, a combined INS and DFT investigation indicated that the additional electron favors delocalization among all Ti 3d-bands leading to a bandstate configuration (see Fig.6.1(b)) with metallic electrical con-

Table 6.1: Isotropic shift of ^{2}H and ^{2}H concentration in $BaTiO_{3-x}D_y$

Sample	δ_{iso} (ppm)	^{2}H concentration (mol/f.u.)
$BTOD_{NAB}$	-8.3	0.13
$BTOD_{CA}$	-22	0.23
$BTOD_{EXCH}$	-39	0.31

ductivity. [150] Misaki et al. using solid-state NMR also concluded that the oxyhydride is more likely to have a bandstate electronic structure. However, in contrast to the previous report the authors proposed that the each hydride site in the bandstate is occupied by two hydrogens as shown in Fig.6.1(c). [151]

In an effort to finally resolve the electronic structure and occupancy in barium titanium oxyhydride in Paper IV we employ solid-state NMR combined with DFT calculations. We begin by examining the ^{1}H and ^{2}H MAS spectra of the oxyhydride. Followed by a comprehensive study of the ^{2}H environment by determining the quadrupolar and shift tensor components and the response of the parameters to temperature. The most important results of Paper IV are summarised in Sections 6.1-6.4.

6.1 Comparison of ^{1}H and ^{2}H solid-state NMR

Since the hydride ions are directly bonded to Ti ions we expect that ^{1}H or ^{2}H NMR parameters to be very sensitive on the Ti electronic configuration that is whether the 3d electrons form localized polarons (Fig.6.1(a)) or delocalize among all Ti (Fig.6.1(b) and 6.1(c)). ^{1}H spectrum acquired under MAS is given in Fig.6.2(a), which shows that for ^{1}H we have additional signals due to surface-adsorbed water and/or hydroxyl groups. These background resonances overlap with the hydride signal, hence complicating quantitative and qualitative analysis of the spectrum. Therefore, ^{2}H appears to be a better “spy” nucleus to probe the electronic structure of the material, furthermore, ^{2}H is subject to the quadrupolar interaction, which later will prove to be crucial for discerning the hydrogen occupancy.

Consequently, deuterated versions of $BaTiO_{3-x}H_y$ were prepared. In total three samples were synthesized. Two were obtained by reducing $BaTiO_3$ with $NaBD_4$ and CaD_2, while in the third case $BaTiO_3$ was reduced with CaH_2 followed by a hydride ion exchange with deuterium D_2. Henceforth each sample is referred to as $BTOD_{NAB}$, $BTOD_{CA}$ and $BTOD_{EXCH}$, respectively. The corresponding ^{2}H MAS spectra of each sample are shown in Fig.6.2(b). As expected, the spectra are void of any resonances in the region of $0-6$ ppm, which indicates that surface-adsorbed water and hydroxyl groups are not deuterated. The $BTOD_{NAB}$ and $BTOD_{CA}$ samples give a single resonance with a negative shift corresponding to the hydride ion, while $BTOD_{EXCH}$ shows two hydrogen environments at -39 and -150 ppm. A previous study reported that in TiD_2 ^{2}H has a shift of approximately -150 ppm and so we assign the second resonance in $BTOD_{EXCH}$ to this impurity phase. [152] Finally, using the ^{2}H spectra we are able to quantify the hydride content in each sample. The hydride isotropic shifts are given in Table 6.1, along with the determined hydride concentration y.

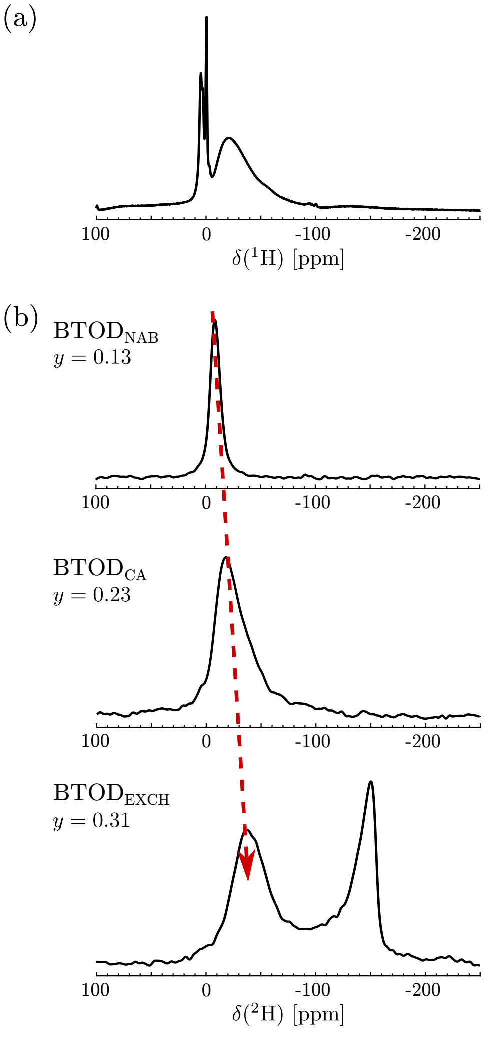

Figure 6.2: MAS NMR spectra of barium titanium oxyhydrides. (a) shows the ^{1}H spectrum at 60 kHz MAS of unlabeled barium titanium oxyhdyride. In (b) from top to bottom are given ^{2}H spectra at 30 kHz MAS of BTOD$_{\text{NAB}}$, BTOD$_{\text{CA}}$ and BTOD$_{\text{EXCH}}$, with their determined hydride contents y.

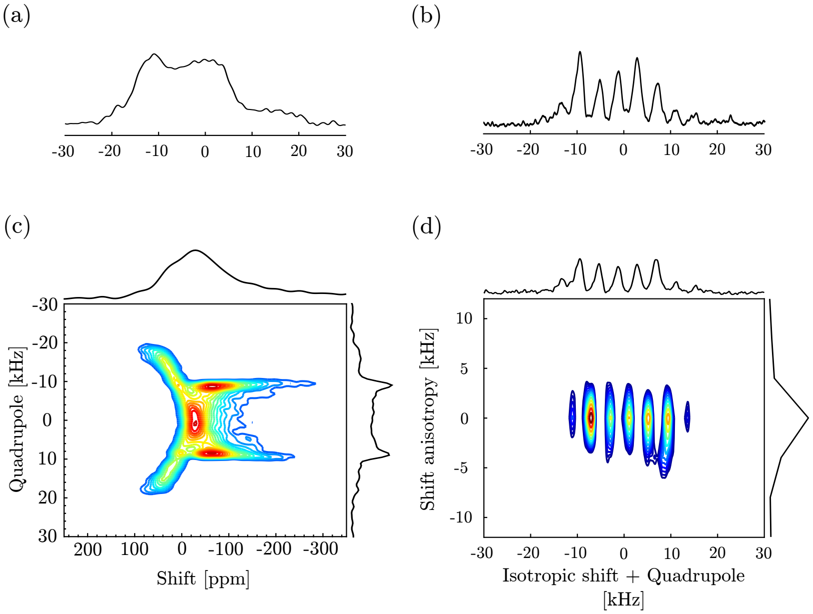

Figure 6.3: Experimental ^{2}H spectra of BTOD$_{\mathrm{CA}}$ under static and MAS conditions. The static 1D and 4 kHz MAS spectra are shown in (a) and (b), respectively. The static 2D adiabatic shifting *d*-echo experiment and 2D PASS at 4kHz MAS are given in (c) and (d), respectively.

6.2 Determination and analysis of the quadrupole and shift tensor parameters

Needless to say, the spectra in Fig.6.2(b) obtained under 30 kHz completely average the anisotropic parts of each interaction and no information about the orientation dependence of the interaction tensors is available. Therefore, in order to extract the interaction tensor parameters we need to acquire spectra at lower spinning frequencies or under static condition. The static and 4 kHz MAS 1D spectra of ^{2}H in BTOD$_{\mathrm{CA}}$ are shown in Fig.6.3(a) and 6.3(b). Both the static powder pattern and sideband manifold are essentially featureless and individual tensor parameters cannot be recovered. In previous sections we introduced experiments that are tailored for analyzing such ^{2}H environments by separating the shift and first-order quadrupolar interactions. The sheared spectra obtained using the static adiabatic shifting *d*-echo and 4 kHz MAS PASS experiments are given in Fig.6.3(c) and 6.3(d). The dimension with the quadrupolar interaction for both spectra give rise to pristine Pake doublets. However, in the shift anisotropy dimension of the PASS spectrum only four sidebands are detected, which implies that accurate anisotropic information or the Euler angles relating the two interactions cannot be procured. On the other hand, the adiabatic shifting *d*-echo experiment allows determination of these parameters, hence has an advantage over the PASS sequence for this system. Thus, we acquired adiabatic shifting *d*-echo spectra for all three samples.

The sheared adiabatic shifting *d*-echo spectra of all three BTOD samples are shown in Fig.6.4. Apart from the sharp peak at zero frequency due to the impurity (TiD_2) in $BTOD_{EXCH}$, the spectral features of the ^2H resonance qualitatively are very similar in the three samples. Surprisingly, despite the presence of oxygen vacancies and anionic disorder in the lattice the spectra exhibit very well-defined Pake doublets in the quadrupole dimension, which implies that hydride ions exhibit uniform local structure throughout the material. To obtain a more quantitative assessment of the NMR parameters we proceed by fitting the spectra. The best fit and the best fit residual spectra are shown in Fig.6.4 and the extracted tensor components are summarised in Table 6.2. We notice that the quadrupolar tensor components and the Euler angles match within margin of error among the studied samples, which indicates that the different samples have equivalent local hydride environments and electronic structures.

With the knowledge that the electronic structure is consistent between the different samples we continue by elucidating the electronic state. We note that the ^2H shift tensor displays significant differences among the samples (see Table 6.2). Before we explain this observation, we comment on the discrepancy in the isotropic shift value between the static and MAS methods. Firstly, due to the broad lineshape in static sample the fit provides a lower accuracy for the determination of the isotropic shift value. [153] Second, the available model used for the fit does not account for isotropic shift and shift anisotropy distribution resulting from structural disorder. Hence, the isotropic shift values estimated from MAS experiments (Table 6.1) are used to draw conclusions about the properties of the material. The observed ^2H isotropic shifts are far outside the standard $^1H/^2H$ shift range of $0-12$ ppm, which suggest that the nuclei experience a hyperfine field due to unpaired electrons. In the case of the polaronic state the hyperfine interaction occurs with the electron polaron, while for the bandstate with the conduction electrons. We anticipate that the dominant contribution to the shift will arise from the Fermi contact term. [18; 154]

If we treat the polaronic state as a paramagnetic insulator, then the shift depends on the transferred spin density to the hydrogen s-orbital $\rho^{\alpha-\beta}(0)$ (see Eq.2.90) and so the shift should be additive with respect to the number of adjacent paramagnetic centres (polarons). In the present case, we foresee two possible configurations with either one or two polarons next to the hydride ion. Therefore, we conjecture that with increasing hydride content (potentially increasing electron polaron concentration) a second shift should emerge at -16.6 ppm, which is twice the shift position of ^2H in $BTOD_{NAB}$. However, this does not occur experimentally.

For the bandstate the FC part of the Knight shift is proportional to the density of states at the Fermi level (see Eq.2.91), hence depends on the number of electrons in the conduction band (3d-band of Ti). As mentioned earlier, by substitution of oxide ions with hydride ions an electron is donated to the the 3d-band of Ti, and so with increasing hydride content the number of conduction electrons is expected to increase. Thus, the isotropic shift becoming more negative with higher hydride concentrations (see Table 6.1) is ascribed to the metallic character of the oxyhydride. Furthermore, the negative sign of the shift is associated with the

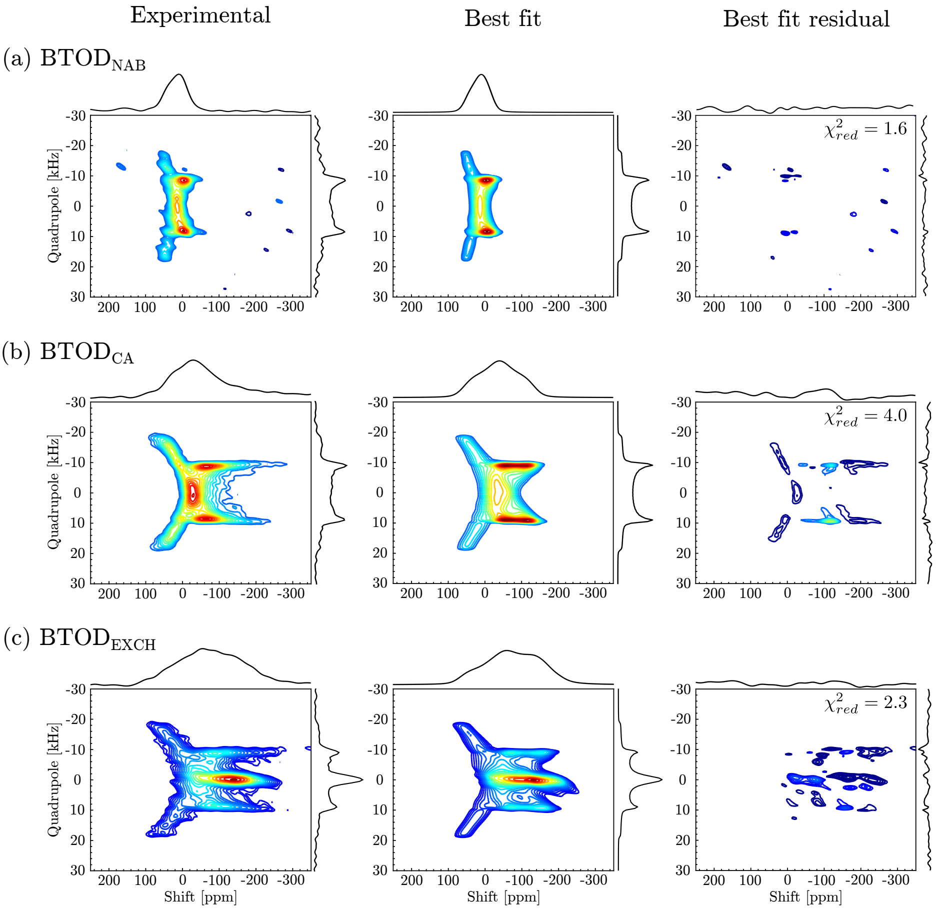

Figure 6.4: 2D static shifting *d*-echo NMR spectra of different BTOD samples. From left to right are given experimental, best fit and best fit residual spectra of BTOD$_{\text{NAB}}$ (a) and BTOD$_{\text{CA}}$ (b) and BTOD$_{\text{EXCH}}$ (c).

Table 6.2: Best fit shift and quadrupolar tensor parameters and errors for the 2D adiabatic shifting *d*-echo spectra of $\mathrm{BTOD_{NAB}}$, $\mathrm{BTOD_{CA}}$ and $\mathrm{BTOD_{EXCH}}$.

Sample	δ_{iso} (ppm)	$\Delta\delta$ (ppm)	η_S	C_Q (kHz)	η_Q
$\mathrm{BTOD_{NAB}}$	-5.8 ± 0.3	40.1 ± 0.3	0.76 ± 0.08	24.2 ± 1.7	0.06 ± 0.06
$\mathrm{BTOD_{CA}}$	-55.2 ± 0.3	97.0 ± 0.7	0.99 ± 0.01	25.2 ± 0.3	0.03 ± 0.03
$\mathrm{BTOD_{EXCH}}$	-53.4 ± 0.2	120.8 ± 0.8	0.98 ± 0.02	25.4 ± 0.3	0.06 ± 0.03

Sample	α (°)	β (°)	γ (°)
$\mathrm{BTOD_{NAB}}$	44 ± 7	0 ± 7	0 ± 7
$\mathrm{BTOD_{CA}}$	34 ± 1	0.7 ± 0.4	0.6 ± 0.3
$\mathrm{BTOD_{EXCH}}$	33 ± 2	0.7 ± 0.4	1.0 ± 0.5

polarization mechanism, which means that the conduction electrons in the $\mathrm{t_{2g}}$ band polarize the $\mathrm{e_g}$ band, resulting in a negative spin density of hydride s-band and consequently a negative contact shift. [155–157] We conjecture that for the double occupied bandstate the spin density would be transferred via the delocalisation mechanism, since the position of the hydride ions allows direct overlap between the H s orbitals and the Ti $\mathrm{t_{2g}}$ orbital. Therefore, a positive contact shift is expected. Next we consider the shift anisotropy, which has contributions from the orbital and spin-dipolar parts of the Knight shift. We note that the SD term depends on the density of states at the Fermi level and so the anisotropy should increase in magnitude with higher hydride concentrations, which explains experimentally observed relationship between shift anisotropy (see Table 6.1) and the hydride content.

Collectively these data provide strong evidence that the barium titanium oxyhydrides have a bandstate electronic structure and the NMR shift corresponds to the Knight shift. Finally, we call attention to the lineshapes of the MAS spectra in Fig.6.2 and of the static shift projection in Fig.6.4 both of which display a skew towards negative frequencies. Possibly, different crystallites in the sample have distinct hydride or oxygen vacancy concentrations, which lead to a distribution of Knight shifts. This corroborates our explanation about the differences in the observed isotropic values determined from static or MAS methods.

6.3 Temperature dependence of NMR parameters

Until now, we have discussed the shift tensor parameter dependence on the hydride content, which has suggested that the studied material adopts a bandstate configuration. We provide further support for the bandstate electronic structure by measuring the temperature dependence of NMR parameters. As discussed in Section 2.3.4 in simple metals according to the Korringa relation the quantity T_1TK^2 is constant as function of temperature. [60] The determined experimental quantity T_1TK^2 of $\mathrm{BTOD_{CA}}$ is given in Fig.6.5, which indeed shows a constant trend in the temperature range $100-300$ K. The observation of the Korringa relation gives unambiguous evidence that the material has a bandstate electronic structure and would

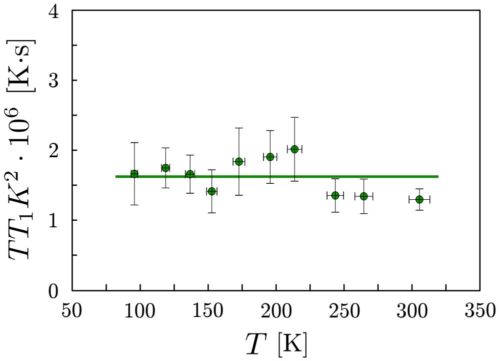

Figure 6.5: Temperature dependence of NMR parameters. The plot displays the quantity T_1TK^2 of ^{2}H in BTOD$_{\mathrm{CA}}$ as a function of temperature.

exhibit metallic conductivity.

6.4 Density functional theory calculations

The presented data have given strong indication that the electrons form delocalized bandstates which is in agreement with previous INS [150] and solid-state NMR [151; 158] studies. However, we have only speculated about the hydride occupancy based on the sign of the contact shift. To completely resolve this issue we employ DFT to compute the EFG tensor parameters for each of the structures in Fig.6.1. Due to the discussed self-interaction error the 3d Ti electrons are excessively delocalized and the polaronic state cannot be obtained using GGA functionals. Therefore, we utilize the DFT+U method instead and treat the Ti 3d electrons with an additional Hubbard-like term U. The optimal U value was chosen so that the total electronic energy is linearly dependent on the charge population of the polaron level (see Fig.6.6). [150; 159; 160] The deviation from piecewise linearity of system energy as function of the polaron level population is shown in Fig.6.6. We notice for the value of $U = 2.7$ eV the relation is closest to being linear. However, following this approach for the double occupied bandstate the electrons in the 3d-band of Ti were overlocalized leading to an unreliable electronic structure, therefore for this case we carried out the calculations without the U correction.

The DFT optimized geometries, the calculated spin density distribution and the bandstructure of the three BTOH configurations consider here are shown in Fig.6.1. We can see from the bandstructures that the two bandstates exhibit conduction bands crossing the Fermi level, while the polaron has a narrow band gap of ~ 0.65 eV. Establishing that we have the correct electronic structures we proceed with ^{2}H EFG tensors calculations. The obtained quadrupolar parameters are given in Table 6.3 together with the experimental values

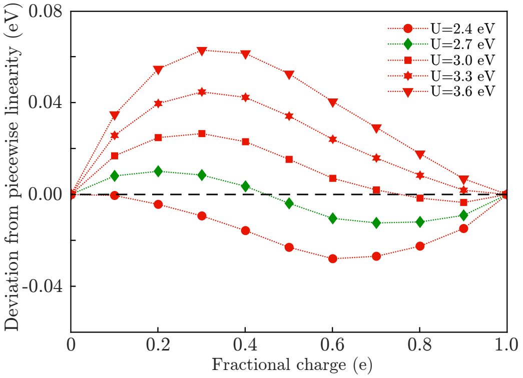

Figure 6.6: Deviation from linearity of the total electronic energy as a function of the charge of the system. The plots with suboptimal and optimal U values are given in red and green, respectively. The calculations were performed on a $2 \times 2 \times 2$ supercell with $BaTiO_{2.875}H_{0.125}$ composition in the polaronic state.

of $BTOD_{CA}$ for comparison. The polaron and single occupied bandstate quadrupolar parameters are very similar and differentiation between the two experimentally would not be possible. However, the double occupied bandstate ^2H quadrupolar parameters are distinct with a quadrupolar coupling larger by a factor of 3 than for the other two structures. We note that overall the calculated quadrupolar parameters of single occupied bandstate matches reasonably well with the experimental values (see Table 6.2). The discrepancy in the quadrupolar coupling constant between DFT values and experiment can be explained by the presence of vibrational [146; 150] and/or diffusion [143–145] dynamics of the hydride, which can average the EFG tensor parameters and consequently lower the quadrupolar coupling constant. Taking into consideration these possible dynamic effects on the EFG tensor, the calculations indicate that the vacant oxygen sites are occupied by a single hydrogen.

In conclusion, we have demonstrated that barium titanium oxyhydride has a bandstate electronic structure with hydride sites occupied by a single hydrogen. Moreover, we have showed that DFT-assisted solid-state NMR is an exceptional tool for studying the hydride ion local environment and for differentiating between the electron-nuclear hyperfine coupling due to electron polarons and conduction electrons.

Table 6.3: DFT computed and $BTOD_{CA}$ quadrupolar tensor parameters

State	C_Q (kHz)	η_Q
Polaron	62.5	0.08
Bandstate	60.9	0.0
Double occupied banstate	193.7	0.39
$BTOD_{CA}$	25.2 ± 0.3	0.03 ± 0.03

7

Summary

In recent years, the study of paramagnetic systems by solid-state NMR has experienced an increased activity due to advancements in NMR probe design and development of pulse sequences. While the current approaches perform well for spin $I = 1/2$ nuclei, several limitations still remain for quadrupolar nuclei ($I > 1/2$). This Thesis contributes to the theoretical description of pulse schemes and adds new sequences to the arsenal of NMR methodology for spin $I = 1$ nuclei in paramagnetic systems.

We first undertook the issue of deconvolving spectra of spin $I = 1$ nuclei subject to quadrupolar and paramagnetic shift interactions, and BMS effects. This was achieved by separating the shift (including the isotropic shift, shift anisotropy and BMS effects) from the first-order quadrupolar interaction. Several NMR approaches in static solids had been reported previously for the separation of the two interactions, however, the different methods are a compromise between poor excitation bandwidth and sensitivity. Furthermore, all the methods are susceptible to the formation of an artefact in the spectrum. Here we demonstrated that by combining the preceding shifting d-echo sequence with short-high power adiabatic pulses, artefact free experiments with high sensitivity and broad excitation bandwidth can be obtained.

Secondly, we examined whether the separation could be achieved in spinning solids, since this would increase the sensitivity and resolution and open new avenues to study systems with multiple distinct resonances. We show that the previously reported phase-adjust spinning sideband method, which was originally intended for separation of the isotropic shift and the shift anisotropy, can be utilized to separate and correlate the shift anisotropy with the first-order quadrupolar interaction. This is the first example of a sequence for separation of the two interactions under MAS.

Thirdly, we addressed the excitation of large anisotropic interactions with low-power pulses under MAS. To this end, we derived a new theoretical framework for analyzing low-power phase-modulated pulse schemes applied to nuclei subject to anisotropic interaction(s) much larger than the spinning frequency. The methodology is analogous to the symmetry-based pulse sequences, however, applicable to the low-power regime. We employed the formalism to describe previously reported DQ excitation schemes for spin $I = 1$ nuclei and introduced new sequences, including a γ-encoded scheme.

Finally, we applied the static and MAS methods for separation of the quadrupolar and shift interactions to study the electronic structure of a mixed electron-ion conductor barium titanium oxyhydride. By employing the new adiabatic shifting d-echo sequence we were able to extract accurate quadrupolar tensor parameters, which showed that the local hydride environment does not change with the material composition, hence the electronic structure is equivalent in each sample. Thus, the shift parameter dependence on the material composition could be associated with metallic behaviour, which was corroborated by the observed Korringa relation. Lastly, by calculating the electric-field gradient tensor with density functional theory we concluded that each hydride site occupies a single hydride ion.

In conclusion, we anticipate that the new methods provided in this work will be very beneficial for investigating local hydrogen environments in different types of materials. We foresee that improvement in the excitation bandwidth of the phase-adjusted spinning sideband sequence could increase the scope of the method even further. Finally, since the new theoretical formalism is general it could open new horizons for the development of novel low-power sequences for the excitation of spin systems subject to large anisotropic interactions.

7.1 Sammanfattning

Under de senaste åren har studier av paramagnetiska systemet med fasta tillståndet kärnmagnetiskresonans (NMR) spektroskopi upplevt en ökad aktivitet, på grund av framsteg inom NMR-probdesign och utveckling av pulssekvenser. Även om de nuvarande metoderna fungerar bra för spinn $I = 1/2$ kärnor, kvarstår flera begränsningar fortfarande för kvadrupolära kärnor ($I > 1/2$). Denna avhandling bidrar till den teoretiska beskrivningen av pulsscheman och lägger till nya sekvenser till arsenalen av NMR-metodiken för spinn $I = 1$ kärnor i paramagnetiska system.

Vi fokuserade först på problemet att analysera spektra av spinn $I = 1$ kärnor som är inkluderar kvadrupol- och paramagnetiska kemiskt skiftinteraktioner. Detta uppnåddes genom att separera skiftet (inklusive det isotropa skiftet samt, skiftanisotropi) från kvadrupol interaktionen. Flera NMR-metoder för statiska fasta ämnen hade tidigare rapporterats för separationen av de två interaktionerna, men dessa är en kompromiss mellan dålig excitationsbandbredd och känslighet. Dessutom, var dessa metoder känsliga för bildandet ave artefakter i spektrumet. Genom att kombinera den tidigare utvecklad skiftande d-ekosekvensen med korta högeffekts adiabatiska pulser, introducerades artefaktfria experiment med hög känslighet och bred excitationsbandbredd.

Dessutom, undersökte vi om separationen kunde uppnås i roterande fasta ämnen, eftersom detta skulle öka känsligheten och upplösningen samt öppna nya vägar för att studera system med flera distinkta resonanser. Vi visade att den tidigare rapporterade fasjusterande spinnande sidobandsmetoden, som ursprungligen var avsedd för separation av det isotropa kemiska skiftet och skiftanisotropin, kan användas för att separera och korrelera skiftanisotropin med den kvadrupolära interaktionen. Detta är det första exemplet på en sekvens för separation av de två interaktionerna under Magic-angle spinning (MAS).

Vidare, behandlade vi excitationen av stora anisotropa interaktioner med lågeffektpulser under MAS. För detta ändamål härledde vi ett nytt teoretiskt ramverk för att analysera lågeffektfasmodulerade pulsscheman som tillämpas på kärnor som är föremål för anisotrop interaktion som är mycket större än rotationsfrekvensen. Metodiken är analog med de olika symmetribaserade pulssekvenserna. Vi tillämpade formalismen för att beskriva tidigare rapporterade DQ-excitationsscheman för spin $I = 1$ och introducerade nya sekvenser, inkluderande ett γ-kodat schema.

Slutligen tillämpade vi de statiska och MAS-metoderna för separation av de kvadrupol och skift interaktionerna för att studera den elektroniska strukturen hos en blandad elektron-jonledare av bariumtitanoxihydrid. Genom att använda den nya adiabatiska skiftande d-ekosekvensen kunde vi extrahera noggranna kvadrupol tensorparametrar, vilket visade att den lokala hydridmiljön inte förändras med materialsammansättningen, därför är den elektroniska strukturen är ekvivalent i varje prov. Således kan skiftparameterberoendet på materialsammansättningen associeras med materialens metalliska beteende, vilket bekräftades av den observerade Korringa-relationen. Slutligen, genom att beräkna det elektriska fältets gradienttensor med hjälp av densitetsfunktionella teorin drog vi slutsatsen att varje hydridplats upptar en enda hydridjon.

Sammanfattningsvis förväntar vi oss att de nya metoder som har utvecklats i detta arbete kommer att vara mycket fördelaktiga för att undersöka lokal vätemiljö i olika typer av material. Vi förutser att förbättring av excitationsbandbredden för den fasjusterade spinnande sidosekvensen kan öka omfattningen av metoden ytterligare. Slutligen, eftersom den nya teoretiska formalismen är allmän kan den öppna nya horisonter för upptäckt av nya lågeffektsekvenser för excitering av de flesta spinnsystem som är föremål för stora anisotropa interaktioner.

Acknowledgements

First, I would like to express my deepest gratitude to my supervisor Prof. Andrew J. Pell for the invaluable education on NMR theory and the guidance throughout the PhD. In particular, I am grateful for the continuous availability to discuss details of spin dynamics and the willingness to entertain any NMR ideas that arose.

I would also like to thank my co-supervisor Prof. Ulrich Häussermann for providing the opportunity to employ the new NMR methods to study more complex materials than model systems.

I would like to offer a special thanks to Prof. Arnold Maliniak for his patience, understanding and assistance throughout the PhD. Without his help finishing the PhD would have been very painful at best.

I am also grateful to Prof. Guido Pintacuda, who provided the opportunity to conduct experiments at CRMN. Furthermore, a big thanks to Dr. David Gajan, Georges Menzildjian and Thomas Robinson for the practical help on setting up low-temperature experiments.

Also I would like to thank all of the office/group mates over years: Lorenzo, Elodie, Min and Lucia. Especially, I would like to thank Aleks for showing the first steps in solid-state NMR. Most importantly, I am grateful for my fellow PhD peers José and Wassilios, with who plenty of loops were converged (some still open), many fortresses of logic were built, several fear-mongering occasions were endured and countless adventures were enjoyed.

My gratitude goes to all the new friends in MMK and outside, in particular Ellie, Niko, Annie and Andreas. Also I want to thank the climbing mates (Dimi, José) and the skateboarding crew (Ken, Erik, José) for the many fun times.

I am thankful also for the support from my friends back home, mainly Valdis and Agris.

I am very grateful to all my previous teachers in school, at the university and my former colleagues at the Latvian institute of organic synthesis. Special thanks to prof. Kristaps Jaudzems and prof. Edvards Liepiņš who introduced me to NMR and instilled good scientific practices. Without the education provided by these people I would surely not have gotten this far.

Finally, huge thank you goes to my family for the relentless help and support over the last 4 years and before. Liels paldies!

References

[1] Michael S Whittingham. Electrical energy storage and intercalation chemistry. *Science*, 192 (4244):1126–1127, 1976.

[2] Sumio Iijima and Toshinari Ichihashi. Single-shell carbon nanotubes of 1-nm diameter. *Nature*, 363(6430):603–605, 1993.

[3] Markus Konig, Steffen Wiedmann, Christoph Brune, Andreas Roth, Hartmut Buhmann, Laurens W Molenkamp, Xiao-Liang Qi, and Shou-Cheng Zhang. Quantum spin Hall insulator state in HgTe quantum wells. *Science*, 318(5851):766–770, 2007.

[4] Su-Yang Xu, Ilya Belopolski, Nasser Alidoust, Madhab Neupane, Guang Bian, Chenglong Zhang, Raman Sankar, Guoqing Chang, Zhujun Yuan, Chi-Cheng Lee, et al. Discovery of a Weyl fermion semimetal and topological Fermi arcs. *Science*, 349(6248):613–617, 2015.

[5] James D Watson and Francis HC Crick. Molecular structure of nucleic acids: a structure for deoxyribose nucleic acid. *Nature*, 171(4356):737–738, 1953.

[6] John C Kendrew, G Bodo, Howard M Dintzis, RG Parrish, Harold Wyckoff, and David C Phillips. A three-dimensional model of the myoglobin molecule obtained by X-ray analysis. *Nature*, 181 (4610):662–666, 1958.

[7] Wim GJ Hol. Protein crystallography and computer graphics—toward rational drug design. *Angewandte Chemie International Edition in English*, 25(9):767–778, 1986.

[8] Michael J Hartshorn, Christopher W Murray, Anne Cleasby, Martyn Frederickson, Ian J Tickle, and Harren Jhoti. Fragment-based lead discovery using X-ray crystallography. *J. Med. Chem.*, 48(2):403–413, 2005.

[9] Laurent Maveyraud and Lionel Mourey. Protein X-ray crystallography and drug discovery. *Molecules*, 25(5):1030, 2020.

[10] Hans Wolfgang Spiess. 50th anniversary perspective: The importance of NMR spectroscopy to macromolecular science. *Macromolecules*, 50(5):1761–1777, 2017.

[11] Robert Tycko. Solid-state NMR studies of amyloid fibril structure. *Annu. Rev. Phys. Chem.*, 62: 279–299, 2011.

[12] Gemma Comellas and Chad M Rienstra. Protein structure determination by magic-angle spinning solid-state NMR, and insights into the formation, structure, and stability of amyloid fibrils. *Annual review of biophysics*, 42:515–536, 2013.

[13] Mattias Edén. NMR studies of oxide-based glasses. *Annu. Rep. Prog. Chem., Sect. C: Phys. Chem.*, 108(1):177–221, 2012.

[14] Randall Youngman. NMR spectroscopy in glass science: A review of the elements. *Materials*, 11(4):476, 2018.

[15] Aaron J Rossini, Alexandre Zagdoun, Moreno Lelli, Anne Lesage, Christophe Coperet, and Lyndon Emsley. Dynamic nuclear polarization surface enhanced NMR spectroscopy. *Acc. Chem. Res.*, 46(9):1942–1951, 2013.

[16] Bradley F Chmelka. Materializing opportunities for NMR of solids. *J. Magn. Reson.*, 306: 91–97, 2019.

[17] Robert J Messinger, Michel Ménétrier, Elodie Salager, Adrien Boulineau, Mathieu Duttine, Dany Carlier, Jean-Marcel Ateba Mba, Laurence Croguennec, Christian Masquelier, Dominique Massiot, et al. Revealing defects in crystalline lithium-ion battery electrodes by solid-state NMR: applications to $LiVPO_4F$. *Chem. Mater.*, 27(15):5212–5221, 2015.

[18] Andrew J Pell, Guido Pintacuda, and Clare P Grey. Paramagnetic NMR in solution and the solid state. *Prog. Nucl. Magn. Reson. Spectrosc.*, 111:1–271, 2019.

[19] Ivano Bertini, Claudio Luchinat, and Giacomo Parigi. Magnetic susceptibility in paramagnetic NMR. *Prog. Nucl. Magn. Reson. Spectrosc.*, 40(3):249, 2002.

[20] Clare P Grey and Nicolas Dupré. NMR studies of cathode materials for lithium-ion rechargeable batteries. *Chem. Rev.*, 104(10):4493–4512, 2004.

[21] Julia Koehler and Jens Meiler. Expanding the utility of NMR restraints with paramagnetic compounds: background and practical aspects. *Prog. Nucl. Magn. Reson. Spectrosc.*, 59(4):360, 2011.

[22] Roberta Pigliapochi, Liam O'Brien, Andrew J Pell, Michael W Gaultois, Yuri Janssen, Peter G Khalifah, and Clare P Grey. When do anisotropic magnetic susceptibilities lead to large NMR shifts? Exploring particle shape effects in the battery electrode material $LiFePO_4$. *J. Am. Chem. Soc.*, 141(33):13089–13100, 2019.

[23] Nikolaos Panopoulos, Michael Pissas, Hae Jin Kim, Jin-Gyu Kim, Seung Jo Yoo, Jamal Hassan, Yasser Al Wahedi, Saeed Alhassan, Michael Fardis, Nikos Boukos, et al. Polaron freezing and the quantum liquid-crystal phase in the ferromagnetic metallic $La_{0.67}Ca_{0.33}MnO_3$. *npj Quantum Mater.*, 3(1):1–8, 2018.

[24] Wassilios Papawassiliou, Aleksander Jaworski, Andrew J Pell, Jae Hyuck Jang, Yeonho Kim, Sang-Chul Lee, Hae Jin Kim, Yasser Alwahedi, Saeed Alhassan, Ahmed Subrati, et al. Resolving Dirac electrons with broadband high-resolution NMR. *Nat. Comm.*, 11(1):1–7, 2020.

[25] Nalinda P Wickramasinghe, Medhat Shaibat, and Yoshitaka Ishii. Enhanced sensitivity and resolution in ^1H solid-state NMR spectroscopy of paramagnetic complexes under very fast magic angle spinning. *J. Am. Chem. Soc.*, 127(16):5796–5797, 2005.

[26] Gwendal Kervern, Guido Pintacuda, and Lyndon Emsley. Fast adiabatic pulses for solid-state NMR of paramagnetic systems. *Chem. Phys. Lett.*, 435(1-3):157–162, 2007.

[27] Gwendal Kervern, Stefan Steuernagel, Frank Engelke, Guido Pintacuda, and Lyndon Emsley. Absence of Curie relaxation in paramagnetic solids yields long ^{1}H coherence lifetimes. *J. Am. Chem. Soc.*, 129(46):14118–14119, 2007.

[28] Andrew J Pell, Raphaële J Clément, Clare P Grey, Lyndon Emsley, and Guido Pintacuda. Frequency-stepped acquisition in nuclear magnetic resonance spectroscopy under magic angle spinning. *J. Phys. Chem.*, 138(11):114201, 2013.

[29] Anatole Abragam. *The principles of nuclear magnetism*. Oxford university press, 1961.

[30] Shimon Vega. Fictitious spin 1/2 operator formalism for multiple quantum NMR. *J. Chem. Phys.*, 68(12):5518–5527, 1978.

[31] Harvey A Buckmaster, Ramananda Chatterjee, and YH Shing. The application of tensor operators in the analysis of EPR and ENDOR spectra. *Phys. Stat. Sol. A*, 13(1):9–50, 1972.

[32] Ulrich Haeberlen. *Advances in magnetic resonance*, volume 1. Academic Press, 1976.

[33] Ulrich Haeberlen and John S Waugh. Coherent averaging effects in magnetic resonance. *Phys. Rev.*, 175(2):453, 1968.

[34] Sharon E Ashbrook, Jamie McManus, Michael J Thrippleton, and Stephen Wimperis. Second-order cross-term interactions in high-resolution MAS NMR of quadrupolar nuclei. *Prog. Nucl. Magn. Reson. Spectrosc.*, 55(2):160–181, 2009.

[35] David M Brink and George R Satchler. *Angular Momentum*. Clarendon Press Oxford, 1993.

[36] Philip J Grandinetti, Jason T Ash, and Nicole M Trease. Symmetry pathways in solid-state NMR. *Prog. Nucl. Magn. Reson. Spectrosc.*, 59(2):121, 2011.

[37] Malcolm H Levitt. Why do spinning sidebands have the same phase? *J. Magn. Reson.*, 82(2): 427–433, 1989.

[38] Mattias Edén. Computer simulations in solid-state NMR. I. Spin dynamics theory. *Concept. Magn. Reson. A*, 17(1):117–154, 2003.

[39] Mattias Edén. Computer simulations in solid-state NMR. II. Implementations for static and rotating samples. *Concept. Magn. Reson. A*, 18(1):1–23, 2003.

[40] Mattias Edén. Computer simulations in solid-state NMR. III. Powder averaging. *Concept. Magn. Reson. A*, 18(1):24–55, 2003.

[41] John H Van Vleck. The dipolar broadening of magnetic resonance lines in crystals. *Phys. Rev.*, 74(9):1168, 1948.

[42] Hans Primas. Generalized perturbation theory in operator form. *Rev. Mod. Phys.*, 35(3):710, 1963.

[43] Maurice Goldman, Philip J Grandinetti, A Llor, Zbigniew Olejniczak, Joseph R Sachleben, and Josef W Zwanziger. Theoretical aspects of higher-order truncations in solid-state nuclear magnetic resonance. *J. Chem. Phys.*, 97(12):8947–8960, 1992.

[44] Michal Leskes, PK Madhu, and Shimon Vega. Floquet theory in solid-state nuclear magnetic resonance. *Prog. Nucl. Magn. Reson. Spectrosc.*, 57(4):345–380, 2010.

[45] Ingo Scholz, Jacco D van Beek, and Matthias Ernst. Operator-based Floquet theory in solid-state NMR. *Solid State Nucl. Magn. Reson.*, 37(3-4):39–59, 2010.

[46] Michael Mehring. *Principles of high resolution NMR in solids*. Springer Verlag, Berlin, 1983.

[47] Andreas Brinkmann. Introduction to average Hamiltonian theory. I. Basics. *Concept. Magn. Reson. A*, 45(6):e21414, 2016.

[48] Wilhelm Magnus. On the exponential solution of differential equations for a linear operator. *Commun. Pure Appl. Math.*, 7(4):649–673, 1954.

[49] Zdeněk Tošner, Armin Purea, Jochem O Struppe, Sebastian Wegner, Frank Engelke, Steffen J Glaser, and Bernd Reif. Radiofrequency fields in MAS solid state NMR probes. *J. Magn. Reson.*, 284:20–32, 2017.

[50] Michael Garwood and Lance DelaBarre. The return of the frequency sweep: designing adiabatic pulses for contemporary NMR. *J. Magn. Reson.*, 153(2):155–177, 2001.

[51] Michaël Deschamps, Gwendal Kervern, Dominique Massiot, Guido Pintacuda, Lyndon Emsley, and Philip J Grandinetti. Superadiabaticity in magnetic resonance. *J. Chem. Phys.*, 129(20): 204110, 2008.

[52] Norman F Ramsey. Magnetic shielding of nuclei in molecules. *Physical Review*, 78(6):699, 1950.

[53] Teemu O. Pennanen and Juha Vaara. Nuclear magnetic resonance chemical shift in an arbitrary electronic spin state. *Phys. Rev. Lett.*, 100:133002, Apr 2008. doi: 10.1103/PhysRevLett.100.133002.

[54] Anatole Abragam and Brebis Bleaney. *Electron paramagnetic resonance of transition ions*. Oxford University Press, 1970.

[55] Martin Kaupp, Michael Buhl, and Vladimir G Malkin. *Calculation of NMR and EPR Parameters*. Wiley Online Library, 2004.

[56] Ivano Bertini, Claudio Luchinat, and Giacomo Parigi. *Solution NMR of paramagnetic molecules: applications to metallobiomolecules and models*. Elsevier, 2001.

[57] Walter D Knight. Nuclear magnetic resonance shift in metals. *Phys. Rev.*, 76(8):1259, 1949.

[58] Charles H Townes, Conyers Herring, and Walter D Knight. The effect of electronic paramagnetism on nuclear magnetic resonance frequencies in metals. *Physical Review*, 77(6):852, 1950.

[59] Charles P Slichter. *Principles of magnetic resonance*, volume 1. Springer Berlin, 1990.

[60] Jan Korringa. Nuclear magnetic relaxation and resonnance line shift in metals. *Physica*, 16(7-8): 601–610, 1950.

[61] Madis Alla and Endel T Lippmaa. Resolution limits in magic-angle rotation NMR spectra of polycrystalline solids. *Chem. Phys. Lett.*, 87(1):30–33, 1982.

[62] Clare P Grey, Christopher M Dobson, and Anthony K Cheetham. Susceptibility matching in MAS NMR. The determination of hyperfine tensors from paramagnetic stannates. *J. Magn. Reson.*, 98(2):414–420, 1992.

[63] Uwe Schwerk, Dieter Michel, and Marek Pruski. Local magnetic field distribution in a polycrystalline sample exposed to a strong magnetic field. *J. Magn. Reson.*, 119(2):157–164, 1996.

[64] Atsushi Kubo, Thomas P Spaniol, and Takehiko Terao. The effect of bulk magnetic susceptibility on solid state NMR spectra of paramagnetic compounds. *J. Magn. Reson.*, 133(2):330–340, 1998.

[65] Richard R Eckman and Alexander J Vega. Deuterium solid-state NMR study of the dynamics of molecules sorbed by zeolites. *J. Phys. Chem.*, 90(19):4679–4683, 1986.

[66] Marica Cutajar, Sharon E Ashbrook, and Stephen Wimperis. ^{2}H double-quantum MAS NMR spectroscopy as a probe of dynamics on the microsecond timescale in solids. *Chem. Phys. Lett.*, 423(4-6):276–281, 2006.

[67] Liliya Vugmeyster and Dmitry Ostrovsky. Static solid-state ^{2}H NMR methods in studies of protein side-chain dynamics. *Prog. Nucl. Magn. Reson. Spectrosc.*, 101:1–17, 2017.

[68] Robert Tycko. Biomolecular solid state NMR: advances in structural methodology and applications to peptide and protein fibrils. *Annu. Rev. Phys. Chem.*, 52(1):575–606, 2001.

[69] Ireneusz Szewczyk, Anna Rokicinśka, Marek Michalik, Jianhong Chen, Aleksander Jaworski, Rihards Aleksis, Andrew J Pell, Niklas Hedin, Adam Slabon, and Piotr Kusťrowski. Electrochemical denitrification and oxidative dehydrogenation of ethylbenzene over N-doped mesoporous carbon: Atomic level understanding of catalytic activity by ^{15}N NMR spectroscopy. *Chemistry of Materials*, 32(17):7263–7273, 2020.

[70] Max Born and Robert Oppenheimer. Zur quantentheorie der molekeln. *Annalen der physik*, 389 (20):457–484, 1927.

[71] Pierre Hohenberg and Walter Kohn. Inhomogeneous electron gas. *Phys. Rev.*, 136(3B):B864, 1964.

[72] Walter Kohn and Lu Jeu Sham. Self-consistent equations including exchange and correlation effects. *Phys. Rev.*, 140(4A):A1133, 1965.

[73] Seymour H Vosko, Leslie Wilk, and Marwan Nusair. Accurate spin-dependent electron liquid correlation energies for local spin density calculations: a critical analysis. *Canadian Journal of physics*, 58(8):1200–1211, 1980.

[74] John P Perdew and Wang Yue. Accurate and simple density functional for the electronic exchange energy: Generalized gradient approximation. *Phys. rev. B*, 33(12):8800, 1986.

[75] John P Perdew, Kieron Burke, and Matthias Ernzerhof. Generalized gradient approximation made simple. *Phys. Rev. Lett.*, 77(18):3865, 1996.

[76] John P Perdew and Alex Zunger. Self-interaction correction to density-functional approximations for many-electron systems. *Phys. Rev. B*, 23(10):5048, 1981.

[77] Axel D Becke. A new mixing of Hartree-Fock and local density-functional theories. *J. Chem. Phys.*, 98(2):1372–1377, 1993.

[78] Vladimir I Anisimov, Jan Zaanen, and Ole K Andersen. Band theory and Mott insulators: Hubbard U instead of Stoner I. *Phys. Rev. B*, 44(3):943, 1991.

[79] Sergei L Dudarev, Gianluigi A Botton, Sergey Y Savrasov, CJ Humphreys, and Adrian P Sutton. Electron-energy-loss spectra and the structural stability of nickel oxide: An LSDA+U study. *Phys. Rev. B*, 57(3):1505, 1998.

[80] Paul Erhart, Karsten Albe, and Andreas Klein. First-principles study of intrinsic point defects in ZnO: Role of band structure, volume relaxation, and finite-size effects. *Phys. Rev. B*, 73(20): 205203, 2006.

[81] John P Perdew, Robert G Parr, Mel Levy, and Jose L Balduz Jr. Density-functional theory for fractional particle number: derivative discontinuities of the energy. *Phys. Rev. Lett.*, 49(23): 1691, 1982.

[82] Hendrik J Monkhorst and James D Pack. Special points for Brillouin-zone integrations. *Phys. rev. B*, 13(12):5188, 1976.

[83] Georg Kresse and Daniel Joubert. From ultrasoft pseudopotentials to the projector augmented-wave method. *Phys. Rev. B*, 59(3):1758, 1999.

[84] Peter E Blöchl. Projector augmented-wave method. *Phys. Rev. B*, 50(24):17953, 1994.

[85] Chris J Pickard and Francesco Mauri. All-electron magnetic response with pseudopotentials: NMR chemical shifts. *Phys. Rev. B*, 63(24):245101, 2001.

[86] Thibault Charpentier. The PAW/GIPAW approach for computing NMR parameters: A new dimension added to NMR study of solids. *Solid State Nucl. Magn. Reson.*, 40(1):1–20, 2011.

[87] George E Pake. Nuclear resonance absorption in hydrated crystals: fine structure of the proton line. *J. Chem. Phys.*, 16(4):327–336, 1948.

[88] Malcolm H Levitt. *Spin dynamics: basics of nuclear magnetic resonance*. John Wiley & Sons, 2013.

[89] Erwin L Hahn. Spin echoes. *Phys. Rev.*, 80(4):580, 1950.

[90] James H Davis, Kenneth R Jeffrey, Myer Bloom, Marko I Valic, and TP Higgs. Quadrupolar echo deuteron magnetic resonance spectroscopy in ordered hydrocarbon chains. *Chem. Phys. Lett.*, 42(2):390–394, 1976.

[91] Sasa Antonijevic and Stephen Wimperis. Refocussing of chemical and paramagnetic shift anisotropies in ^{2}H NMR using the quadrupolar-echo experiment. *J. Magn. Reson.*, 164(2):343–350, 2003.

[92] Geoffrey Bodenhausen, Herbert Kogler, and RR Ernst. Selection of coherence-transfer pathways in NMR pulse experiments. *J. Magn. Reson.*, 58(3):370–388, 1984.

[93] Sasa Antonijevic and Stephen Wimperis. Separation of quadrupolar and chemical/paramagnetic shift interactions in two-dimensional ^{2}H (I= 1) nuclear magnetic resonance spectroscopy. *J. Chem. Phys.*, 122(4):044312, 2005.

[94] Brennan J Walder, Krishna K Dey, Michael C Davis, Jay H Baltisberger, and Philip J Grandinetti. Two-dimensional NMR measurement and point dipole model prediction of paramagnetic shift tensors in solids. *J. Chem. Phys.*, 142(1):014201, 2015.

[95] Takahiro Iijima, Tadashi Shimizu, and Katsuyuki Nishimura. ^{2}H NMR pure-quadrupole spectra for paramagnetic solids. *J. Magn. Reson.*, 251:57–64, 2015.

[96] Takahiro Iijima, Shinobu Ohki, and Masataka Tansho. Separated quadrupole and shift interactions of ^{2}H NMR spectra in paramagnetic solids by asymmetric pulse sequences. *Solid State Nucl. Magn. Reson.*, 112:101709, 2021.

[97] Rihards Aleksis, José P Carvalho, Aleksander Jaworski, and Andrew J Pell. Artefact-free broadband 2D NMR for separation of quadrupolar and paramagnetic shift interactions. *Solid State Nucl. Magn. Reson.*, 101:51–62, 2019.

[98] Tsang-Lin Hwang and AJ Shaka. Water suppression that works. Excitation sculpting using arbitrary wave-forms and pulsed-field gradients. *J. Magn. Reson.*, 112(2):275–279, 1995.

[99] Katherine Stott, Jonathan Stonehouse, James Keeler, Tsang-Lin Hwang, and AJ Shaka. Excitation sculpting in high-resolution nuclear magnetic resonance spectroscopy: application to selective NOE experiments. *J. Am. Chem. Soc.*, 117(14):4199–4200, 1995.

[100] Edwared J Andrew, Arnold Bradbury, and R G Eades. Nuclear magnetic resonance spectra from a crystal rotated at high speed. *Nature*, 182(4650):1659, 1958.

[101] M Matti Maricq and John S Waugh. NMR in rotating solids. *J. Chem. Phys.*, 70(7):3300–3316, 1979.

[102] Sharon E Ashbrook and David McKay. Combining solid-state NMR spectroscopy with first-principles calculations-a guide to NMR crystallography. *Chem. Commun.*, 52(45):7186–7204, 2016.

[103] Thomas P Spaniol, Atsushi Kubo, and Takehiko Terao. Two-dimensional deuterium magic-angle-spinning nuclear magnetic resonance of paramagnetic compounds: Separation of paramagnetic and quadrupole interactions. *J. Chem. Phys.*, 106(13):5393–5405, 1997.

[104] James Keeler and David Neuhaus. Comparison and evaluation of methods for two-dimensional NMR spectra with absorption-mode lineshapes. *J. Magn. Reson.*, 63(3):454–472, 1985.

[105] Takahiro Iijima and Tadashi Shimizu. Deuterium off-magic-angle spinning NMR spectroscopy for pure-quadrupole spectra of paramagnetic solids. *Solid State Nucl. Magn. Reson.*, 84:234–241, 2017.

[106] W Thomas Dixon. Spinning-sideband-free NMR spectra. *J. Magn. Reson.*, 44(1):220–223, 1981.

[107] W Thomas Dixon. Spinning-sideband-free and spinning-sideband-only NMR spectra in spinning samples. *J. Chem. Phys.*, 77(4):1800–1809, 1982.

[108] Oleg N Antzutkin, SC Shekar, and Malcolm H Levitt. Two-dimensional sideband separation in magic-angle-spinning NMR. *J. Magn. Reson.*, 115(1):7–19, 1995.

[109] Rihards Aleksis and Andrew J Pell. Separation of quadrupolar and paramagnetic shift interactions in high-resolution nuclear magnetic resonance of spinning powders. *J. Chem. Phys.*, 155 (9):094202, 2021.

[110] Luke A O'Dell and Robert W Schurko. QCPMG using adiabatic pulses for faster acquisition of ultra-wideline NMR spectra. *Chem. Phys. Lett.*, 464(1-3):97–102, 2008.

[111] Luke A O'Dell and Robert W Schurko. Fast and simple acquisition of solid-state ^{14}N NMR spectra with signal enhancement via population transfer. *J. Am. Chem. Soc.*, 131(19):6658–6659, 2009.

[112] Pablo Caravatti, Geoffrey Bodenhausen, and Richard R Ernst. Selective pulse experiments in high-resolution solid state NMR. *J. Magn. Reson.*, 55(1):88–103, 1983.

[113] Veronika Vitzthum, Marc A Caporini, Simone Ulzega, and Geoffrey Bodenhausen. Broadband excitation and indirect detection of nitrogen-14 in rotating solids using Delays Alternating with Nutation (DANTE). *J. Magn. Reson.*, 212(1):234–239, 2011.

[114] Clare P Grey and Wiebren S Veeman. The detection of weak heteronuclear coupling between spin 1 and spin 12 nuclei in MAS NMR; ^{14}N/^{13}C/^{1}H triple resonance experiments. *Chem. Phys. Lett.*, 192(4):379–385, 1992.

[115] Clare P Grey, Wiebren S Veeman, and Alexander J Vega. Rotational echo ^{14}N/^{13}C/^{1}H triple resonance solid-state nuclear magnetic resonance: A probe of ^{13}C–^{14}N internuclear distances. *J. Chem. Phys.*, 98(10):7711–7724, 1993.

[116] Zhehong Gan. Measuring amide nitrogen quadrupolar coupling by high-resolution ^{14}N/^{13}C NMR correlation under magic-angle spinning. *J. Am. Chem. Soc.*, 128(18):6040–6041, 2006.

[117] Zhehong Gan. ^{13}C/^{14}N heteronuclear multiple-quantum correlation with rotary resonance and REDOR dipolar recoupling. *J. Magn. Reson.*, 184(1):39–43, 2007.

[118] Zhehong Gan, Jean Paul Amoureux, and Julien Trébosc. Proton-detected ^{14}N MAS NMR using homonuclear decoupled rotary resonance. *Chem. Phys. Lett.*, 435(1-3):163–169, 2007.

[119] Simone Cavadini, Adonis Lupulescu, Sasa Antonijevic, and Geoffrey Bodenhausen. Nitrogen-14 NMR spectroscopy using residual dipolar splittings in solids. *J. Am. Chem. Soc.*, 128(24): 7706–7707, 2006.

[120] Simone Cavadini, Sasa Antonijevic, Adonis Lupulescu, and Geoffrey Bodenhausen. Indirect detection of nitrogen-14 in solids via protons by nuclear magnetic resonance spectroscopy. *J. Magn. Reson.*, 182(1):168–172, 2006.

[121] Simone Cavadini, Sasa Antonijevic, Adonis Lupulescu, and Geoffrey Bodenhausen. Indirect detection of nitrogen-14 in solid-state NMR spectroscopy. *ChemPhysChem*, 8(9):1363–1374, 2007.

[122] Simone Cavadini, Anuji Abraham, and Geoffrey Bodenhausen. Proton-detected nitrogen-14 NMR by recoupling of heteronuclear dipolar interactions using symmetry-based sequences. *Chem. Phys. Lett.*, 445(1-3):1–5, 2007.

[123] GN Manjunatha Reddy, Michal Malon, Andrew Marsh, Yusuke Nishiyama, and Steven P Brown. Fast magic-angle spinning three-dimensional NMR experiment for simultaneously probing H-H and N-H proximities in solids. *Anal. Chem.*, 88(23):11412–11419, 2016.

[124] You-lee Hong, Tetsuo Asakura, and Yusuke Nishiyama. 3D ^{14}N/^{1}H double quantum/^{1}H single quantum correlation solid-state NMR for probing the parallel and anti-parallel beta-sheet arrangement of oligo-peptides at natural abundance. *ChemPhysChem*, 19(15):1841–1845, 2018.

[125] James A Jarvis, Ibraheem M Haies, Philip TF Williamson, and Marina Carravetta. An efficient NMR method for the characterisation of ^{14}N sites through indirect ^{13}C detection. *Phys. Chem. Chem. Phys.*, 15(20):7613–7620, 2013.

[126] James A Jarvis, Maria Concistre, Ibraheem M Haies, Richard W Bounds, Ilya Kuprov, Marina Carravetta, and Philip TF Williamson. Quantitative analysis of ^{14}N quadrupolar coupling using ^{1}H detected ^{14}N solid-state NMR. *Phys. Chem. Chem. Phys.*, 21(11):5941–5949, 2019.

[127] Diego Carnevale, Xiao Ji, and Geoffrey Bodenhausen. Double cross polarization for the indirect detection of nitrogen-14 nuclei in magic angle spinning NMR spectroscopy. *J. Chem. Phys.*, 147 (18):184201, 2017.

[128] Ivan Hung, Peter Gor'kov, and Zhehong Gan. Efficient and sideband-free ^{1}H-detected ^{14}N magic-angle spinning NMR. *J. Chem. Phys.*, 151(15):154202, 2019.

[129] R Tycko and SJ Opella. High-resolution nitrogen-14 overtone spectroscopy: an approach to natural abundance nitrogen NMR of oriented and polycrystalline systems. *J. Am. Chem. Soc.*, 108(12):3531–3532, 1986.

[130] Luke A O'Dell and Christopher I Ratcliffe. ^{14}N magic angle spinning overtone NMR spectra. *Chem. Phys. Lett.*, 514(1-3):168–173, 2011.

[131] Luke A O'Dell and Andreas Brinkmann. ^{14}N overtone NMR spectra under magic angle spinning: Experiments and numerically exact simulations. *J. Chem. Phys.*, 138(6):064201, 2013.

[132] Andrew J Pell, Kevin J Sanders, Sebastian Wegner, Guido Pintacuda, and Clare P Grey. Low-power broadband solid-state MAS NMR of ^{14}N. *J. Chem. Phys.*, 146(19):194202, 2017.

[133] Simone Cavadini, Anuji Abraham, Simone Ulzega, and Geoffrey Bodenhausen. Evidence for dynamics on a 100 ns time scale from single-and double-quantum nitrogen-14 NMR in solid peptides. *J. Am. Chem. Soc.*, 130(33):10850–10851, 2008.

[134] Malcolm H Levitt. Symmetry in the design of NMR multiple-pulse sequences. *J. Chem. Phys.*, 128(5):052205, 2008.

[135] Malcolm H Levitt. Symmetry-based pulse sequences in magic-angle spinning solid-state NMR. *in Encocyclopedia of NMR*, 9:165–196, 2002.

[136] Andreas Detken, Edme H Hardy, Matthias Ernst, and Beat H Meier. Simple and efficient decoupling in magic-angle spinning solid-state NMR: the XiX scheme. *Chem. Phys. Lett.*, 356(3-4): 298–304, 2002.

[137] Rihards Aleksis and Andrew J Pell. Low-power synchronous helical pulse sequences for large anisotropic interactions in MAS NMR: Double-quantum excitation of ^{14}N. *J. Chem. Phys.*, 153 (24):244202, 2020.

[138] Michael Mehring and John S Waugh. Phase transients in pulsed NMR spectrometers. *Rev. Sci. Instrum.*, 43(4):649–653, 1972.

[139] Johannes J Wittmann, Kazuyuki Takeda, Beat H Meier, and Matthias Ernst. Compensating pulse imperfections in solid-state NMR spectroscopy: A key to better reproducibility and performance. *Angew. Chem. Int. Ed.*, 54(43):12592–12596, 2015.

[140] Hiroki Nagashima, Aany Sofia Lilly Thankamony, Julien Trébosc, Frédérique Pourpoint, Olivier Lafon, and Jean Paul Amoureux. γ-independent through-space hetero-nuclear correlation between spin-1/2 and quadrupolar nuclei in solids. *Solid State Nucl. Magn. Reson.*, 84:216–226, 2017.

[141] Yoji Kobayashi, Olivier J Hernandez, Tatsunori Sakaguchi, Takeshi Yajima, Thierry Roisnel, Yoshihiro Tsujimoto, Masaki Morita, Yasuto Noda, Yuuki Mogami, Atsushi Kitada, et al. An oxyhydride of $BaTiO_3$ exhibiting hydride exchange and electronic conductivity. *Nat. Mater.*, 11 (6):507–511, 2012.

[142] Tasuku Uchimura, Fumitaka Takeiri, Kei Okamoto, Takashi Saito, Takashi Kamiyama, and Genki Kobayashi. Direct synthesis of barium titanium oxyhydride for use as a hydrogen permeable electrode. *J. Mater. Chem. A*, 9(36):20371–20374, 2021.

[143] Ya Tang, Yoji Kobayashi, Kazuki Shitara, Ayako Konishi, Akihide Kuwabara, Takahide Nakashima, Cédric Tassel, Takafumi Yamamoto, and Hiroshi Kageyama. On hydride diffusion in transition metal perovskite oxyhydrides investigated via deuterium exchange. *Chem. Mater.*, 29(19):8187–8194, 2017.

[144] Xin Liu, Tor Svendsen Bjørheim, and Reidar Haugsrud. Formation and migration of hydride ions in $BaTiO_{3-x}H_x$ oxyhydride. *J. Mater. Chem. A.*, 5(3):1050–1056, 2017.

[145] Carin Eklöf-Österberg, Reji Nedumkandathil, Ulrich Häussermann, Aleksander Jaworski, Andrew J Pell, Madhusudan Tyagi, Niina H Jalarvo, Bernhard Frick, Antonio Faraone, and Maths Karlsson. Dynamics of hydride ions in metal hydride-reduced BaTiO3 samples investigated with quasielastic neutron scattering. *J. Phys. Chem. C*, 123(4):2019–2030, 2018.

[146] Carin Eklöf-Österberg, Laura Mazzei, Erik Jedvik Granhed, Göran Wahnström, Reji Nedumkandathil, Ulrich Häussermann, Aleksander Jaworski, Andrew J Pell, Stewart F Parker, Niina H Jalarvo, et al. The role of oxygen vacancies on the vibrational motions of hydride ions in the oxyhydride of barium titanate. *J. Mater. Chem. A*, 8(13):6360–6371, 2020.

[147] Guillaume Bouilly, Takeshi Yajima, Takahito Terashima, Wataru Yoshimune, Kousuke Nakano, Cédric Tassel, Yoshiro Kususe, Koji Fujita, Katsuhisa Tanaka, Takafumi Yamamoto, et al. Electrical properties of epitaxial thin films of oxyhydrides $ATiO_{3-x}H_x$ (A= Ba and Sr). *Chem. Mater.*, 27(18):6354–6359, 2015.

[148] Cesare Franchini, Michele Reticcioli, Martin Setvin, and Ulrike Diebold. Polarons in materials. *Nat. Rev. Mater.*, pages 1–27, 2021.

[149] Yuriy Natanzon, Amram Azulay, and Yaron Amouyal. Evaluation of polaron transport in solids from first-principles. *Isr. J. Chem.*, 60(8-9):768–786, 2020.

[150] Erik Jedvik Granhed, Anders Lindman, Carin Eklöf-Österberg, Maths Karlsson, Stewart F Parker, and Göran Wahnström. Band vs. polaron: vibrational motion and chemical expansion of hydride ions as signatures for the electronic character in oxyhydride barium titanate. *J. Mater. Chem. A*, 7(27):16211–16221, 2019.

[151] Tai Misaki, Itaru Oikawa, and Hitoshi Takamura. Negative Knight shift in Ba-Ti oxyhydride: An indication of the multiple hydrogen occupation. *Chem. Mater.*, 31(18):7178–7185, 2019.

[152] Subramanian Srinivasan, Pieter CMM Magusin, Willem P Kalisvaart, Peter HL Notten, Fermin Cuevas, Michel Latroche, and Rutger A van Santen. Nanostructures of $Mg_{0.65}Ti_{0.35}D_x$ studied with X-ray diffraction, neutron diffraction, and magic-angle-spinning ^2H NMR spectroscopy. *Phys. Rev. B*, 81(5):054107, 2010.

[153] Paul Hodgkinson and Lyndon Emsley. The reliability of the determination of tensor parameters by solid-state nuclear magnetic resonance. *J. Chem. Phys.*, 107(13):4808–4816, 1997.

[154] Lawrence H Bennett, Richard E Watson, and GC Carter. Relevance of Knight shift measurements to the electronic density of states. *J. Res. Natl. Bur. Stand.*, 74(4):569, 1970.

[155] John B Goodenough. Theory of the role of covalence in the perovskite-type manganites [La, M (II)] MnO_3. *Phys. Rev.*, 100(2):564, 1955.

[156] John B Goodenough. An interpretation of the magnetic properties of the perovskite-type mixed crystals $La_{1-x}Sr_xCoO_{3-\lambda}$. *J. Phys. Chem. Solids*, 6(2-3):287–297, 1958.

[157] Junjiro Kanamori. Superexchange interaction and symmetry properties of electron orbitals. *J. Phys. Chem. Solids*, 10(2-3):87–98, 1959.

[158] Hua Guo, Aleksander Jaworski, Zili Ma, Adam Slabon, Zoltan Bacsik, Reji Nedumkandathil, and Ulrich Häussermann. Trapping of different stages of $BaTiO_3$ reduction with LiH. *RSC Advances*, 10(58):35356–35365, 2020.

[159] Stephan Lany and Alex Zunger. Polaronic hole localization and multiple hole binding of acceptors in oxide wide-gap semiconductors. *Phys. Rev. B*, 80(8):085202, 2009.

[160] Paul Erhart, Andreas Klein, Daniel Åberg, and Babak Sadigh. Efficacy of the DFT+U formalism for modeling hole polarons in perovskite oxides. *Phys. Rev. B*, 90(3):035204, 2014.